HYDRODYNAMIC ANALYSIS OF MOORING LINES BASED ON

OPTICAL TRACKING EXPERIMENTS

A Dissertation

by

WOO SEUK YANG

Submitted to the Office of Graduate Studies of
Texas A&M University
in partial fulfillment of the requirements for the degree of

DOCTOR OF PHILOSOPHY

December 2007

Major Subject: Ocean Engineering

HYDRODYNAMIC ANALYSIS OF MOORING LINES BASED ON

OPTICAL TRACKING EXPERIMENTS

A Dissertation

by

WOO SEUK YANG

Submitted to the Office of Graduate Studies of
Texas A&M University
in partial fulfillment of the requirements for the degree of

DOCTOR OF PHILOSOPHY

Approved by:

Chair of Committee,	Richard Mercier
Committee Members,	Moo-Hyun Kim
	Jun Zhang
	Achim Stössel
Head of Department,	David Rosowsky

December 2007

Major Subject: Ocean Engineering

ABSTRACT

Hydrodynamic Analysis of Mooring Lines Based on Optical Tracking Experiments.

(December 2007)

Woo Seuk Yang, B.S.; M.S., Chung-Ang University

Chair of Advisory Committee: Dr. Richard Mercier

Due to the complexity of body-shape, the investigation of hydrodynamic forces on mooring lines, especially those comprised of chain segments, has not been conducted to a sufficient degree to properly characterize the hydrodynamic damping effect of mooring lines on the global motions of a moored offshore platform. In the present study, an experimental investigation of the hydrodynamic characteristics of various mooring elements is implemented through free and forced oscillation tests. Since no direct measurement capability for distributed hydrodynamic forces acting on mooring line segments such as chain and wire rope is available yet, an indirect measurement technique is introduced. The technique is based on the fact that hydrodynamic forces acting on a body oscillating in still water and on a stationary body in an oscillatory flow are equivalent except for the additional inertia force, the so-called Froude-Krylov force, present in the latter condition. The time-dependent displacement of a slender body moving in calm water is acquired through optical tracking with a high speed camera. The distributed hydrodynamic measurements are then used to obtain the force by solving the equation of motion with the boundary condition provided from tension measurements.

Morison's equation is employed along with Fourier analysis to separate the inertia and drag components out of the total fluid force. Given the experimentally-derived information on hydrodynamic behavior, the resistance provided by a mooring line to a floating structure is briefly studied in terms of damping and restoring force in a coupled dynamic system.

DEDICATION

To my father, Jae-il Yang, looking after my family in heaven

ACKNOWLEDGMENTS

I would like to express my sincere gratitude to my advisor Dr. Richard Mercier for his inspiration, encouragement, and guidance during my research. I would also like to give my thankful word to Dr. Moo-Hyun Kim, Dr. Jun Zhang and Dr. Achim Stössel for their help and guidance as members of my dissertation committee. Special thanks are extended to all the faculty members of the Coastal and Ocean Engineering Division in the Zachry Civil Engineering Department for their academic support.

I cannot help expressing my deepest thanks to Dr. Won-chul Cho, and Dr. Woo-sun Park in Korea, for their continuous counsel and incitement.   Although I cannot name all my best friends in Korea, I am cordially grateful to them for encouragement.

I would like to express my appreciation to my parents, Min-ja Lim, and Jae-il Yang, and to my brother, Moon-seong Yang, for their continuous support and inspiration throughout my life.   Lastly, I would like to express heartfelt thanks to my wife, Eun-hee Cha, and to my lovely son, Andrew (Si-myeong) Yang, for their patience, support and encouragement during my study.

TABLE OF CONTENTS

LIST OF FIGURES

Page

LIST OF TABLES

CHAPTER I

BACKGROUND AND MOTIVATION

1.1. Introduction

The design of a floating offshore structure primarily requires the wave and current loading information on the floating body itself. In addition, knowledge of the hydrodynamic forces exerted on slender body tether components such as mooring lines and risers is required for the accurate analysis of the global response of the floating structure. In particular, the inertia and damping contributions of moorings and risers to the overall system become quite significant as sea-depth increases. Generally, model tests are implemented to verify the numerical simulation results of moored body motion for design purposes. Due to limitations of the force model for slender bodies (the Morison equation), an important source of uncertainty in the validation of numerical models using experimental model test results or field measurements is the empirical force transfer coefficients that are the basis of the modeling approach.

Numerous investigations of time-dependent hydrodynamic forces acting on slender bodies have been conducted. These investigations were normally confined to laboratory experiments designed to verify and calibrate the well-known Morison equation. A limited number of field tests have been performed for the wider range of parameters (Reynolds number, Keulegan-Carpenter number) of interest in the design of offshore structures that could not be easily created in the laboratory (Dean & Aagaard,

---

This dissertation follows the style and format of Journal of Ocean Engineering.

1970; Kim and Hibbard, 1975). However field measurement of Morison force coefficients is complicated by the uncertainty of the ocean environment and the high cost of the experimental set-up. Laboratory model tests have been carried out under a variety of flow conditions, including impulsively started flows (Sarpkaya, 1966), uniformly accelerating flows (Sarpkaya and Garrison, 1963), and oscillating flows (Keulegan and Carpenter, 1958), to provide an extensive amount of rational data for the design of offshore structures.

The empirical Morison equation was proposed about a half century ago for the estimation of fluid force on a pile. It has been widely used even up to the present time since no better formula has been introduced to replace it. The Morison equation is a force decomposition formula that, under viscous, unsteady flow conditions, represents the total force exerted by the fluid on a slender body as the sum of a drag force and an inertia (or added mass) force. Each force term has its own associated force transfer coefficient. The so-called drag coefficient and inertia (or added mass) coefficient are each strongly dependent on the shape of the body. Thus, many researchers have focused on finding the correct value of these coefficients for several types of bodies (for example, spheres, plates, and especially circular cylinders) under diverse flow conditions mentioned above. Nevertheless, empirical data on Morison force coefficients for chain-shaped bodies is scarce.

Mooring lines for deepwater floating structures generally comprise a number of different elements, such as studlink or studless chain, sheathed or unsheathed wire or polyester rope, and various types of connectors. Sheathed wire or polyester rope is circular in cross section so that the hydrodynamic force coefficients can be readily

obtained from published data on cylindrical rod elements.   Due to lack of available data, the drag coefficients for chains are typically assumed to be the same as for a rod, but with an equivalent diameter equal to twice the bar size of the chain link. Occasionally, the manufacturers provide the drag coefficients for their own chain obtained from simple towing tests.   Hwang (1986) conducted towing tests to estimate the drag coefficients for two different chain types and marine cables for steady state flow conditions.   It can be inferred that there is no single set of representative values of such coefficients for all different kinds of chain.   Thus, efficient, standardized measurement techniques are needed for estimation of force coefficients of mooring elements.

The design of a moored floating system generally involves both numerical simulation and model tests.   For the model tests, we are often faced with the problem of how to relate the experimental results to full scale while accounting for modeling errors. In the case of mooring systems, apart from viscous scale effects, we have to consider that the chain and cable elements used in the model scale mooring will likely not be geometrically similar to the prototype.   Consequently there are rational reasons for employing different Morison force coefficients at model and prototype scale.   However since there is a lack of data on drag and inertia forces for chains and, to our knowledge, no available direct experimental investigations of mooring line dynamics at a level of detail sufficient to isolate the hydrodynamic forces, there is inherently a large degree of uncertainty in the experimental and numerical modeling of hydrodynamic forces on mooring lines.

Complexity of shape is one of the major factors that complicates experiments with chain.   Chain comprises interconnected links which have the shape of elongated

circular rings, so that direct force measurement on the body (i.e. the chain link) using a force gauge is difficult. Since the links are free to rotate at the interconnections to a certain extent, the torsional motion of the chain might be a consideration in the analysis even for small lengths of chain. Also, as compared to simple body shapes, the complex geometry of chain links causes more complex wake flow kinematics. For these reasons, predicting the hydrodynamic loading on moving chain is quite challenging.

In the present research, an investigation of the hydrodynamic force acting on chain and cable elements is implemented by laboratory model tests employing an optical tracking system. The tests involve free and forced oscillations of long chain or cable segments under conditions representative of mooring systems in still water. Laboratory tests and data analysis were planned for both two dimensional and three dimensional motion conditions. Unfortunately because of camera limitations and obstructions in the basin it was not possible to perform three dimensional experiments at this time.

1.2. Literature Review

1.2.1. Analysis of Hydrodynamic Force

Fluid loading on an object induced by a flow around it has been highly investigated by a number of hydrodynamicists in engineering and applied mathematics. Generally, fluid loading can be categorized into viscous fluid effects and irrotational fluid effects according to the nature of the problem addressed. For the irrotational fluid effects, the flow can be represented by potential theory, excluding the complicated behavior very near the structure. However, viscous flow around an object generally involves

formation of a wake, with vortex generation and separation which strongly disturbs the velocity-pressure field around the body. Due to the viscosity of the fluid, the flow in the boundary layer evolves into a vortex by the shearing process, the vortex separates from the surface of the body, thereby forming a wake. By contrast, the flow outside the boundary layer is considered to be ideal potential flow without the viscous boundary layer effect. Although numerous studies have been conducted, many characteristics of these phenomena remain difficult to model, such as the size of the wake, formation and motion of vortices, flow separation points, etc. This is due not only to the complexity of the flow field but also because of the diversity of flow conditions and of body shapes. Thus, certain specific flow conditions with certain body shapes have been mainly studied to gain better understanding of the flow field and fluid loading effects.

Two main approaches have been developed for calculating the hydrodynamic force on a body in an oscillatory flow: one is based on the potential theory and the other is based on the Navier-Stokes equations. The former is commonly implemented by superposing the viscous effects on the solution of the ideal fluid behavior. The latter can be categorized again into several different approaches in terms of the formulation of the governing equations. Both methodologies have been implemented theoretically and, in some case, experimental observations were required to complement the theoretic approaches.

O.S. Madsen (1986) developed the potential theory for a uniformly accelerated flow of an ideal fluid. The combined potential ϕ, which is comprised of an undisturbed flow potential Φ_U and a disturbed flow potential Φ_D due to the presence of the body, was employed for the loading and flow perturbation was applied to obtain the disturbed

flow potential. The hydrodynamic force is obtained by integrating the dynamic pressure over the body surface.

$$F = -\int_s P_n \vec{n}\, ds = \rho \int_s (\partial\phi/\partial t + (\nabla\phi)^2/2)\vec{n}\; ds \tag{1.1}$$

in which nonlinear effects arise from using the Lagrangian derivative in the transient pressure term and directly from the velocity-squared term. According to the potential flow formulation, the derived hydrodynamic force has a contribution only from the inertia force, not from viscous drag.

James Lighthill (1979) suggested that the inertia force could be expressed to second-order by superposing the second order loading due to both the quadratic potential and quadratic interactions associated with the first-order potential to the linear loading associated with the first-order potential, In the Morison force limit the second-order loading resulting from the linear potential was considered in a similar manner as Madsen but including one more contribution, the so-called waterline force generated by the difference between the hydrostatic pressure and the transient pressure. The waterline force, which only applies to surface-piercing bodies, is written as follows and added to the above equation:

$$F_w = \int_w \frac{\rho}{2g}\left(\frac{\partial\phi}{\partial t}\right)^2 dw \tag{1.2}$$

Both the Madsen and Lighthill approaches give a correction to the inertia term in Morison's equation by adding a term associated with a nonlinear contribution.

T.E. Horton and J.W. Rish (1981) devised the Inertia Pressure Concept (IPC) as an empirical wave force algorithm. This concept enables a viscous correction to the pressure distribution associated with the potential flow by integrating the pressure over

the front (before separation) and rear surface (after separation) of the cylinder respectively with two time-dependent empirical coefficients, C_f and C_r, which account for the flow separation and wake sweeping. The pressure term is obtained from a nonlinear Euler-Bernoulli equation,

$$\frac{P}{\rho} + \frac{\partial \phi}{\partial t} + \frac{1}{2}q_{rel}^2 = G(t) \tag{1.3}$$

where q_{rel} denotes the fluid velocity relative to the body. The force algorithm is expressed in the following form:

$$\frac{F}{\rho D L} = 2\int_0^\pi \frac{dF}{\rho D L}$$

$$= -C_f \int_{\theta_S}^\pi \frac{P - P_m}{\rho}\cos\theta\, d\theta - C_r \int_0^{\theta_S} \frac{P - P_m}{\rho}\cos\theta\, d\theta = F_I + F_D + F_R \tag{1.4}$$

where θ_s denotes the circumferential angle on the cylinder where flow separation occurs, D and L are the diameter and length of the cylinder, subscript m indicates the minimum pressure location on the surface of cylinder, and F_I, F_D, and F_R represent the inertia, drag and interaction terms. It is noteworthy that the velocity-acceleration interaction term in addition to the drag and inertia force terms in the Morison equation were included in the algorithm. Furthermore, the IPC algorithm can in principle model the temporal behavior of the force coefficients and it suggests an interdependency of the drag and inertia force coefficients.

T. Sarpkaya and C.J. Garrison (1963) investigated the uniform flow with constant acceleration around a circular cylinder by combining the analytically-derived equations for the complex potential ($\omega = \phi + i\psi$) with a discrete vortex whose characteristics were obtained experimentally. The constant acceleration condition that was used enabled a

dimensional analysis to exclude the higher order accelerations on which the force might depend. The hydrodynamic force was formulated with a general form of the Blasius theorem which can separate the force into the total drag and lift components. Through dimensional analysis and the conventional Morison's equation, formulations were obtained respectively for the drag and inertia coefficients. This research showed that there is a unique relationship between the drag and inertia coefficients.

As mentioned earlier, a number of approaches are available for hydrodynamic analysis with the Navier-Stokes equations. These include: a) direct calculation with boundary conditions, b) control volume approach, c) coupled analysis with the equation of motion for the body and d) stream function-vorticity formulation. The stream function-vorticity formulation is based on non-primitive variables, while the rest are formulated with the primitive variables which are the velocities and pressure. General forms of the Navier-Stokes equations and the vorticity transport equation are written as

$$\rho\left(\frac{\partial \vec{u}}{\partial t} + \vec{u} \cdot \nabla \vec{u}\right) = -\nabla p + \mu \nabla^2 \vec{u} \quad \text{and} \quad \frac{\partial \vec{\omega}}{\partial t} = \nabla \times (\vec{\omega} \times \vec{u}) = \nu \nabla^2 \vec{\omega} \qquad \textbf{(1.5)}$$

S. Murashige, et al (1989) solved the flow field around an oscillating circular cylinder by direct calculation using a body-fitted coordinate system. In their study, the Navier-Stokes equations were solved in the form of partial differential equations with discretized time and spacing. An additional Poisson equation for pressure was introduced for solving the pressure prior to the calculation of the velocity through the Navier-Stokes equations. The comparison of the computed time-dependent in-line force with published experimental data was in good agreement at low Keulegan-Carpenter numbers.

M. Braza, et al (1985) applied the control volume approach for the unsteady flow of an incompressible viscous fluid past a cylinder in a logarithmic-polar coordinate system by employing the finite volume approximation in conjunction with a predictor-corrector pressure scheme. The pressure is deduced by combining the Navier-Stokes equations and a Poisson equation for an auxiliary potential function ϕ. The Poisson equation was only used for pressure correction through an iterative method. The hydrodynamic force was obtained by integrating the wall pressure and wall vorticity, which represent the contributions of the pressure and viscous forces, respectively.

T.E. Horton and M.J. Feifarek (1981) presented a wave force formulation, the so-called Vorticity Transport Integral Concept (VTIC), in which the Navier-Stokes equations for the unsteady flow of an incompressible viscous fluid are solved by integration over an arbitrary volume of fluid surrounding the body through Green's transformation theorem. The usual acceleration operator is replaced by Lagrange's relationship

$$\frac{D\vec{u}}{Dt} = \frac{\partial \vec{u}}{\partial t} + \vec{\omega} \times \vec{u} + \nabla \left(\left| \vec{u} \right| \left| \vec{u} \right| / 2 \right) \tag{1.6}$$

in formulating the vorticity transport concept of the equations of motion, which is different from the general vorticity transport equation [Eq.(1.5)]. Since vorticity is considered to be transported from the boundary layer volume to the wake volume, integration is required to be taken only over the flow near the body, not over the entire flow. The analytical force formulation which takes account of force contributions from the wake inertia defect and vorticity transport can predict the hydrodynamic loading of transient flow on a submerged body.

One of the vorticity-based formulations is the so-called "vortex method" which

approximates the distribution of vorticity by a set of discrete point vortices and thus follows the Lagrangian flow concept. Using this method, P.A. Smith and P.K. Stansby (1988) investigated the viscous flow of an incompressible fluid past a circular cylinder in a polar coordinate system. Vorticity is created from solving the Poisson equation for the stream function by means of a Fourier transform technique, and distributed on the cylinder surface to satisfy the no-slip condition. Then the processes of viscous diffusion and convection are accomplished respectively by a linear diffusion equation and the nonlinear Euler equation, both of which are separate from the vorticity transport equation. The in-line and transverse forces were calculated using two different formulations and the comparison between both results showed good agreement; one is associated with the pressure distribution and the other with the cross product of velocity and vorticity. Comparisons made with experimental data and results from a Eulerian scheme showed good agreement and indicated the better stability of the Lagrangian scheme compared to the Eulerian scheme.

P. Justesen (1990) presented the solution to the stream function-vorticity formulation for a circular cylinder in planar oscillating flow by adopting an Eulerian finite difference scheme. A logarithmic-polar coordinate system was applied to resolve the large gradients near the cylinder surface. The stream function was split into two parts: (a) one due to the prescribed externally driven potential flow, and (b) the other representing a correction due to the viscosity. Unlike the vortex method, vorticity was obtained from the vorticity equation using the prescribed stream function (a) which is derived from the analytical solution of the Laplace equation. The Poisson equation was used to acquire the stream function (b) which was combined with the stream function (a) to yield

the total stream function. The tangential momentum equation at the cylinder surface was derived for the pressure calculation in the same way as for the vortex method. The surface pressure and the surface stress associated with vorticity were integrated over the cylinder surface for the calculation of the total force.

Karl W. Schulz and Y. Kallinderis (2000) developed a numerical method for the solution of coupled fluid-body dynamics in three dimensions. The rigidly-mounted elastic body structural response was coupled with the incompressible Navier-Stokes equations to address the flow-structure interaction. Applications of fixed and freely vibrating structures were presented to give a comparison with experimental observations.

1.2.2. Methods for Estimation of Morison Hydrodynamic Force Coefficients

As mentioned at the outset, for the estimation of force on a slender body Morison's formula has been mostly used and trusted to a certain degree, although a number of alternative theoretical and numerical approaches have been developed in the past half century. Some efforts have been dedicated to identifying ways to modify the existing equation to more precisely model the various force mechanisms, however the main stream of research has been focused on the estimation of suitable force transfer coefficients. The following section briefly reviews various methods of analysis for the determination of the hydrodynamic coefficients, including both deterministic and stochastic approaches.

1.2.2.1. Deterministic Approach

The Fourier averaging technique first given by Keulegan and Carpenter (1958) is to reconcile the Morison equation with the Fourier series representation of the measured force, by taking the first harmonic only and applying the orthogonality of trigonometric functions to estimate each coefficient. The reconciled form of the Morison equation is expressed as

$$\frac{2F}{\rho U_m^2 D} = \frac{\pi^2}{KC} C_m \sin \omega t - C_d \left| \cos \omega t \right| \cos \omega t \qquad (1.7)$$

where U_m and ω denote the maximum velocity and the angular frequency of harmonic flow, respectively. Using this method, J.R. Driscoll (1972) analyzed test data for the simple harmonic motion of an oscillating cylinder in still water and found that the drag coefficient is a function of both Re and KC but the added mass coefficient primarily depends on KC.

C.J. Garrison, et al (1977) conducted similar model tests to those of Driscoll but applied a least-square analysis to determine the drag and added mass coefficients. Specifically, by defining the squared error between the measured and calculated forces as

$$E^2 = (F_M - F_C)^2 \qquad (1.8)$$

the drag and added mass coefficients are determined by minimizing the squared error according to

$$\frac{d E^2}{d C_d} = 0 \quad \text{and} \quad \frac{d E^2}{d C_m} = 0. \qquad (1.9)$$

Unlike Driscoll, he suggested that both coefficients strongly depend on Re except at high Re.   It was also shown that, when KC decreases, the drag and added mass coefficients approach respectively to zero and unity, which are the values associated with potential flow.

G. Rodenbusch and C. Kallstrom (1986) studied the forces on a large cylinder undergoing random directional oscillation in two dimensions transverse to the cylinder axis.   The least-square method was used to estimate the force coefficients in conjunction with a velocity tracking scheme in which the component of the force at each instant of time is aligned with the instantaneous velocity.   However this analysis scheme yields poor estimates of the added mass coefficient since the acceleration is not aligned with the direction of the velocity in which the force is considered.   Thus, it has been inferred that using an alternative acceleration tracking scheme for the added mass force might yield better estimates for the added mass coefficient.

P.W. Bearman, J.R. Chaplin, et al (1985) carried out measurements of the fluid loading on a vertical and a horizontal cylinder in periodic and random waves under controlled laboratory conditions.   A time averaging version of the Fourier technique and least-square error minimization were employed to evaluate the hydrodynamic coefficients for the vertical and horizontal cylinder, respectively.   The Fourier analysis method used by Bearman was different from the others mentioned above in that the first six Fourier components of the force and velocity were considered, thereby providing better accuracy.   Bearman concluded that Morison's equation cannot provide a good representation of the force for the horizontal cylinder, because due to wake rotation the transverse component of vortex shedding cannot be separated from the in-line drag

component in Morison's equation.

T. Sarpkaya (1976a, b) studied the characteristics of periodic flow past a bluff body. He analyzed model test results with Morison's equation to correlate the force data with the drag and inertia coefficients. Three different methods were applied: 1) Fourier analysis, 2) least-square method, and 3) modified least-square method with the squared error defined as $E^2 = F_M^2 (F_M - F_C)^2$. The last method is similar in form to the ordinary least-square method except for the addition of the square of the measured force as a weighting factor. It was shown that the results from all three methods differ by only one or two percent from each other.

The system identification technique may also be used for estimation of the hydrodynamic coefficients. The technique has the advantage of being able to address the time-dependent problem, while other techniques referenced above are associated with time-averaged or frequency-averaged force modeling. P. Kaplan, C.W. Jiang and F.J. Dello Stritto (1981) analyzed the wave measurement data from the Ocean Test Structure (OTS) by applying the sequential estimation technique, which is used to estimate the state variables and the system parameters in a noisy nonlinear dynamical system. The coupled first-order differential equations from Morison's equation were constructed in the x-y directions based on the six state variables (including the force coefficients) and solved via an integration scheme in matrix form to yield the time-varying coefficients and velocity fields. They suggested that this method is more robust than the spectral-fitting technique and that Morison's formula is suitable for the representation of wave force by comparison with the alternative force model in which the velocity-squared drag force term ($u|u|$) is replaced by the sum of a linear (u) and a

cubic (u^3) velocity term.

1.2.2.2. Stochastic Approach

The studies referenced in the previous section all involved deterministic analysis generally implemented in the time domain. Since waves in the ocean are generally considered to be a mildly non-Gaussian random process, the wave forces on a body and the induced body responses should also be modeled as a random process. Based on this idea, a diversity of stochastic approaches combined with linear wave theory and applied to representations of Morison's equation have been proposed in order to provide improved estimates of wave force for the design of offshore structures.

L.E. Borgman (1965, 1967) carried out spectral analysis of the force on a body in a turbulent fluid by employing a zero-memory, nonlinear transformation of the bivariate Gaussian process for the velocity and acceleration of the fluid. The covariance of the force was developed by deriving the probability density function and the moment generating function, and then expressed with a series expansion. The partial sums of the series were transformed into the spectral density of a Morison-type force.

$$S_{FF}(\omega) = K_D^2 \, \frac{\sigma_V^4}{\pi} \left[\frac{8\, S_{VV}(\omega)}{\sigma_V^2} \right] + K_M^2 \, S_{AA}(\omega)$$

(1.10)

$$K_D = \frac{1}{2}\rho D\, C_D \quad \text{and} \quad K_M = \frac{1}{4}\pi \rho D^2\, C_m$$

where σ_V^2 is the variance of velocity, and $S_{FF}(\omega)$, $S_{VV}(\omega)$, $S_{AA}(\omega)$ denote the spectral density of force, velocity and acceleration of fluid, respectively. The determination of

the drag and inertia coefficients was achieved by a least square fitting of the theoretical covariance model to the measured force covariance.

Later Borgman (1969) developed a different spectral analysis approach based on a digital filter concept which inter-relates the fluid velocity and acceleration with the wave surface elevation through a linear integral operator. To simplify the application of the digital filter to Morison's formula, the nonlinear drag term was approximated by statistical least square fitting of the velocity process. In this research, the force coefficients were determined by applying the theoretical constraint that the inertia and drag force respectively equal zero below the wave crests and the wave zero crossing points.

W.J. Pierson and P. Holmes (1965) studied the force on a vertical pile in shallow water with irregular long-crested waves in a probabilistic manner. The probability function of force was developed using a joint probability density function of velocity and acceleration to avoid difficulties with the representation of force in terms of covariance and spectra due to the non-Gaussian nature of the drag term. The method of moments was applied to express the second and fourth statistical moments of force as

$$E[F^2] = K_M^2 \, \sigma_A^2 \, + \, 3 K_D^2 \, \sigma_V^4$$

$$(1.11)$$

$$E[F^4] = 3 \left(K_M^4 \, \sigma_A^4 \, + \, 6 K_M^2 \, \sigma_A^2 \, K_D^2 \, \sigma_V^4 \, + \, 35 K_D^4 \, \sigma_V^8 \right)$$

Later, many researchers including R.G. Tickell (1977) and R. Burrows (1977) further developed the method of Pierson and Holmes to analyze the wave loading on assemblages of offshore structural members (as opposed to a single object).

While most statistical approaches for the estimation of the hydrodynamic force

coefficients were based on the averaged value of the wave force, C.L. Bretschneider (1967) evaluated the coefficients using peak forces derived at or ahead of the wave crest since the maximum probable values of wave height and force are preferred in the design of offshore structures.   In order to suggest a better selection of the coefficients for the design wave, Bretschneider attempted to correlate the empirical coefficients with the probability distribution of wave heights via evaluation of the terms "correlation drag (or inertia) coefficient" associated with the crest (or the wave zero-crossing).

T. Bostrom (1987) investigated several different stochastic approaches to model the wave force on an object: 1) the method of moments, 2) the maximum likelihood method, 3) the least square fitting of a spectrum, 4) cross-spectra between surface elevation and force, and 5) fitting time series of force by an extended Kalman filter.   These methods may be grouped into three categories: the first two are applied in the probability domain, the last is applied in the time domain, and the other are applied in the frequency domain. Results from the probability and frequency domain methods were in close agreement, however the results from the time domain method displayed somewhat larger values of force coefficients than those from the other methods.

1.2.3. Mooring Line Damping

The response of a moored floating structure in irregular seas is generally determined by the first-order wave frequency forces and the second-order low frequency drift forces. While the motion due to the first-order forces can be straightforwardly evaluated through linear wave radiation/diffraction theory, the resonant low frequency drift motions of the

floater due to second-order forces are primarily controlled by damping effects from the hull and mooring systems. Modeling of these damping effects involves many uncertainties because of the nonlinear mechanisms, the selection of force coefficients, the effect of seabed friction, etc. System damping is contributed by several components: the wave drift damping, the wind damping, the current and viscous flow damping on the hull, and the mooring line damping. Among them, the studies focused on the mooring line damping are relevant to this research and will be reviewed briefly.

Several different approaches have been developed to model mooring-induced damping. E. Huse (1986) employed the dissipated energy method with the catenary equation to estimate the low frequency mooring damping. The friction force (between the mooring line and the seabed) and drag force which provide the main contributions to the mooring line damping were considered separately and the energy dissipated by the drag force was obtained by integrating the force over a cycle ($\Delta E = 2 \int F_D \, d\eta$), where the top end of the line was assumed to move horizontally and η is the displacement of the mooring line in the normal direction. It was shown that the mooring line drag can reduce the second order motion by 20 ~ 25%, representing one-third of the total mooring system damping, while the friction damping contributes only a small portion to the total damping.

Further developing Huse's approach, J.E.W. Wichers and R.H.M. Huijsmans (1990) incorporated the dynamic effect of the chain with the dissipated energy method for the analysis of mooring damping on the low frequency motion. The equation of motion based on the lumped mass method was solved for the dynamic behavior of the chain, and the product of low frequency velocity and horizontal component of chain force at the

chain table was integrated to determine the effect of damping ($E = \int T(x)\dot{x}\,dt$). The combined low and high (wave) frequency effect on damping was analyzed and it was concluded that the chain damping contribution to the total damping may increase significantly due to the superposition of low frequency surge and high frequency heave motions.

A similar approach was pursued by W.C. Webster (1995), but including the internal (material) damping of the mooring line in addition to the drag damping. Through various parametric studies, an attempt was made to provide comprehensive information for the optimal design of mooring lines so as to access a maximum amount of damping. The studies investigated variations in pretension, motion amplitude and frequency, drag coefficient, stiffness, current and scope.

Instead of using estimates of the low frequency-averaged chain damping described above, Dercksen, et al (1992) presented a direct simulation method for the correct instantaneous low and high frequency motions of a turret-moored tanker. For the correct coupling between high and low frequency motion, each equation of motion for the tanker and mooring lines is solved respectively for the low frequency surge motion and for the combined high and low frequency motion. The linear and quadratic transfer functions derived from wave diffraction theory are used to force the high and low frequency motions of the tanker. It was suggested that the direct coupling of high and low frequency motions can predict the correct momentary chain damping.

Yuh-Lin Hwang (1998) simulated a surge decay test with a numerical model of the coupled tanker and mooring-riser system to evaluate the mooring line damping. Determination of the mooring line damping, which was linearized based on the principle

of energy conservation, was conducted by analyzing the peaks of the free vibration response through a log-decrement technique. The results indicated that with increasing water depth mooring damping increases due to the effects of current and the coupling between the high and low frequency motions, and the riser contribution considerably increases the total mooring damping as well.

M.S. Triantafyllou, et al (1994) introduced the drag amplification factor to calibrate the conventional drag coefficient to reflect the effect of vortex-induced vibrations (VIV) and of wave-slow motion interaction. The amplification due to VIV is caused by the substantial changes in the vortex formation process that occur during VIV. The amplification due to the motion interaction is a nonlinear function of amplitude and frequency of the wave motions. They proposed that considering both effects on drag might considerably increase the total mooring damping to a level compatible to the wave-drift damping associated with the vessel motions.

1.3. Objectives and Scope

In the previous section, a number of studies associated with the hydrodynamic force acting on a slender body were reviewed mainly in respect to modeling methodology. However, it can be noted that none of these studies seem to be applicable to the calculation and decomposition of fluid force on a moving object with a complicated shape, such as chain links, due to the numerical and experimental limitations introduced by such complexity. Accordingly, there is a need for an alternative approach of force estimation which can minimize the problem related to body shape and which can be

brought to realization when the conventional slender body dynamics formulation is combined with the advanced optical tracking of body motion in calm water.

The ultimate objective of the present research is to develop efficient, repeatable, automated, low cost, and standardized measurement techniques for estimation of Morison drag and inertia coefficients for slender body elements at prototype and model scale over the full operating range of Re and KC number for three-dimensional flow situations that include combined non-collinear slow drift and wave frequency motions. This is accomplished by the works listed below:

1. Modeling the hydrodynamic force acting on chain and cable elements is done by estimation of the rational force transfer coefficients (drag and added mass coefficients) through laboratory model tests in two dimensional conditions. For the full operating range of Reynolds number and Keulegan-Carpenter number, both small and relatively large scale model tests are carried out for two different types of motion: free oscillation and forced oscillation of the chain/cable in still water.

2. Analysis of the experimental data is progressed in two different ways:

    i. Direct values of the coefficients are extracted from the derived drag and inertia force (for the free oscillation tests).

    ii. Fourier-averaged values of the coefficients are extracted from the derived total normal force (for the forced oscillation tests only).

3. Two forms of equations of motion in partial differential form are employed for describing the motion of the chain/cable. Results obtained with both equations are compared to propose the better estimating system equation.

4. With the force coefficients obtained from experiments, the validation of the method of data analysis is implemented by comparison of motion results between model tests and computer simulation. Numerical simulations are conducted using the commercial program "OrcaFlex". OrcaFlex has the capability to simulate the motion of a single or multiple mooring line system attached to a floating platform with user-input Morison drag and added mass coefficients that may be specified as a function of the Reynolds number.

The appropriateness of the Morison equation is tested for certain relative fluid-body interaction regimes characterized by the degree of relative importance of the drag and inertia forces. Since many researchers have shown that the Morison equation is not quite suitable for all regimes in several cases of different shaped bodies including circular cylinders, assessment of the equation should be performed for chain as well. This assessment is also needed for the validation of the force coefficients derived from the experiments, and will be included in the discussion of free oscillation tests.

Finally, the damping effect of a mooring line undergoing forced oscillation is investigated briefly. Since a moored offshore structure experiences both high (wave) and low frequency motion, tests at various different frequencies are required to demonstrate the frequency effect of mooring line damping. The contribution of the Morison force coefficients to the damping effect provided by the mooring line to the floater will be also studied by conducting a numerical simulation once with the flow-dependent coefficients obtained herein and once with representative single valued flow-independent coefficients as applied in typical design practice.

1.4. Outline of Dissertation

Chapter II presents all of the theoretical and numerical techniques used in the analysis of the experimental data to estimate the hydrodynamic force and its coefficients. Morison's force model, slender body dynamics and the incorporated computing process for force estimation are explained first. Then the methodologies used for the estimation of force transfer coefficients are described. Lastly, a novel procedure for estimation of bending stiffness of wire is introduced.

Chapter III is divided into two sections. The first section provides information regarding the experimental set-up of each test and the properties of the mooring lines tested. In the second section, the detailed procedures for experimental data processing are discussed, such as optical tracking calibration, data reconstruction, data filtering, and error analysis.

In Chapter IV results of the bending stiffness measurement, free oscillation tests, and forced oscillation tests are presented and discussed. Also, the resistance provided by mooring lines to floater motions is investigated by comparison between using the conventional values of force coefficients and the experimentally-derived coefficients.

Finally, concluding remarks and future work related to the present topic are given in Chapter V.

CHAPTER II

THEORETICAL MODELING OF MOORING LINE DYNAMICS

2.1. Introduction

Both physical and numerical experiments of an oscillating mooring line in 2-dimension have been performed to date. Since the nature of the problems addressed in free oscillation and forced oscillation tests are somewhat different, the corresponding assumptions and analysis techniques are specified separately for each case. Due to experimental difficulties, torsional motion and friction between each chain link will not be considered throughout the entire analysis even though their contribution to the hydrodynamic behavior of an oscillating mooring line is not negligible.

To model the detailed dynamics, the mooring line is discretised into individual segments whose positions are known (i.e. measured) for each time step. The discretised form of the equation of force equilibrium is then applied for each segment at each time step to estimate the total hydrodynamic force on the line. For simplicity, it is assumed that Morison's equation well represents the hydrodynamic force on the slender body, excluding 3-D effects such as vortex-induced vibrations (VIV).

In general, three different components of the hydrodynamic force exist: tangential, normal, and bi-normal components relative to the local axis of the mooring line. Among these three, the normal and bi-normal force components are generally an order of magnitude larger than the tangential force component. Since extracting the tangential force coefficients with some degree of accuracy by the experimental technique

presented herein does not seem possible, known representative values of tangential coefficients are incorporated with Morison's equation. Due to the unavailability of 3-D data (that is, only 2D experiments were performed), the bi-normal component is excluded in the analysis. However as the length of the mooring line may be quite long, the tangential force component should be considered for better evaluation of the dynamic behavior of the mooring line.

2.2. Morison Equation

Hydrodynamic forces on a slender body can be modeled with the well known Morison's equation. The conventional form of Morison's equation used to model the normal component of hydrodynamic force F_N on a slender body is

$$F_N = F_D + F_A = \frac{1}{2} C_D \rho D L V |V| + \frac{1}{4} C_A \pi \rho D^2 L \frac{dV}{dt} \qquad (2.1)$$

in which $\qquad C_D$ and C_A : drag and added mass coefficients, respectively

V : instantaneous velocity of the body relative to the fluid

D : characteristic dimension of the body normal to the flow

L : length of slender body subjected to fluid force

ρ : fluid density.

The tangential and bi-normal force components are expressed similarly to the above equation and the detailed explanation will be given later. The drag force term for the normal direction is mainly associated with pressure drag while the tangential drag force component is primarily associated with friction drag. Force coefficients for each term can be obtained from the derived hydrodynamic force by means of several different

methods such as least square minimization, Fourier averaged analysis, and stochastic analysis, as reviewed in section 1.2.2.

2.3. Governing Parameters

Before the estimation of Morison's force coefficients, the governing parameters that forces are dependent on should be determined, for instance, viscosity, flow conditions, and characteristics of body (dimensions, roughness, etc…). Simple dimensional analysis of oscillatory slender body motion in fluids leads to the following relationship:

$$\frac{F_N}{0.5\,\rho\,D\,L\,V^2} = f\left(V\,T\,/\,D, \quad V\,D\,/\,v\right) = f\left(\text{KC, Re}\right) \tag{2.2}$$

Since the relation between fluid force and other parameters not listed in Equation (2.2), such as roughness, upstream turbulence level, etc…, can hardly be resolved through the present analysis methodology, those parameters are not incorporated in the dimensional analysis.   To reconcile Equations (2.1) and (2.2),

$$C_D = g\left(\text{KC, Re}\right)$$
$$C_A = h\left(\text{KC, Re}\right) \tag{2.3}$$

where T : period of oscillation

D, L : diameter & length of body

v : kinematic viscosity

Re   : Reynolds number

KC   : Keulegan-Carpenter number.

The Keulegan-Carpenter number represents the displacement ratio of flow over the body under oscillating flow conditions (fluid particle displacement relative to body

dimension) and is a most appropriate parameter for characterizing the periodic motion of the body in the fluid.   However, for free oscillations of a mooring line in water because the damping is over-critical, the KC number is effectively infinite so the fluid-body interaction is characterized by the Reynolds number only.

The Reynolds number is the ratio of the inertia force to the viscous force, which is well correlated with the drag force under non-harmonic motion.   Both parameters have been widely employed by many researchers to characterize the fluid-structure interaction regime in presenting the correlation with drag and added mass coefficients.   The combination of KC and Re, the so-called frequency parameter, can also be used as a suitable non-dimensional parameter for purposes of correlating with the force coefficients.   Thus, the present research will seek to correlate Morison force coefficients with the parameters stated above.

2.4. Equations of Motion

We are interested in measuring the local hydrodynamic forces on mooring lines under characteristic operating conditions.   However it is not practical to directly measure the external force on a mooring line that is itself responding dynamically to applied forcing. It is therefore necessary to invoke the equation of motion for the mooring line, which expresses the dynamic force equilibrium at each instant of time.   The applied hydrodynamic force can be derived through direct measurement of all other quantities that contribute to the dynamic equilibrium.
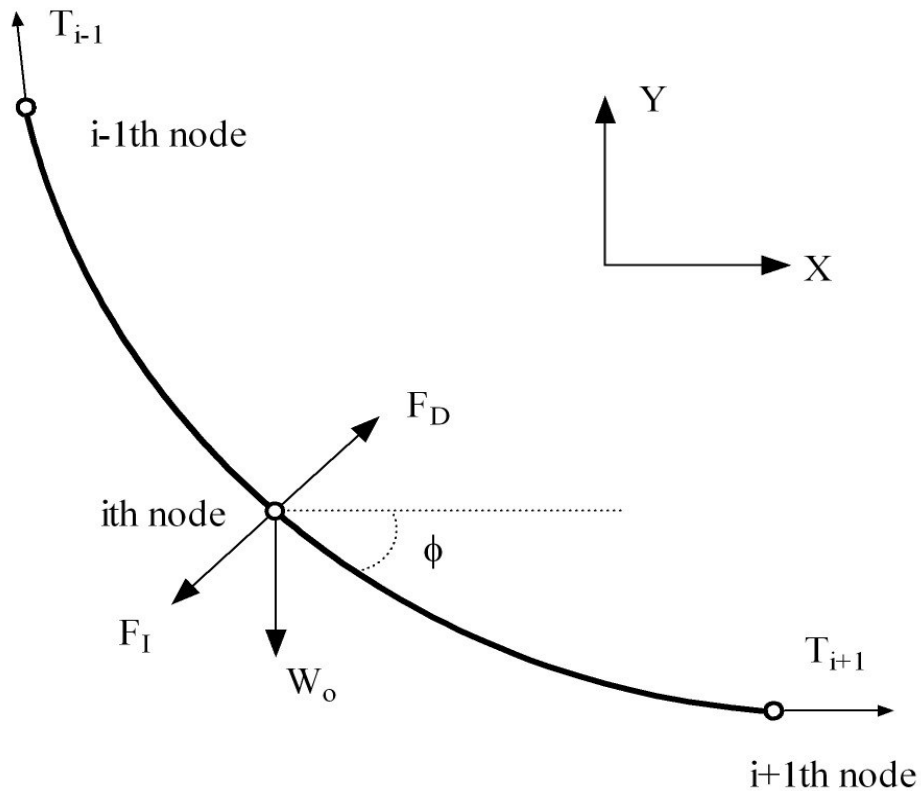
Figure 2.1   Free body diagram of lumped mass body (where F_D : drag force, F_I :

inertia force, T_n : tension at n-th node, W_o : net weight)

   This section describes two alternative, but equivalent, approaches for expressing the equation of motion, both of which are based on Frenet's formula representing curves in space.   One approach is founded on a global rectangular (XYZ) coordinate system (R.P. Nordgren, 1974) while the alternative is based on a natural (TNB) coordinate system, which is the coordinate system moving with the body (A.Bliek, 1984, and C.T. Howell, 1992).   For both methods, the mooring line is discretized into a finite number of segments, each of which must be in dynamic equilibrium according to the equation of

motion. All properties (weight, buoyancy, hydrodynamic force etc.) on each segment are lumped to corresponding node points along the segment (Figure 2.1). In the following two subsections the essential procedure for derivation for each equation of motion will be summarized.

2.4.1. Theory Based on Natural Coordinate System

First we define the directional vector in a natural (TNB) coordinate system. As illustrated in Figure 2.2, the tangential vector $\vec{t}$ is tangent to the local curve of the mooring line and the normal vector $\vec{n}$ is at right angle to the local curve, pointing to the local center of curvature of the mooring line. The binormal vector $\vec{b}$ is then the cross vector product of the tangential and normal vectors. All of the directional unit vectors are functions of time (t) and arc-length (s),

$$\text{TNB} = [\,\vec{t}(t,s),\ \vec{n}(t,s),\ \vec{b}(t,s)\,]$$

Assuming the mooring line is inextensible, which means the line is not subjected to axial strain and the length of line remains constant at all time, the vectors follow Frenet's relation,

$$\frac{\partial \vec{t}}{\partial s} = \frac{1}{k}\,\vec{n}$$

$$\frac{\partial \vec{b}}{\partial s} = -\frac{1}{\tau}\,\vec{n} \tag{2.4}$$

$$\frac{\partial \vec{n}}{\partial s} = \frac{1}{\tau}\,\vec{b} - \frac{1}{k}\,\vec{t}$$

where k is the radius of curvature and τ is the radius of torsion.

The assumption of inextensibility is made in recognition of the fact that for the chain and wire rope mooring elements that will be tested the axial strains will be negligible. For mooring elements where axial strains are significant, such as polyester rope, the effects of axial stiffness can be incorporated straightforwardly in the equations of motion and do not pose any new challenges.
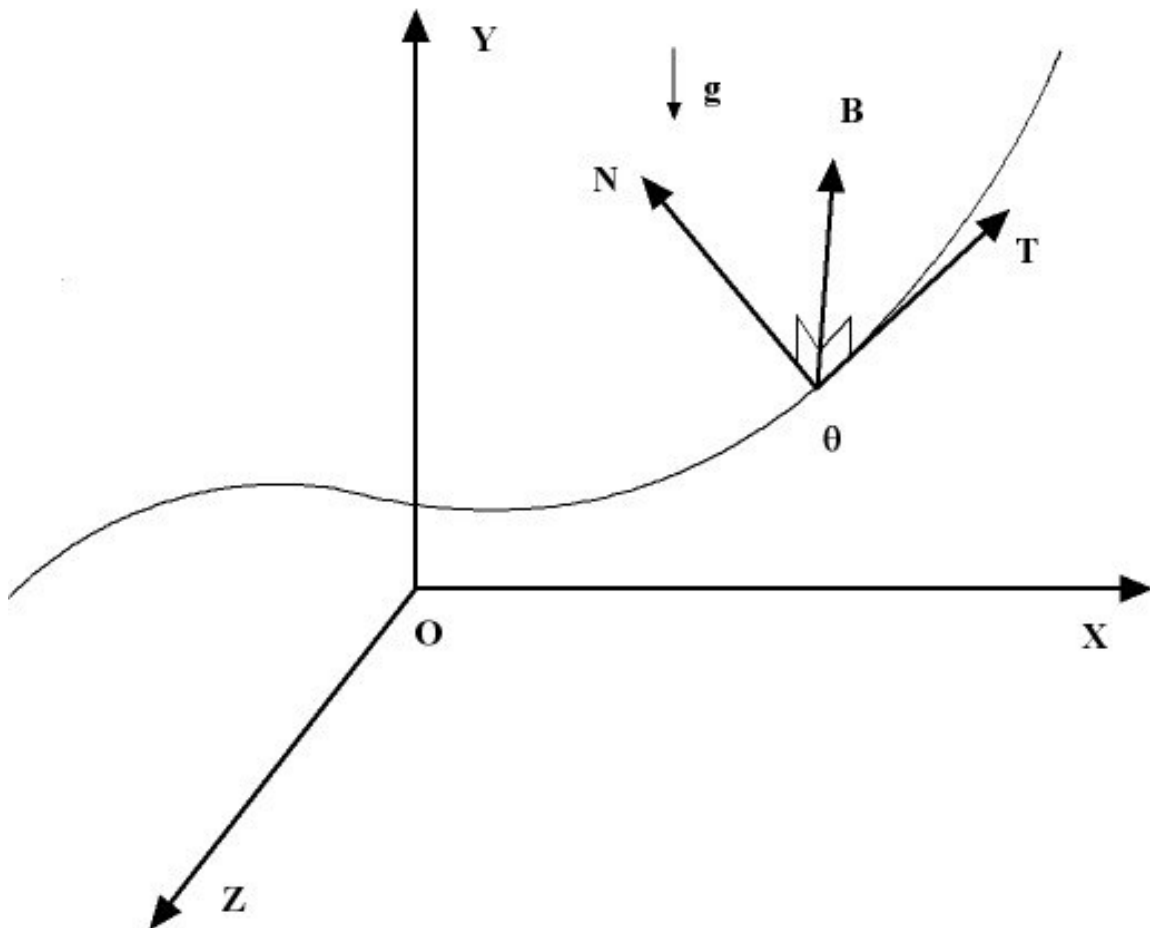
Figure 2.2   Definition of natural coordinate system

Before building up the dynamic equation for the mooring line, one should define the derivatives of the vectors with respect to time and space as well. Consider a vector $\vec{V}(t,s)$ along the line,

$$\vec{V} = V_1 \vec{t} + V_2 \vec{n} + V_3 \vec{b} \tag{2.5}$$

The space derivative of $\vec{V}$ in the TNB coordinate system is defined as

$$\frac{D\vec{V}}{Ds} = \frac{\partial \vec{V}}{\partial s} + \vec{\Omega} \times \vec{V} \tag{2.6}$$

where

$$\frac{\partial \vec{V}}{\partial s} = \left[\frac{\partial V_1}{\partial s}, \frac{\partial V_2}{\partial s}, \frac{\partial V_3}{\partial s} \right] \;,$$

$$\vec{\Omega} = \left(\frac{\partial \vec{n}}{\partial s} \cdot \vec{b} \right) \vec{t} + \left(\frac{\partial \vec{b}}{\partial s} \cdot \vec{t} \right) \vec{n} + \left(\frac{\partial \vec{t}}{\partial s} \cdot \vec{n} \right) \vec{b}$$

$$= \frac{1}{\tau} \vec{t} + \frac{1}{k} \vec{b} = (\Omega_1, \Omega_2, \Omega_3) \;\; : \text{Darboux vector (or local curvature vector)}$$

Similarly, the time derivative (Lagrangian derivative) in the TNB coordinate system is

$$\frac{D\vec{V}}{Dt} = \frac{\partial \vec{V}}{\partial t} + \vec{\omega} \times \vec{V} \tag{2.7}$$

where

$$\frac{\partial \vec{V}}{\partial t} = \left[\frac{\partial V_1}{\partial t}, \frac{\partial V_2}{\partial t}, \frac{\partial V_3}{\partial t} \right] \;,$$

$$\vec{\omega} = \omega_1 \vec{t} + \omega_2 \vec{n} + \omega_3 \vec{b} \qquad : \quad \text{rotation vector.}$$

Both derivatives have a term associated with a vector cross product, one with the Darboux vector and the other with the rotation vector, which is different from the derivatives in the conventional fluid dynamics where the advective derivative term replaces the cross product term in the time derivative, following the Eulerian description of motion.

The fundamental equation of motion for an infinitesimal length of line with the specified derivatives above is

$$m \left[\frac{\partial \vec{V}}{\partial t} + \vec{\omega} \times \vec{V} \right] ds = \sum \vec{F}_{Ap} \, ds + \sum \vec{F}_{Int} \, ds \qquad (2.8)$$

where

m : mass of line per unit length

$\vec{\omega}$: rotation vector

$\vec{F}_{Ap}$: applied force per unit length

$\vec{F}_{Int}$: internal force per unit length

$\vec{V} = V_1 \vec{t} + V_2 \vec{n} + V_3 \vec{b}$: velocity vector of a node in natural coordinates.

Weight, hydrostatic force, and hydrodynamic force are the applied forces acting on a submerged line. The net submerged weight per unit length of line is the sum of the weight and buoyancy forces,

$$W_0 = (m - \rho_w A) g \qquad (2.9)$$

where A is the cross-sectional area of the line.

The Morison-type hydrodynamic force on a slender body is decomposed into three directional components,

$$\vec{F}_{Hd} \;=\; F_t \vec{t} \;+\; F_n \vec{n} \;+\; F_b \vec{b} \tag{2.10}$$

where all three directional forces consist of both drag and added mass forces.

After applying all the external forces, the internal forces on each line element should be addressed. Along with tension, the internal forces due to material friction, torsional stiffness, axial stiffness, and bending stiffness should be considered. However due to the relatively small effect of friction, axial strain and torsion on the hydrodynamics, only the tension and shear forces resulting from bending stiffness are retained, which seems to provide sufficient accuracy for the estimation of the hydrodynamic force coefficients. The internal force on a differential element can be expressed as:

$$\frac{D\vec{T}}{Ds} \, ds \;=\; \left[\frac{\partial \vec{T}}{\partial s} \;+\; \vec{\Omega} \times \vec{T} \right] ds \tag{2.11}$$

where

$\vec{T} \;=\; T_t \vec{t} \;+\; S_n \vec{n} \;+\; S_b \vec{b}$: internal force vector

T_t, S_n, S_b : tension and shear forces in normal and binormal directions.

Combining equations (2.8) through (2.11) yields the general mooring line dynamic equation in the TNB natural coordinate system,

$$m\left(\frac{\partial \vec{V}}{\partial t} \;+\; \vec{\omega} \times \vec{V} \right) \;=\; \frac{\partial \vec{T}}{\partial s} \;+\; \vec{\Omega} \times \vec{T} \;-\; W_o \hat{k} \;-\; \left(F_t \vec{t} \;+\; F_n \vec{n} \;+\; F_b \vec{b} \right) \tag{2.12}$$

where

$\hat{k}$: vertical unit vector in terms of the natural vector (positive upward)

F_t, F_n, F_b : components of hydrodynamic forces in tangential, normal, and bi-

normal directions

To incorporate the bending stiffness of the material, moment equilibrium must be introduced as follows:

$$\frac{D}{Dt}\left[I_m\,\vec{\omega}\right] \;=\; \frac{D\vec{M}}{Ds} \;+\; d\vec{r}\times\vec{F}_{Ap} \;+\; \frac{d\vec{r}}{ds}\times\vec{T} \tag{2.13}$$

where I_m : mass moment of inertia per unit length

$\vec{r}$: position vector

$\vec{M}$: internal moment vector

The internal moment vector due to bending and torsional stiffness has three directional components,

$$\vec{M} \;=\; G\,I_P\,\Omega_1\,\vec{t} \;+\; EI\,\Omega_2\,\vec{n} \;+\; EI\,\Omega_3\,\vec{b} \tag{2.14}$$

where G : shear modulus

E : Young's modulus

I_P : polar moment

I : sectional second moment.

As $d\vec{r}$ approaches zero and the rotational inertia becomes negligible equation (2.13) reduces to

$$\frac{D\vec{M}}{Ds} \;+\; \vec{t}\times\vec{T} \;=\; 0 \tag{2.15}$$

The three directional components of the governing equations can be expressed in terms of Euler angles which define the position of the natural (TNB) coordinate system relative to the global Cartesian (XYZ) coordinate system. To determine the transformation matrix, initially the mooring line element is considered to be aligned with the horizontal X axis, and then it starts to experience the angular and translational motion. According to the assumption of no torsional motion of the line, only two Euler

angle rotations are defined for the coordinate transformation. The rotation sequence is defined in Figure 2.3.
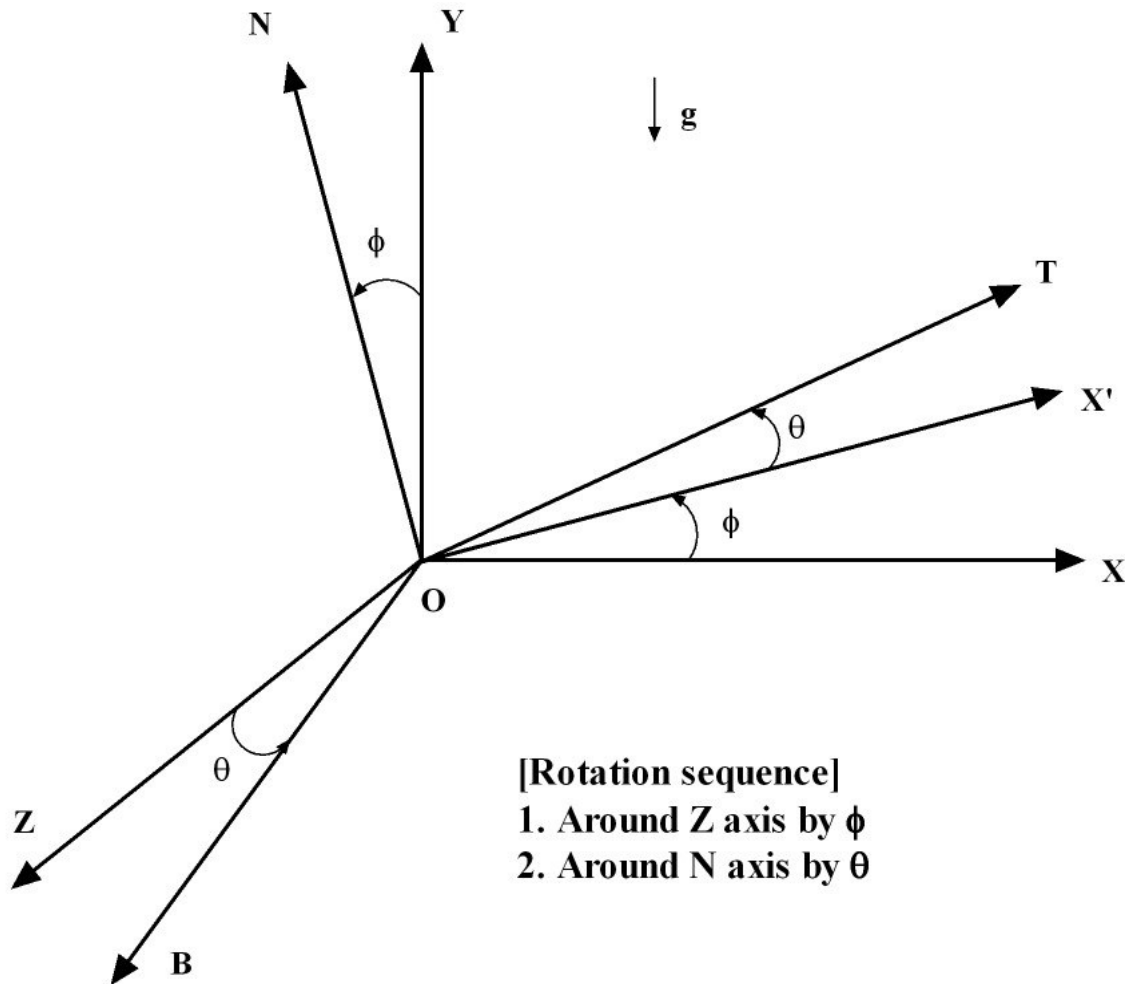
Figure 2.3   Cartesian (XYZ) to natural (TNB) coordinate transformation

There are many different orders of rotation that one can apply if rotations around all

three axes are involved. Determining the sequence of rotation is a very important issue because it can affect the entire dynamic solution of the mooring line, including the calculated hydrodynamic forces. The rotation sequence used in the present work showed better efficiency for the estimation of force coefficients than the reversed sequence when a 3-D problem is addressed. This is because the tension plays a key role in the estimation of fluid force through solid dynamics, and the tension is not coupled with the equilibrium equation for the binormal direction when the reversed sequence is chosen. Consequently, both the tension and the hydrodynamic force can be distorted in the dynamic calculation. The efficiency of these two rotation sequences can be measured by comparing the backwardly estimated coefficients from the motion data simulated with the pre-defined coefficients.

The coordinate transformation from global to natural coordinates can be accomplished by applying the following matrix transformation:

$$
\begin{bmatrix} T \\ N \\ B \end{bmatrix} = \begin{bmatrix} \cos\phi\cos\theta & \sin\phi\cos\theta & -\sin\theta \\ -\sin\phi & \cos\phi & 0 \\ \cos\phi\sin\theta & \sin\phi\sin\theta & \cos\theta \end{bmatrix} \begin{bmatrix} X \\ Y \\ Z \end{bmatrix}
\tag{2.16}
$$

The rotation vector, the vertical unit vector, and the Darboux vector in Euler angles are given as

$$
\vec{\omega} = \left(-\dot{\phi}\sin\theta\right)\vec{t} + \left(\dot{\theta}\right)\vec{n} + \left(\dot{\phi}\cos\theta\right)\vec{b}
\tag{2.17}
$$

$$
\vec{k} = \left(\sin\phi\cos\theta\right)\vec{t} + \left(\cos\phi\right)\vec{n} + \left(\sin\phi\sin\theta\right)\vec{b}
\tag{2.18}
$$

$$
\vec{\Omega} = \left(-\sin\theta\,\frac{\partial\phi}{\partial s}\right)\vec{t} + \left(\frac{\partial\theta}{\partial s}\right)\vec{n} + \left(\cos\theta\,\frac{\partial\phi}{\partial s}\right)\vec{b}
\tag{2.19}
$$

Using equation (2.17) through equation (2.19), the equations of motion for each

directional component in natural coordinates are written as

$$m \left[\frac{\partial u}{\partial t} + w\dot{\theta} - v\dot{\phi} \cos\theta \right] = \frac{\partial T_t}{\partial s} + S_b \frac{\partial \theta}{\partial s} - S_n \frac{\partial \phi}{\partial s} \cos\theta + F_t - W_0 \sin\phi \cos\theta$$

$$m \left[\frac{\partial v}{\partial t} + w\dot{\phi} \cos\theta + u\dot{\phi} \cos\theta \right] = T_t \frac{\partial \phi}{\partial s} \cos\theta + \frac{\partial S_n}{\partial s} + S_b \frac{\partial \phi}{\partial s} \sin\theta + F_n - W_0 \cos\phi$$

$$m \left[\frac{\partial w}{\partial t} - u\dot{\theta} - v\dot{\phi} \sin\theta \right] = \frac{\partial S_b}{\partial s} - S_n \frac{\partial \phi}{\partial s} \sin\theta - T_t \frac{\partial \theta}{\partial s} + F_b - W_0 \sin\phi \sin\theta \qquad \textbf{(2.20)}$$

$$S_n = -EI \left[\frac{\partial^2 \phi}{\partial s^2} \cos\theta + \frac{\partial \phi}{\partial s} \frac{\partial \cos\theta}{\partial s} - \frac{\partial \theta}{\partial s} \frac{\partial \phi}{\partial s} \sin\theta \right]$$

$$S_b = EI \left[\frac{\partial^2 \theta}{\partial s^2} + \left(\frac{\partial \phi}{\partial s} \right)^2 \cos\theta \sin\theta \right]$$

where u, v, w are the velocity components in tangential, normal, and binormal directions, respectively. For a two dimensional problem constrained to the plane of the mooring line, the equations of motion are simplified as below.

$$m \left[\frac{\partial u}{\partial t} - v\dot{\phi} \right] = \frac{\partial T_t}{\partial s} - S_n \frac{\partial \phi}{\partial s} + F_t - W_0 \sin\phi$$

$$m \left[\frac{\partial v}{\partial t} + u\dot{\phi} \right] = T_t \frac{\partial \phi}{\partial s} + \frac{\partial S_n}{\partial s} + F_n - W_0 \cos\phi \qquad \textbf{(2.21)}$$

$$S_n = -EI \left[\frac{\partial^2 \phi}{\partial s^2} \right]$$

2.4.2. Theory Based on Global Coordinate System

The motion of a mooring line element is expressed in terms of the position of the central axis of the line in a space curve defined by the position vector $\vec{r}(s,t)$, which is a function of the arc length along the curve and time. On the curve, the unit tangent vector $\vec{t}$, the unit normal vector $\vec{n}$, and the unit binormal vector $\vec{b}$ are defined by

$$\vec{t} = \vec{r}', \quad \vec{n} = \vec{t}'/k, \quad \vec{b} = \vec{t} \times \vec{n} \tag{2.22}$$

where the prime denotes differentiation with respect to arc length and k denotes the local radius of curvature.

The internal state of stress at a point on the line element is described by the resultant force $\vec{F}$. The dynamic force balance is given by:

$$\vec{F} + \vec{Q} = m\ddot{\vec{r}} \tag{2.23}$$

where $\vec{Q}$: applied force per unit length

m : mass per unit length.

The resultant force $\vec{F}$ has contributions from bending stiffness and tangential force on the mooring line,

$$\vec{F} = -(EI\,\vec{r}'')' + \lambda\,\vec{r}' \tag{2.24}$$

where EI is the bending stiffness of the material and λ is a Lagrangian multiplier resulting from the assumption of inextensibility of the mooring line. Applying Frenet's formula yields

$$\lambda = \vec{F} \cdot \vec{r}' - EI\,k^2 = T - EI\,k^2 \tag{2.25}$$

where T is the tension in the line and k is the line curvature, which is defined as the absolute value of the second spatial derivative of the position vector $\vec{r}(s,t)$.

All of the remaining forces, including weight, buoyancy force, and hydrodynamic force, can be considered as the applied force,

$$\vec{Q} = \vec{W} + \vec{B} + \vec{F}_{Hd} = W_0\hat{k} + (\vec{F}_t + \vec{F}_n + \vec{F}_b) \tag{2.26}$$

The hydrodynamic force consists of the inertia and drag forces in all three directions of the TNB coordinate system. One could also include the hydrodynamic lift force, which can cause vortex-induced vibrations (VIV), however this will not be considered here for the sake of simplicity.

Substituting equations (2.24)-(2.26) into (2.23) and neglecting torsion and the bending stiffness, the general equations of motion for a mooring line element in the global coordinate system can be written as

$$m\left(\frac{\partial^2\vec{r}}{\partial t^2} + \vec{\omega}\times\frac{\partial\vec{r}}{\partial t}\right) = \frac{\partial\vec{T}}{\partial s}\frac{\partial\vec{r}}{\partial s} + \vec{T}\frac{\partial^2\vec{r}}{\partial s^2} - W_o\hat{k} - \left(\vec{F}_t + \vec{F}_n + \vec{F}_b\right)$$

$$- EI\left[\frac{\partial^4\vec{r}}{\partial s^4} + \left|\frac{\partial^2\vec{r}}{\partial s^2}\right|^2\left(\frac{\partial\vec{r}}{\partial s} + \frac{\partial^2\vec{r}}{\partial s^2}\right)\right] \tag{2.27}$$

where

    m : mass of line per unit length

    $\vec{\omega}$: rotation vector

    $\vec{T}$: tension vector

    W_o : submerged weight of line per unit length

    $\vec{r}(s, t)$: space curve

F_t, F_n, F_b : tangential, normal, and bi-normal components of hydrodynamic

forces.

Note that the time derivative of the acceleration term is replaced by the Lagrangian derivative in order to include the effect of rotational motion of the mooring line. The rotation vector used here involves two axes only, the Y and Z axes, since torsional motion has been neglected, that is,

$$\vec{\omega} = \dot{\theta} \cdot \hat{i} + \dot{\phi} \cdot \hat{k} \tag{2.28}$$

The rotation sequence for coordinate transformation is given in the previous section (see Figure 2.3). The hydrodynamic forces in natural coordinates should be transformed into the global coordinate system by using the following transformation matrix:

$$\begin{bmatrix} X \\ Y \\ Z \end{bmatrix} = \begin{bmatrix} \cos\phi\cos\theta & -\sin\phi & \cos\phi\sin\theta \\ \sin\phi\cos\theta & \cos\phi & \sin\phi\sin\theta \\ -\sin\theta & 0 & \cos\theta \end{bmatrix} \begin{bmatrix} T \\ N \\ B \end{bmatrix} \tag{2.29}$$

which is the inverse of the transformation matrix in equation (2.16).

Rewriting the equations for each directional component in the global coordinate system yields

$$m\left[\ddot{x} + \dot{z}\dot{\theta} - \dot{y}\dot{\phi}\right] = \frac{\partial T}{\partial s}\frac{\partial x}{\partial s} + T\frac{\partial^2 x}{\partial s^2} - F_t\cos\phi\cos\theta + F_n\sin\phi - F_b\cos\phi\sin\theta$$

$$- EI\left[\frac{\partial^4 x}{\partial s^4} + \left|\frac{\partial^2 \vec{r}}{\partial s^2}\right|^2\left(\frac{\partial x}{\partial s} + \frac{\partial^2 x}{\partial s^2}\right)\right]$$

$$m\left[\ddot{y} + \dot{x}\dot{\phi}\right] = \frac{\partial T}{\partial s}\frac{\partial y}{\partial s} + T\frac{\partial^2 y}{\partial s^2} - F_t \sin\phi \cos\theta - F_n \cos\phi - F_b \sin\phi \sin\theta$$

$$- W_0 - EI\left[\frac{\partial^4 y}{\partial s^4} + \left|\frac{\partial^2 \vec{r}}{\partial s^2}\right|^2\left(\frac{\partial y}{\partial s} + \frac{\partial^2 y}{\partial s^2}\right)\right]$$

(2.30)

$$m\left[\ddot{z} - \dot{x}\dot{\theta}\right] = \frac{\partial T}{\partial s}\frac{\partial z}{\partial s} + T\frac{\partial^2 z}{\partial s^2} + F_t \sin\theta - F_b \cos\theta$$

$$- EI\left[\frac{\partial^4 z}{\partial s^4} + \left|\frac{\partial^2 \vec{r}}{\partial s^2}\right|^2\left(\frac{\partial z}{\partial s} + \frac{\partial^2 z}{\partial s^2}\right)\right]$$

where

$$\left|\frac{\partial^2 \vec{r}}{\partial s^2}\right|^2 = \left(\frac{\partial^2 x}{\partial s^2}\right)^2 + \left(\frac{\partial^2 y}{\partial s^2}\right)^2 + \left(\frac{\partial^2 z}{\partial s^2}\right)^2.$$

In the case of two dimensional motions constrained in the plan of the line, the equations of motion are reduced to

$$m\left[\ddot{x} - \dot{y}\dot{\phi}\right] = \frac{\partial T}{\partial s}\frac{\partial x}{\partial s} + T\frac{\partial^2 x}{\partial s^2} - F_t \cos\phi + F_n \sin\phi$$

$$- EI\left[\frac{\partial^4 x}{\partial s^4} + \left|\frac{\partial^2 \vec{r}}{\partial s^2}\right|^2\left(\frac{\partial x}{\partial s} + \frac{\partial^2 x}{\partial s^2}\right)\right]$$

(2.31)

$$m\left[\ddot{y} + \dot{x}\dot{\phi}\right] = \frac{\partial T}{\partial s}\frac{\partial y}{\partial s} + T\frac{\partial^2 y}{\partial s^2} - F_t \sin\phi - F_n \cos\phi$$

$$- W_0 - EI\left[\frac{\partial^4 y}{\partial s^4} + \left|\frac{\partial^2 \vec{r}}{\partial s^2}\right|^2\left(\frac{\partial y}{\partial s} + \frac{\partial^2 y}{\partial s^2}\right)\right]$$

2.5. Computational Approach

The equations of motion in both coordinate systems are quite similar to each other and have the same number of variables including velocity, acceleration, tension, angle, etc. Excluding all the variables associated with kinematics, which can be obtained from the measured position vector by using the finite difference method (forward, central or backward difference), only the top tension and each component of the hydrodynamic force are left as unknown variables. As previously mentioned, the tangential force may be neglected. Alternatively, we may combine the normal and binormal forces into one component to reduce the number of unknown variables if a three-dimensional problem is considered. The equations in both coordinate systems then become a complete, closed system with known top (or bottom) tension which is also provided by direct measurements. The equations can be solved explicitly or implicitly by adjusting the starting node point for the computation. For example, when considering the case of forced or free oscillations, for an implicit scheme the computation may start with the second node from the top or bottom end, while for an explicit scheme the computation may start with the first end node. Hereafter, the overall process of dynamic calculation is presented in the order of computation.

2.5.1. Kinematics

Moving chain or cable elements generally undergo translational and angular motion, thus kinematics for both types of motion are required for dynamic analysis and can be

calculated by means of the 3-point central difference method applied to position measurements. To increase accuracy, a 5-point differencing scheme can be applied. For the initial and last frames, forward and backward difference schemes are employed. Since the kinematics are measured in a global coordinate frame of reference, kinematics related to the translational motion should be transformed into the natural coordinate system through the coordinate transformation matrix previously provided.

Angular velocity and acceleration

$$\dot{\theta}^{i,q} = \frac{\theta_i^{q+1} - \theta_i^{q-1}}{2\,h}$$

$$\ddot{\theta}^{i,q} = \frac{\theta_i^{q+1} - 2\,\theta_i^q + \theta_i^{q-1}}{h^2}$$

(2.32)

Translational velocity and acceleration

$$\dot{X}^{i,q} = \frac{X_i^{q+1} - X_i^{q-1}}{2\,h}$$

$$\ddot{X}^{i,q} = \frac{X_i^{q+1} - 2\,X_i^q + X_i^{q-1}}{h^2}$$

(2.33)

where q :   the time step index

   h :   the time interval between successive measured positions

   i :   the node point index.

Alternatively, the 5-point central difference scheme is

$$\dot{X}^{i,q} = \frac{-X_i^{q+2} + 8\,X_i^{q+1} - 8\,X_i^{q-1} + X_i^{q-2}}{12\,h}$$

(2.34)

$$\ddot{X}^{i,q} = \frac{-X_i^{q+2} + 16\,X_i^{q+1} - 30\,X_i^{q} + 16\,X_i^{q-1} - X_i^{q-2}}{12\,h^2}$$

2.5.2. Hydrodynamic Forces

As previously mentioned, Morison's formula is assumed to represent the hydrodynamic force on slender body elements. The hydrodynamic force is comprised of the drag and inertia force components. Each force has three directional (tangential, normal and binormal) components, each with its own force coefficients in the natural coordinate system.

Drag force: tangential, normal, and binormal components

$$F_{Dt}^{i,q} = \frac{1}{2}\rho \cdot \pi \cdot D \cdot L^{i,q} \cdot C_{Dt} \cdot V_t^{i,q}\left|V_t^{i,q}\right|$$

$$F_{Dn}^{i,q} = \frac{1}{2}\rho \cdot D \cdot L^{i,q} \cdot C_{Dn} \cdot V_n^{i,q}\left|V_n^{i,q}\right| \qquad\qquad \textbf{(2.35)}$$

$$F_{Db}^{i,q} = \frac{1}{2}\rho \cdot D \cdot L^{i,q} \cdot C_{Db} \cdot V_b^{i,q}\left|V_b^{i,q}\right|$$

where subscripts *t*, *n*, *b* denote the tangential, normal, and binormal directions, respectively. Since the dynamics of the mooring line are computed with a finite number of discretized segments, the nonlinear velocity-squared terms in the formulas for the normal and binormal components should be replaced with averaged values over the length of each element to include the effect of angular motion. The averaged normal velocity-squared term for the two different cases of segment motion can be calculated

through integration over the length of each segment.

For $\dfrac{\dot{\phi}}{2} \leq V_n$

$$V_n^{i,q}\left|V_n^{i,q}\right| = \frac{1}{L}\int\limits_{-L/2}^{L/2}(V_n^{i,q} + \dot{\phi}r)^2\,dr = \frac{sign(V_n^{i,q})}{L^{i,q}}\left[(V_n^{i,q})^2 L^{i,q} + \frac{1}{12}\dot{\phi}^2(L^{i,q})^3\right] \qquad (2.36)$$

For $\dfrac{\dot{\phi}}{2} > V_n$

$$V_n^{i,q}\left|V_n^{i,q}\right| = \frac{1}{L}\int\limits_{-L/2}^{L/2}(V_n^{i,q} + \dot{\phi}r)^2\,dr = \frac{sign(V_n^{i,q})}{L^{i,q}}\left[\frac{2}{3}\frac{(V_n^{i,q})^3}{\dot{\phi}} + \frac{1}{2}V_n^{i,q}\dot{\phi}(L^{i,q})^2\right] \qquad (2.37)$$

Similarly, the velocity-squared term for the binormal component can be obtained using θ (angle around normal axis) instead of ϕ.

The formulas listed above are based on an in-line flow approach. An alternative approach is to apply the cross-flow assumption using vector calculation. In this approach, the tangential component remains the same while the normal and binormal components are changed as follows.

$$V_{cr}\cdot\left|V_{cr}\right| = (V_n\,\hat{n} + V_b\,\hat{b})\cdot\left|V_n + V_b\right|$$

$$= V_n\sqrt{V_n^2 + V_b^2}\,\hat{n} + V_b\sqrt{V_n^2 + V_b^2}\,\hat{b} \qquad (2.38)$$

thus

$$V_n\left|V_n\right| \approx V_n\sqrt{V_n^2 + V_b^2} \qquad \text{and} \qquad V_b\left|V_b\right| \approx V_b\sqrt{V_n^2 + V_b^2} \qquad (2.39)$$

Added mass: normal and binormal components

$$F_{An}^{i,q} = \frac{1}{4}\rho \cdot \pi \cdot D^2 \cdot L^{i,q} \cdot C_{mn} \cdot \dot{V}_n^{i,q} \tag{2.40}$$

$$F_{Ab}^{i,q} = \frac{1}{4}\rho \cdot \pi \cdot D^2 \cdot L^{i,q} \cdot C_{mb} \cdot \dot{V}_b^{i,q} \tag{2.41}$$

Because of the linear relationship between inertia force and acceleration, angular motion does not contribute to the averaged value of acceleration over each segment.

2.5.3. System Equations in Two Dimensions

A finite difference method is applied for the numerical solution of the derived partial differential equations of motion. Although there a number of different schemes one could choose, only representative system equations in 2-dimensions are given here. Both 3-point symmetric (central) and asymmetric (forward and backward) schemes for spatial derivatives are used for the computation and all schemes are compatible with variable grid size.

System equations including bending stiffness term in natural coordinates

For the first end node (forward difference),

$$m^1\left(\dot{V}_t^{1,q} - V_n^{1,q}\dot{\phi}^{1,q}\right) = F_t^{1,q} - W_o^1 \sin\phi^{1,q}$$

$$+ \frac{(\Delta s_1^2 + 2\Delta s_1\Delta s_2 + \Delta s_2^2)T^{2,q} - \Delta s_1^2 T^{3,q} - T^{1,q}(2\Delta s_1\Delta s_2 + \Delta s_2^2)}{\Delta s_1\Delta s_2(\Delta s_1 + \Delta s_2)}$$

$$+ S_n^{1,q}\frac{\Delta s_1^2(\phi^{2,q} - \phi^{3,q}) + 2\Delta s_1\Delta s_2(\phi^{2,q} - \phi^{1,q}) + \Delta s_2^2(\phi^{2,q} - \phi^{1,q})}{\Delta s_1\Delta s_2(\Delta s_1 + \Delta s_2)}$$

$$m^1\left(\dot{V}_n^{1,q} + V_t^{1,q}\dot{\phi}^{1,q}\right) = F_n^{1,q} - W_o^1\cos\phi^{1,q}$$

$$+ T^{1,q}\frac{\Delta s_1^2(\phi^{2,q} - \phi^{3,q}) + 2\Delta s_1\Delta s_2(\phi^{2,q} - \phi^{1,q}) + \Delta s_2^2(\phi^{2,q} - \phi^{1,q})}{\Delta s_1\Delta s_2(\Delta s_1 + \Delta s_2)}$$

$$+ \frac{\Delta s_1^2(S_n^{2,q} - S_n^{3,q}) + 2\Delta s_1\Delta s_2(S_n^{2,q} - S_n^{1,q}) + \Delta s_2^2(S_n^{2,q} - S_n^{1,q})}{\Delta s_1\Delta s_2(\Delta s_1 + \Delta s_2)}$$

$$S_n^{1,q} = -EI\frac{2[\Delta s_1(\phi^{3,q} - \phi^{2,q}) - \Delta s_2(\phi^{2,q} - \phi^{1,q})]}{\Delta s_1\Delta s_2(\Delta s_1 + \Delta s_2)} \qquad \textbf{(2.42)}$$

For an ith internal node (central difference),

$$m^i\left(\dot{V}_t^{i,q} - V_n^{i,q}\dot{\phi}^{i,q}\right) = F_t^{i,q} - W_o^i\sin\phi^{i,q}$$

$$+ \frac{(\Delta s_i^2 - \Delta s_{i-1}^2)T^{i,q} + \Delta s_{i-1}^2 T^{i+1,q} - T^{i-1,q}\Delta s_i^2}{\Delta s_i\Delta s_{i-1}(\Delta s_i + \Delta s_{i-1})}$$

$$- S_n^{i,q}\frac{\Delta s_{i-1}^2(\phi^{i+1,q} - \phi^{i,q}) + \Delta s_i^2(\phi^{i,q} - \phi^{i-1,q})}{\Delta s_i\Delta s_{i-1}(\Delta s_i + \Delta s_{i-1})}$$

$$m^i\left(\dot{V}_n^{i,q} + V_t^{i,q}\dot{\phi}^{i,q}\right) = F_n^{i,q} - W_o^i\cos\phi^{i,q}$$

$$+ T^{i,q}\frac{\Delta s_{i-1}^2(\phi^{i+1,q} - \phi^{i,q}) + \Delta s_i^2(\phi^{i,q} - \phi^{i-1,q})}{\Delta s_i\Delta s_{i-1}(\Delta s_i + \Delta s_{i-1})}$$

$$+ \frac{\Delta s_{i-1}^2(S_n^{i+1} - S_n^i) + \Delta s_i^2(S_n^i - S_n^{i-1})}{\Delta s_i\Delta s_{i-1}(\Delta s_i + \Delta s_{i-1})}$$

$$S_n^{i,q} = -EI\frac{2[\Delta s_{i-1}(\phi^{i+1,q} - \phi^{i,q}) - \Delta s_i(\phi^{i,q} - \phi^{i-1,q})]}{\Delta s_i\Delta s_{i-1}(\Delta s_i + \Delta s_{i-1})} \qquad \textbf{(2.43)}$$

where Δs_i is the length of the ith segment and superscripts i and q denote i^{th} node and q^{th} time step, respectively.

For the last end node, finite difference equations can be obtained in the same manner as for the first node by replacing the spatial derivative term with a backward difference scheme.

System equations in global coordinates

Unlike the previous equations, bending stiffness is not included here because the terms with bending stiffness in the original equations involve fourth-order spatial derivatives of position vectors and so a fine grid size is required to obtain a sufficient degree of accuracy. Thus the system equations expressed in global coordinates below are only applicable to mooring line components whose bending stiffness is negligible, such as chain and thin wire.

For the first end node,

$$m^1 \left[\ddot{x}^{1,q} - \dot{y}^{1,q} \, \dot{\phi}^{1,q} \right] = F_t^{1,q} \cos\phi^{1,q} - F_n^{1,q} \sin\phi^{1,q}$$

$$+ \left[\frac{dT}{ds} \right]^{1,q} \left[\frac{dx}{ds} \right]^{1,q} + T^{1,q} \left[\frac{d^2 x}{ds^2} \right]^{1,q}$$

$$\text{(2.44)}$$

$$m^1 \left[\ddot{y}^{1,q} + \dot{x}^{1,q} \, \dot{\phi}^{1,q} \right] = - W_0^1 + F_t^{1,q} \sin\phi^{1,q} + F_n^{1,q} \cos\phi^{1,q}$$

$$+ \left[\frac{dT}{ds} \right]^{1,q} \left[\frac{dy}{ds} \right]^{1,q} + T^{1,q} \left[\frac{d^2 y}{ds^2} \right]^{1,q}$$

where

$$\left[\frac{d(\ )}{ds} \right]^{1,q} = \frac{\Delta s_1^2 \left[(\ )^{2,q} - (\ )^{3,q} \right] + 2 \Delta s_1 \Delta s_2 \left[(\ )^{2,q} - (\ )^{1,q} \right] + \Delta s_2^2 \left[(\ )^{2,q} - (\ )^{1,q} \right]}{\Delta s_1 \Delta s_2 (\Delta s_1 + \Delta s_2)}$$

$$\left[\frac{d^2(\ )}{ds^2}\right]^{1,q} = 2\,\frac{\Delta s_1\,[(\ )^{3,q} - (\ )^{2,q}] - \Delta s_2\,[(\ )^{2,q} - (\ )^{1,q}]}{\Delta s_1\,\Delta s_2\,(\Delta s_1 + \Delta s_2)}.$$

For an ith internal node,

$$m^i\left[\ddot{x}^{i,q} - \dot{y}^{i,q}\dot{\phi}^{i,q}\right] = -F_t^{i,q}\cos\phi^{i,q} + F_n^{i,q}\sin\phi^{i,q}$$

$$+ \left[\frac{dT}{ds}\right]^{i,q}\left[\frac{dx}{ds}\right]^{i,q} + T^{i,q}\left[\frac{d^2x}{ds^2}\right]^{i,q}$$

(2.45)

$$m^i\left[\ddot{y}^{i,q} + \dot{x}^{i,q}\dot{\phi}^{i,q}\right] = -W_0^i + F_t^{i,q}\sin\phi^{i,q} + F_n^{i,q}\cos\phi^{i,q}$$

$$+ \left[\frac{dT}{ds}\right]^{i,q}\left[\frac{dy}{ds}\right]^{i,q} + T^{i,q}\left[\frac{d^2y}{ds^2}\right]^{i,q}$$

where

$$\left[\frac{d(\ )}{ds}\right]^{i,q} = \frac{\Delta s_{i-1}^2\,[(\ )^{i+1,q} - (\ )^{i,q}] + \Delta s_i^2\,[(\ )^{i,q} - (\ )^{i-1,q}]}{\Delta s_i\,\Delta s_{i-1}\,(\Delta s_i + \Delta s_{i-1})}$$

$$\left[\frac{d^2(\ )}{ds^2}\right]^{i,q} = \frac{\Delta s_{i-1}\,[(\ )^{i+1,q} - (\ )^{i,q}] - \Delta s_i\,[(\ )^{i,q} - (\ )^{i-1,q}]}{\Delta s_i\,\Delta s_{i-1}\,(\Delta s_i + \Delta s_{i-1})}.$$

Similarly, the equations for the last node can be derived with a backward difference scheme.

Based on the above equations, applying the boundary condition of known (i.e. measured) top (or bottom) tension and the known values of tangential hydrodynamic force coefficients yields a couple of closed systems with two unknown variables of tension and normal hydrodynamic force for each node point.

2.6. Estimation of Force Transfer Coefficients

Generally, for purposes of design, one is interested in modeling the time-dependent forces on floating systems exposed to realistic ocean environments. In the context of modeling the hydrodynamic forces on mooring systems using Morison's equation, this would require knowledge of flow-dependent and time-dependent force coefficients. Due to the complexities of the fluid-structure interaction experienced by mooring lines in real environments, it is not possible to catalog instantaneous (time-dependent) values of the Morison force coefficients for all the relevant flow conditions. However, time- or frequency (or harmonic)-averaged values of the hydrodynamic coefficients can be regarded as practical alternatives to instantaneous values to appropriately represent the characteristics of slender body hydrodynamics. The dependence of the time- or frequency-averaged coefficients on the flow conditions (as characterized by the Re and KC numbers) may still be retained, and is in part the subject of this dissertation.

Given the measured or indirectly derived total hydrodynamic force and line kinematics from experiments, the force transfer coefficients can be estimated in several ways. Either the least square minimization method or the Fourier analysis method may be applied to obtain both drag and added mass coefficients. Note that neither method is applicable to the over-damped free oscillation case since no harmonic motion exists. For this reason, the force transfer coefficients from free oscillation tests are obtained by direct calculation of the dynamic equation, as will be explained later in detail.

2.6.1. Fourier Analysis

Since the motion of a mooring line is composed of multiple harmonic modes, the motion-induced hydrodynamic force must have different transfer coefficients for each harmonic. Using the Fourier transform, the time series of the total in-line force and its drag and added mass force components can be further decomposed into various frequency-dependent components. Splitting the Fourier-transformed data into real and imaginary parts yields, for each harmonic, two equations with two unknowns, C_D and C_A. The conventional Morison equation and its Fourier series representation are

$$F_N = F_D + F_A = -\frac{1}{2}\rho D C_D V|V| - \frac{1}{4}\pi\rho D^2 C_A A \tag{2.46}$$

and

$$\sum_{k=1}^{N}\left[\mathrm{Re}[F_N^f(k)]\cos(\omega_k t)\right] = -\frac{1}{2}\rho D \sum_{k=1}^{N} C_D^k \left[\mathrm{Re}[V_{NS}^f(k)]\cos(\omega_k t)\right]$$

$$-\frac{1}{4}\pi\rho D^2 \sum_{k=1}^{N} C_A^k \left[\mathrm{Re}[A_N^f(k)]\cos(\omega_k t)\right]$$

$$\tag{2.47}$$

$$\sum_{k=1}^{N}\left[\mathrm{Im}[F_N^f(k)]\sin(\omega_k t)\right] = -\frac{1}{2}\rho D \sum_{k=1}^{N} C_D^k \left[\mathrm{Im}[V_{NS}^f(k)]\sin(\omega_k t)\right]$$

$$-\frac{1}{4}\pi\rho D^2 \sum_{k=1}^{N} C_A^k \left[\mathrm{Im}[A_N^f(k)]\sin(\omega_k t)\right]$$

where F_N^f : in-line force for each harmonic

V_{NS}^f : velocity squared term with sign for each harmonic

A_N^f : acceleration term for each harmonic

ω : angular frequency.

The averaged force coefficients for each harmonic can be readily obtained by multiplying both sides of equation (2.47) with $\cos(\omega_k t)$ for the real part and $\sin(\omega_k t)$ for the imaginary part, respectively, and integrating over the cycle of each frequency.

2.6.2. Least Square Minimization

The estimation of the averaged force coefficients for the total time history is achieved by minimizing the least square difference (E^2), defined as follows:

$$E^2 = \sum [S_M - S_{FF}]^2 \tag{2.48}$$

where S_M is the amplitude spectrum of the calculated force by solving the chain-cable dynamic equations and S_{FF} is the amplitude spectrum of force expressed by Morison's equation, that is,

$$S_{FF} = \frac{1}{2}\rho D C_D S_{(V|V|)(V|V|)} + \frac{1}{4}\pi \rho D^2 C_A S_{AA} \tag{2.49}$$

Differentiating E^2 with respect to C_D and C_A, respectively, and setting the two resulting equations equal to zero yields the time-averaged force coefficients for each mooring line segment,

$$\frac{dE^2}{dC_D} = \frac{1}{2}\rho D C_D \sum S_{(V|V|)(V|V|)}^2 + \frac{1}{4}\pi \rho D^2 C_A \sum S_{AA} + \sum S_M S_{(V|V|)(V|V|)} = 0$$

$$\tag{2.50}$$

$$\frac{dE^2}{dC_A} = \frac{1}{2}\rho D C_D \sum S_{(V|V|)(V|V|)} S_{AA} + \frac{1}{4}\pi\rho D^2 C_A \sum S_{AA}^2 + \sum S_M S_{AA} = 0$$

Alternatively, the power spectrum of the in-line force can be used to obtain the time-averaged value of the coefficients by applying the Fourier transform to the expression for the covariance of the in-line force. As mentioned in section 1.2.2.2, Borgman (1965) derived the power spectrum of wave force on bodies for a Gaussian wave process, in which some assumptions on the variables (force, velocity, acceleration) were made. In the present study, however, one might employ the following form of covariance of Morison's type force simplified by the assumption of zero-mean acceleration:

$$R_{FF} = C_1^2 R_{(V|V|)(V|V|)} + C_2^2 R_{\dot{V}\dot{V}} \qquad\qquad (2.51)$$

Using the Wiener-Khintchine relationship,

$$S_{FF} = \frac{1}{2\pi} \int_{-\infty}^{\infty} R_{FF}(\tau)\, e^{-i\omega\tau}\, d\tau \qquad\qquad (2.52)$$

and substituting Eq. (2.51), Eq. (2.52) becomes

$$\mathcal{F}\{R_{FF}\} = S_{FF} = C_1^2 S_{(V|V|)(V|V|)} + C_2^2 S_{\dot{V}\dot{V}} \qquad\qquad (2.53)$$

where $\quad C_1 = \dfrac{1}{2}\rho D C_D$

$\qquad C_2 = \dfrac{1}{4}\pi\rho D^2 C_A$

$\qquad \mathcal{F}\{\} \quad : \quad$ denotes the Fourier transform.

Likewise, applying the least square minimization to equation (2.53) can yield time-averaged hydrodynamic coefficients. Since the values of the coefficients estimated through this equation, especially the added mass coefficient, were observed to be much larger than those from the amplitude spectrum which indicates the results might be

distorted by the assumption associated with the acceleration, only the amplitude spectrum, equation (2.49), will be employed for the estimation of time-averaged coefficients in this study.

2.7. Velocity and Time Scales

The Reynolds number (Re) and Keulegan-Carpenter number (KC) may be specified in terms of characteristic velocity and time scales. When correlating frequency- or time-averaged force coefficients with Re and KC, it is important to use consistent velocity and time scales. For frequency-averaged coefficients, the velocity amplitude and the period (reciprocal of frequency) for each harmonic can be employed. The time-averaged coefficients can be well correlated with the root mean square (RMS) velocity and the average zero-upcrossing period, which is the average time interval between successive upcrossings of the mean position. For a zero-mean Gaussian velocity process, the zero-upcrossing period may be calculated as:

$$T_Z = 2\pi \sqrt{\frac{m_0}{m_2}} = 2\pi \frac{\sigma_V}{\sigma_{\dot{V}}} \tag{2.54}$$

where σ_V :   standard deviation of velocity

$\sigma_{\dot{V}}$:   standard deviation of acceleration

$m_n = \int_0^\infty \omega^n S(\omega) \, d\omega$:   spectral moments.

Alternatively, if the velocity process can be further assumed to be narrow banded, one might use the characteristic RMS velocity defined as $\sqrt{2} \cdot \sigma_V$.

2.8. Bending Stiffness

The effect of bending stiffness due to curvature of a cable or wire rope segment should be considered when designing a mooring system. In deep water the effect of bending stiffness is generally neglected, but in shallow water and laboratory situations, where the radius of curvature may not be that small, the effect of bending stiffness in generating internal shear forces and moments may be significant. The shear force is oriented with the normal hydrodynamic force whose magnitude is an important factor in design because of its role in generating system damping for the floating structure. Therefore, without considering the effect of bending, the evaluation of damping from the mooring system may not be accurate.

The bending stiffness of wire rope used in the laboratory experiments described in Chapter III is not available from the manufacturer and instruments for direct measurement of bending stiffness are not available to us. Consequently the following method was devised to measure the bending stiffness of the wire rope segments used in the experiments. Each wire segment was hung as shown in Figure 2.4 with both ends fixed. A tri-axial load cell was placed at one end to measure the tension and shear force. The position of each optical target placed on the wire was measured through optical tracking.
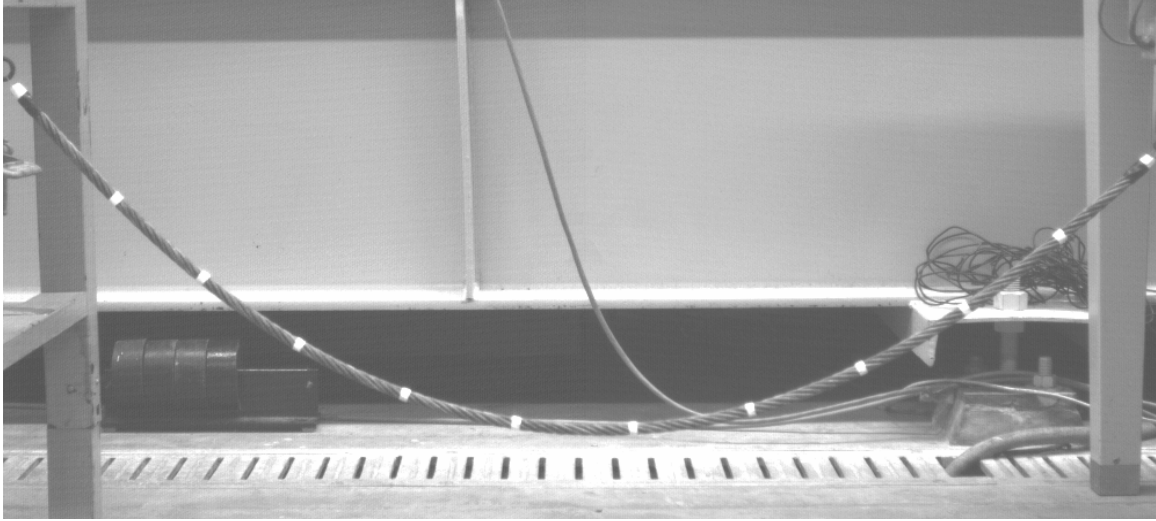
Figure 2.4 Experimental configuration of wire for measurement of bending stiffness

With these data, solving the static equilibrium yields the shear force at each discretized node point (optical target location).   The static equilibrium equation in 2-D can be derived from Eq. (2.20) by setting the inertia and hydrodynamic forces equal to zero:

$$\frac{\partial T_t}{\partial s} - S_n \frac{\partial \phi}{\partial s} - W_0 \sin \phi = 0$$

$$T_t \frac{\partial \phi}{\partial s} + \frac{\partial S_n}{\partial s} - W_0 \cos \phi = 0$$

$$\text{(2.55)}$$

$$S_n = - EI \frac{\partial^2 \phi}{\partial s^2} \qquad \text{(2.56)}$$

From Eq. (2.54), the bending stiffness (EI) can be obtained for each segment.   If a variation of values over all sections is observed, an average or median value may be

taken as representative if the single wire is known to have uniform material properties.

Eq. (2.56) is exactly the same as the shear-curvature relation in fundamental beam-deflection theory, which is founded on the assumption that the deflection angle (ϕ) is small enough for the approximations $\tan\phi \cong \phi$ and $\cos\phi \cong 1$ to be valid. However, since wire rope is more flexible and in most applications experiences larger curvature than beams do, the alternative relation between shear force and curvature without the small angle assumption may be required to achieve sufficient accuracy.
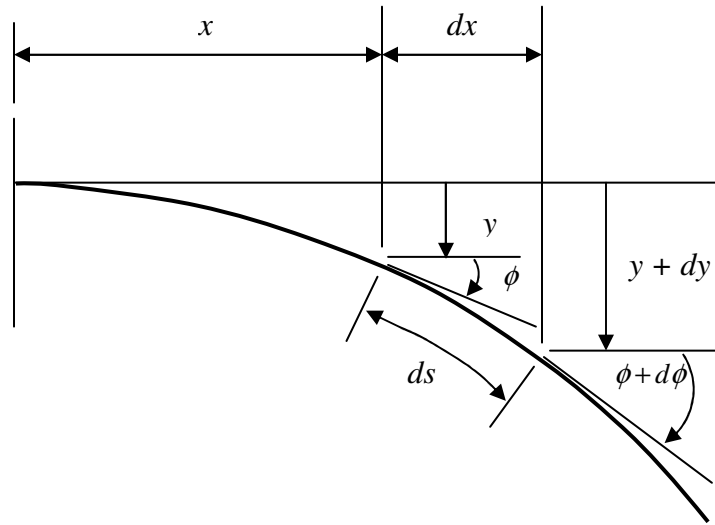
Figure 2.5   Deflection curve

The new equation is derived from the classic relation

$$S_n = -EI \frac{\partial^3 y}{\partial x^3} \tag{2.57}$$

where y :   vertical deflection

         x :   horizontal coordinate.

The third order spatial derivative of deflection can be obtained by differentiating the slope of the deflection curve twice with respect to x and using following relations (refer to Figure 2.5),

$$\frac{dx}{ds} = \cos\phi, \qquad \frac{dy}{dx} = \tan\phi \qquad \text{and} \qquad \frac{\partial^2 y}{\partial x^2} = \frac{\partial}{\partial x}\tan\phi = \frac{1}{\cos^2\phi}\frac{\partial\phi}{\partial x} \qquad \textbf{(2.58)}$$

The final equation for the shear force is expressed as:

$$S_n = -EI \frac{\partial}{\partial x}\left(\frac{\partial^2 y}{\partial x^2}\right) = -\frac{EI}{\cos^4\phi}\left[3\tan\phi\left(\frac{\partial\phi}{\partial s}\right)^2 + \frac{\partial^2\phi}{\partial s^2}\right] \qquad \textbf{(2.59)}$$

Results from both equations (2.56) and (2.59) will be compared and tested for how they affect the inferred hydrodynamic force coefficients (see section 4.2).

CHAPTER III

EXPERIMENTAL DESIGN AND DATA PROCESSING

3.1. Experimental Design

The availability of optical tracking techniques using high-speed video provides an opportunity for exploring the feasibility of deducing Morison drag and inertia coefficients from measured trajectories of chain and cable elements undergoing controlled free or forced oscillations in calm water. A Similar type of 3-D motion tracking of oscillating chain in air was conducted by C.T. Howell (1992) for the verification of analytical and numerical models of resonant response.   Since there is no available technique for direct measurement of the hydrodynamic force on an oscillating slender body such as chain and wire rope, an alternative, indirect method is proposed where the fluid force is obtained from the solution of the slender body dynamic equations of motion using the measured line displacement and end-force.   In principle a free oscillation test may be used to estimate instantaneous values of the drag coefficient, whereas a forced oscillation test may be analyzed to derive Fourier- and time-averaged values of both the drag and added mass coefficients.

Small scale oscillation experiments were performed to simply test the approach and work out the majority of problems which can potentially occur in a large scale test. Given success with the small scale experiments, both free and forced oscillation tests at large scale were conducted in the OTRC wave basin with the benefit of the knowledge and confidence gained in the foregoing experiences.

3.1.1. Small Scale Experiments (Free Oscillation Tests)

The objective of this part is to set-up an experiment to measure the motion of chain undergoing free oscillation in calm water. Experiments took place in a small 2-D wave flume whose sides are made of glass, which enables direct measurement of line kinematics by optical tracking (Figure 3.1). The interior width of the flume is 0.914 m and the maximum water depth is 1.21 m.

Three different sizes of twisted link chains were tested in order to investigate a wide range of Re and KC number. Chains of about 0.7 m length were tested. Detailed characteristics of each chain are given in Table 3.1. The equivalent diameter, D_{eq}, is calculated using the measured submerged unit weight of the chain, W_{sub} according to

$$D_{eq} = \sqrt{4(W - W_{sub})/(\pi \rho L)} \tag{3.1}$$

where W and L are the unit weight and length of the chain, and ρ is the water density.

Table 3.1   Characteristics of small scale chains tested

| Chain Characteristic	Big Chain	Medium Chain	Small Chain
Weight per Unit Length [kg/m]	0.1257	0.0766	0.0454
Submerged Unit Weight [kg/m]	0.1073	0.0632	0.0364
Equivalent Diameter [m]	0.0048	0.0041	0.0034
Length [m]	0.703	0.706	0.690
Marker Spacing [m]	0.0566	0.049	0.0518

The top of the chain was pinned just below the water level and thereby confined to rotational motion. Initially the other end of the chain was held in a pliers-type release device.   The pliers are opened electronically through a controller.   Upon release of the bottom of the chain, the motion of the chain is tracked by the camera until the chain comes to rest in the vertical position (Figure 3.2).   An example trajectory from a free oscillation test is given in Figure 3.3.
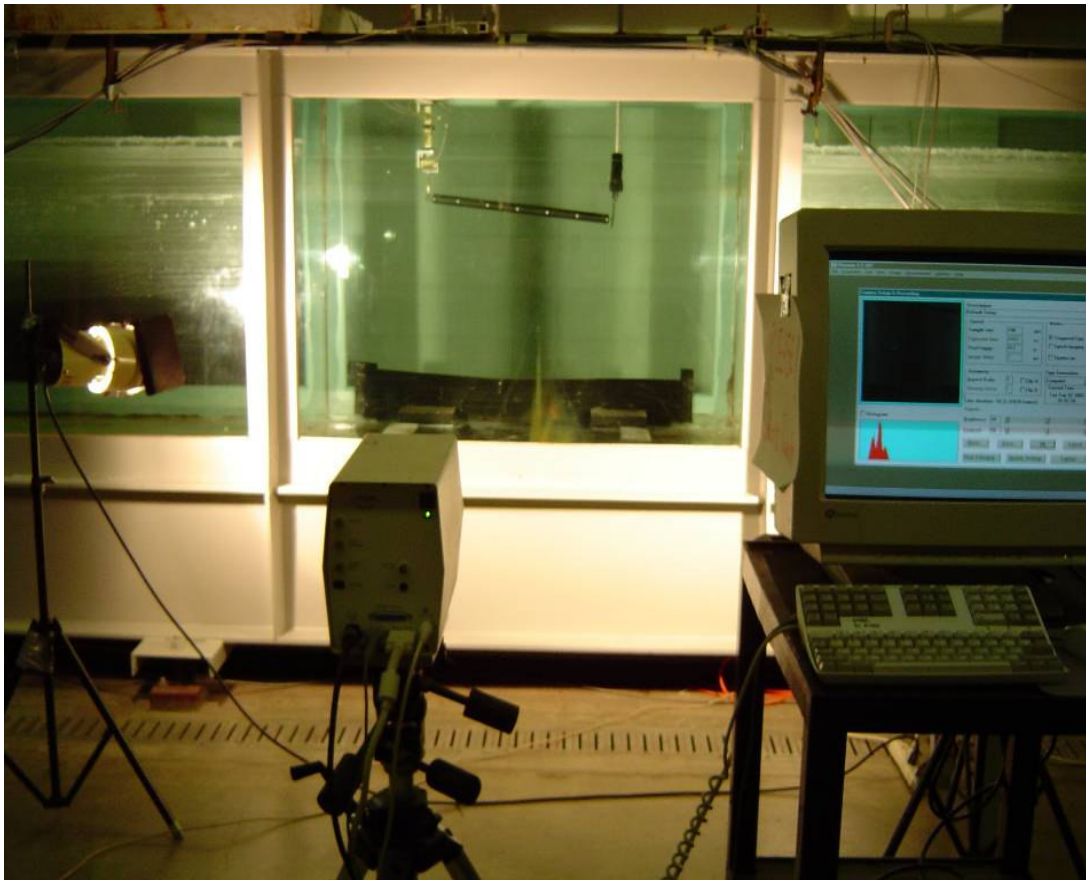
Figure 3.1   Experimental set-up of small scale test
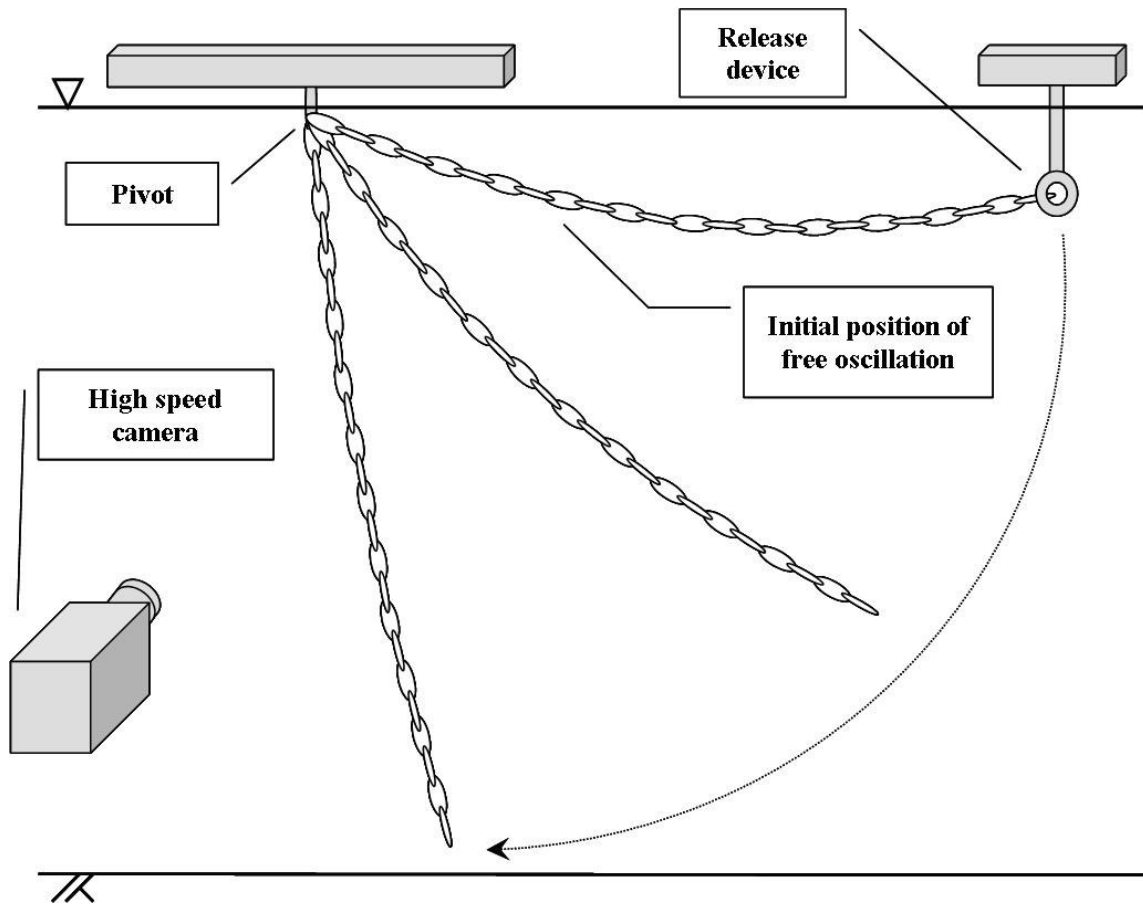
**Figure 3.2   Small scale free oscillation test**
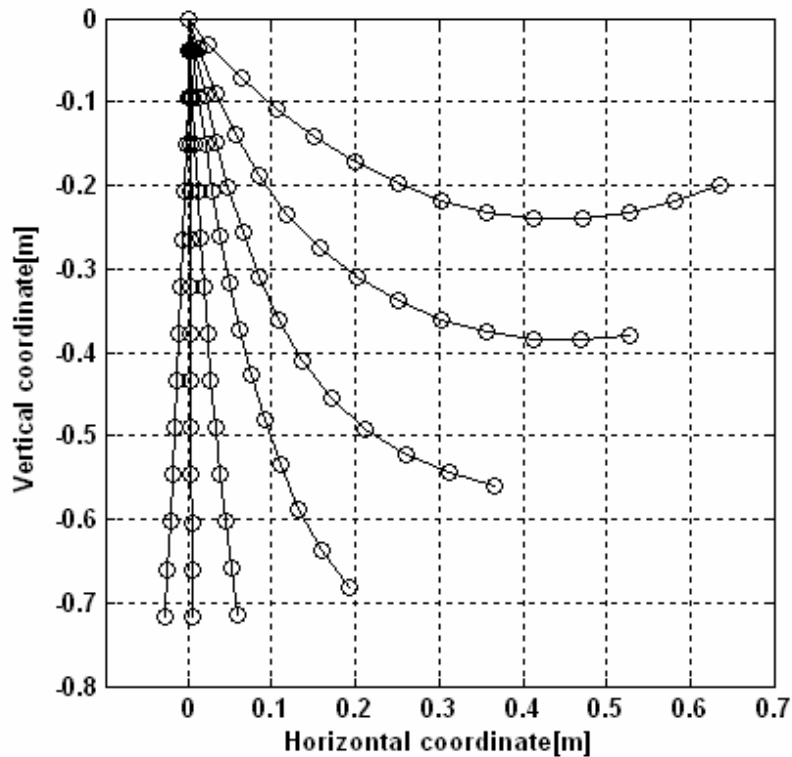
Figure 3.3   Sample trajectory from a free oscillation test

For optical tracking of the chain, a digital high-speed video camera (early version Phantom V-series camera, manufactured by Vision Research Inc.) which can record up to 1000 frames per second was employed.   The camera produces black & white images at a resolution of 512 pixels by 512 pixels.   Markers consisting of little strips of white tape were placed with uniform spacing on the test chains.   In order to easily analyze the video, one has to maximize the contrast between the markers and the background, so all possible areas appearing bright should appropriately be blocked out.   A pair of high intensity lights was placed in front of the flume window to illuminate the markers on the chain.

3.1.2. Large Scale Experiments

Large scale experiments were conducted in the OTRC 3D wave basin. The wave basin was designed for hydrodynamic model testing of moored, deepwater offshore structures. The basin is 150 ft long, 100 ft wide and 19 ft deep. Observation windows are located on each side of the basin and beneath the wavemaker, which enables optical tracking of submerged bodies (Figure 3.4). The large scale experiments were designed to utilize the full depth of the basin. Accordingly, the field of view (FOV) was set at 5 m x 5 m, much larger than the 0.78 m x 0.78 m FOV used in the small scale tests in the wave flume.

In order to minimize the resolution error from optical tracking, a CCD camera (Phantom v5.1 camera, manufactured by Vision Research Inc.) with a resolution of 1024 pixels by 1024 pixels and a frame rate of up to 1000 Hz was employed, offering twice the accuracy relative to the small scale experiments. Since high speed cameras have very poor light sensitivity compared with regular digital cameras, pictures must be taken with intense lighting. Accordingly, six underwater lights with unit brightness of over 9000 lumens were placed around the tracking object close enough to create the best illumination without creating excessive glare (Figure 3.5).
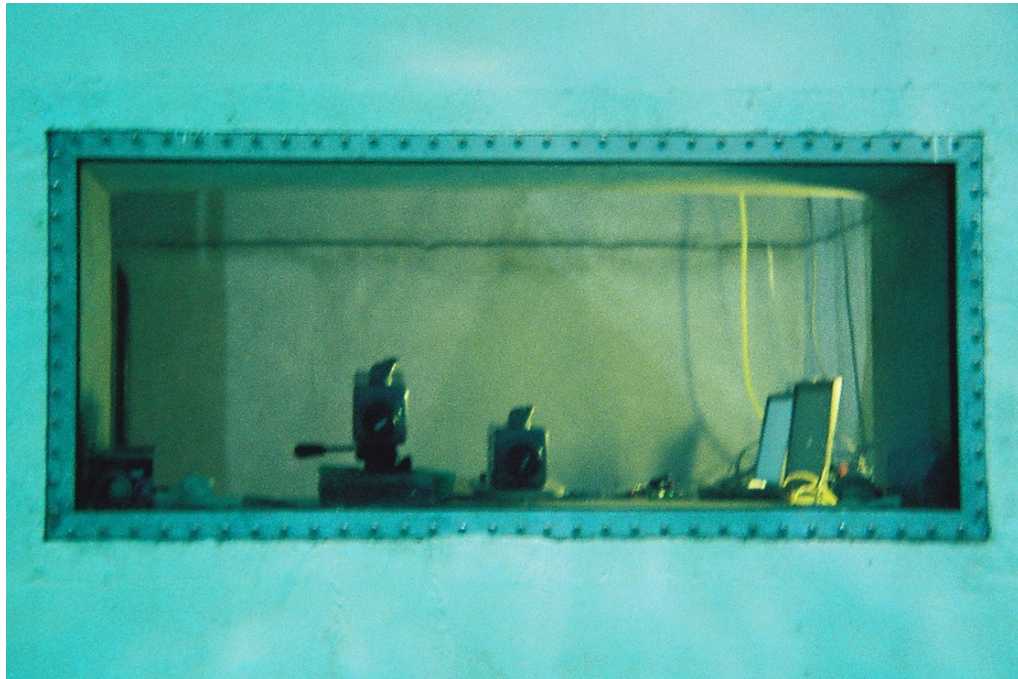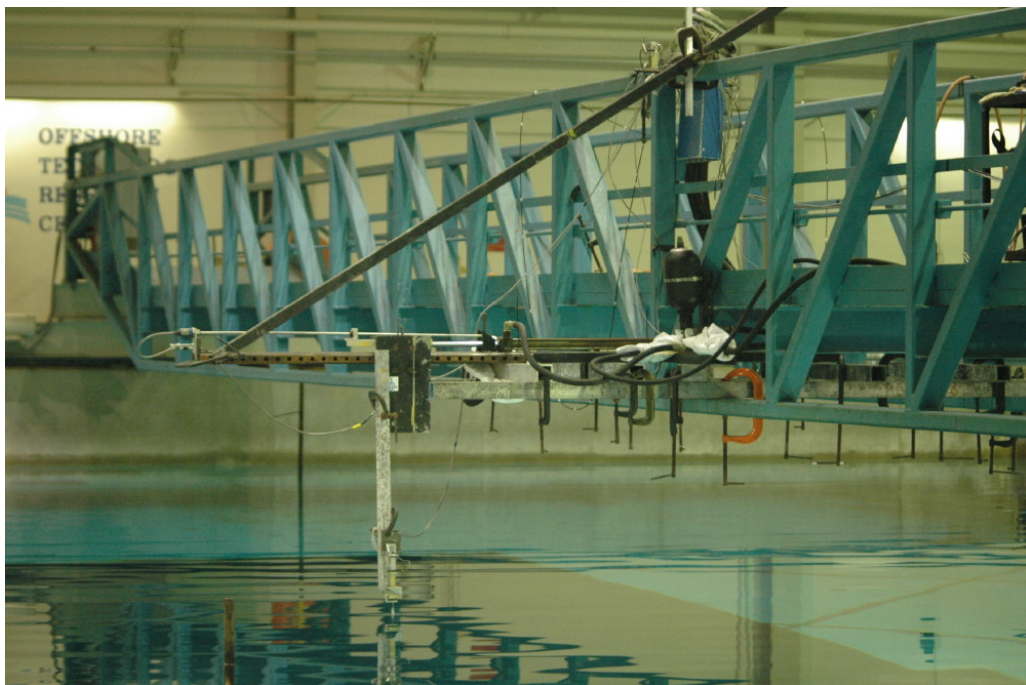
Figure 3.4   Optical tracking camera installed on the side window of OTRC basin
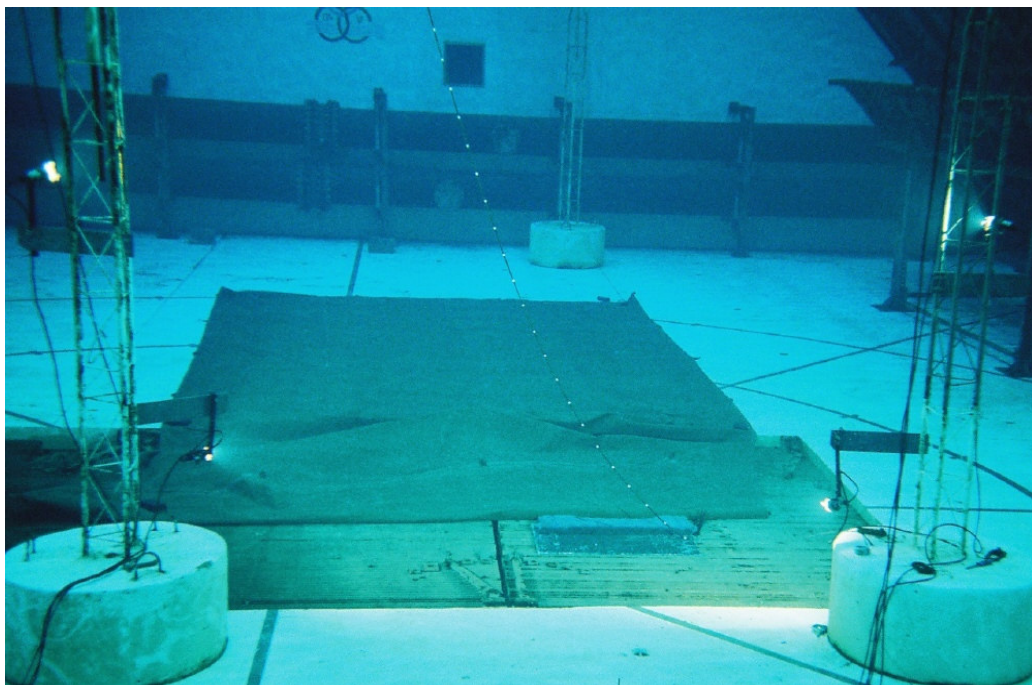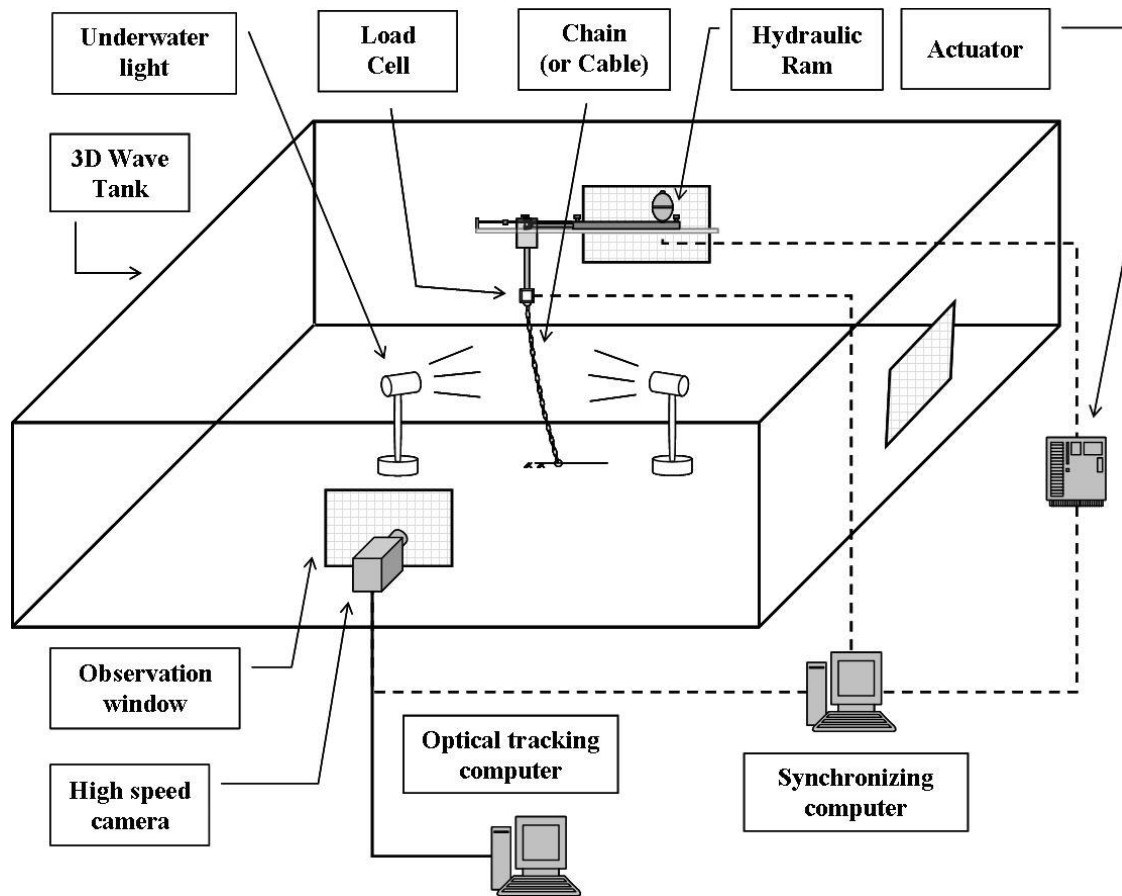

Figure 3.5   Underwater lighting set-up
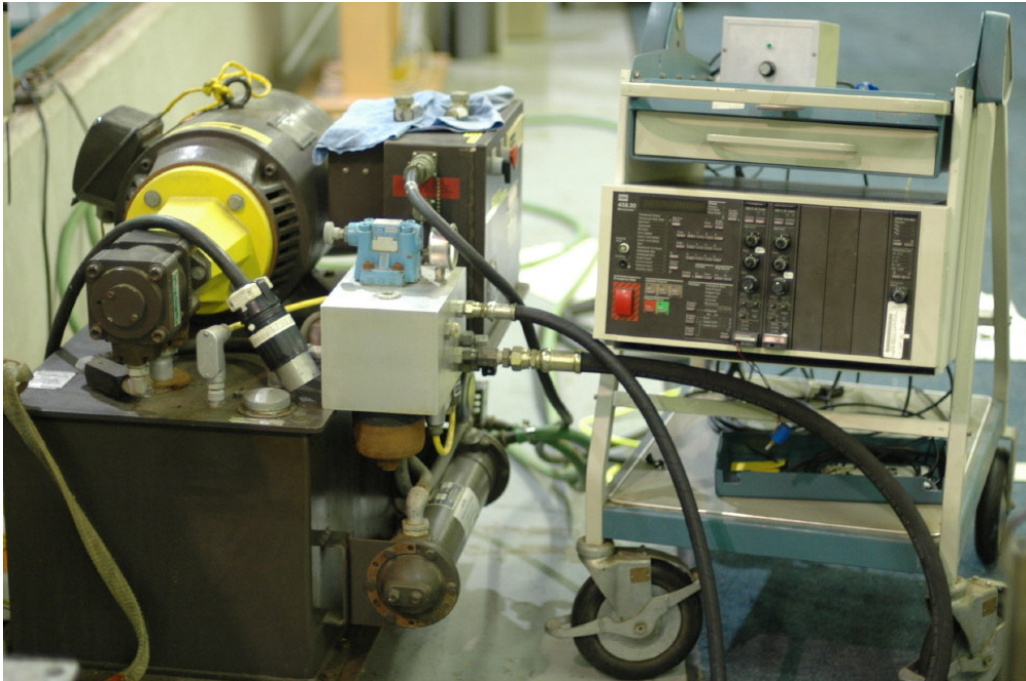
Figure 3.6   Power supply and MTS controller for hydraulic ram

Figure 3.7   Hydraulic ram installed on the bridge for the forced oscillation test

**Figure 3.8   Diagram of large scale test setup**

In addition to optical tracking measurements, the top tension in the mooring line was measured using a tri-axial load cell composed of three stacked single-axis load cells oriented to measure the three directional X, Y, and Z force components.   Loads cells of two different capacities are combined for cases where one of the directional force components is much smaller than the others in order to increase the accuracy of the data. A hydraulic ram actuated by an MTS Systems Corp. series 458 analog servo-controller with MLDT (magnetostrictive linear displacement transducer) position feedback is used

to sinusoidally oscillate the top of the line at single or multiple frequencies (Figure 3.6 and Figure 3.7). Synchronization of all of the measurement channels is simply done by transmitting a signal to each device identified above, so that all devices can be automatically triggered at the same time. The set-up in the OTRC wave tank is roughly displayed in Figure 3.8.

By performing both free and forced oscillation tests of flexible cable and chain segments, one can derive detailed insight into the behavior of the fluid-structure interaction, which may demonstrate the existence of different hydrodynamic characteristics for different ranges of KC and Re. To obtain a broad range of Re and KC, three different sizes of chain and cable were tested for various forced harmonic motions which may be either single frequency oscillations or combined low+high frequency oscillations. For the combined frequency motion, a typical wave frequency was superposed upon a frequency characteristic of slow drift surge motion in a typical 1:50 model scale situation. Table 3.2 summarizes the frequencies tested, corresponding to periods of 1.5, 3, 5, 10 and 15 seconds.

Table 3.2 Frequencies of forced oscillations

	Low Frequency			Low-High Combined Frequency	
Frequency [rad/s]	$2\pi/5$	$2\pi/10$	$2\pi/15$	$2\pi/15 + 2\pi/1.5$	$2\pi/15 + 2\pi/3$
Amplitude[m]	0.22	0.35	0.35	0.315 + 0.039	0.28 + 0.07
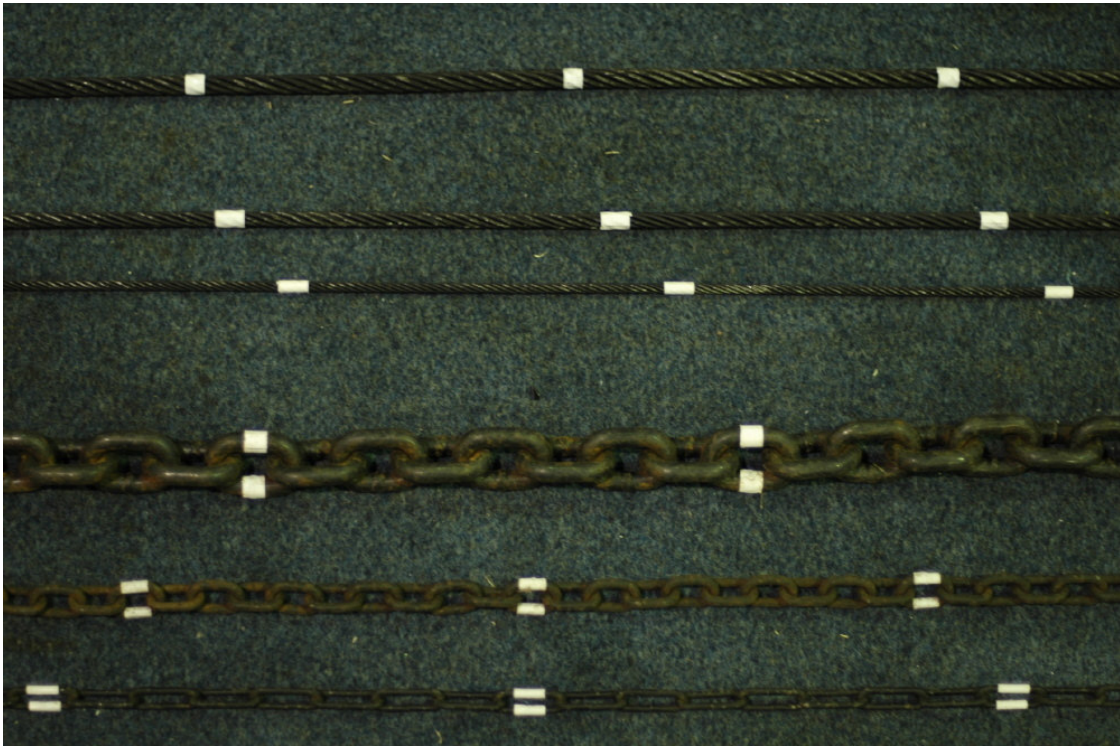
Figure 3.9   Chains and wires used in large scale test

Additionally, experiments with a combination mooring of chain-wire-chain were implemented to acquire data from a more realistic mooring line configuration used for offshore structures.   The length ratio of the chain-wire-chain combination was approximately 15%-70%-15% of the total line length.

Free oscillation tests of wire rope turned out to be impractical because of the significant influence of bending stiffness of the cable for the line lengths that could be tested.   The motion of free falling wire in fluids is substantially affected by material characteristics such as bending stiffness, torsional stiffness, etc.

The properties of all mooring lines tested in the large scale experiments are listed in

Table 3.3 and illustrated in Figure 3.9.

**Table 3.3   Characteristics of all mooring lines tested**

Material	Characteristics		Big	Medium	Small
Chain	Length [m]	Free oscillation	4.611594	4.757369	4.601306
		Suspended	6.047808	6.152369	6.049306
		Semi-taut	7.06707	6.956369	6.975306
	Marker Spacing [m]		0.25	0.197	0.24
	Unit Weight [kg/m]		2.306755	0.46576	0.189812
	Submerged Unit Weight [kg/m]		2.007127	0.402685	0.163092
	Equivalent Diameter [m]		0.019542	0.008966	0.005836
Wire	Length [m]	Semi-taut	7.0075	7.004	6.99875
	Marker Spacing [m]		0.20	0.20	0.20
	Unit Weight [kg/m]		0.342205	0.239006	0.086301
	Submerged Unit Weight [kg/m]		0.276535	0.192842	0.06831
	Equivalent Diameter [m]		0.009149	0.007671	0.004789
Chain - Wire - Chain	Total Length [m]		7.047594	7.059369	7.013306
	Cable Length [m]		5.005	5.007	5.004
	Chain Length for Each End [m]		0.986297	1.004184	0.981153
	Marker Spacing in chain[m]		0.24	0.197	0.24
	Marker Spacing in wire[m]		0.20	0.20	0.20
	Equiv. Diameter of Cable [m]		0.009149	0.007671	0.004789
	Equiv. Diameter of Chain [m]		0.019542	0.008966	0.005836

Two distinctive configurations of mooring line systems were employed for the forced oscillation tests. A semi-taut catenary configuration was tested to investigate the damping contribution of the sag bend section. A suspended catenary configuration was tested to investigate what effect on the hydrodynamic behavior of a mooring line can be produced by interaction with the (assumed rigid) seafloor. Therefore the semi-taut catenary mooring line was designed to have its bottom part contacting the floor of the basin while the suspended catenary mooring was designed to be free of such interaction (Figure 3.10 and Figure 3.11). Laboratory configurations and sample trajectories of both moorings are shown in Figure 3.12 and Figure 3.13, respectively.
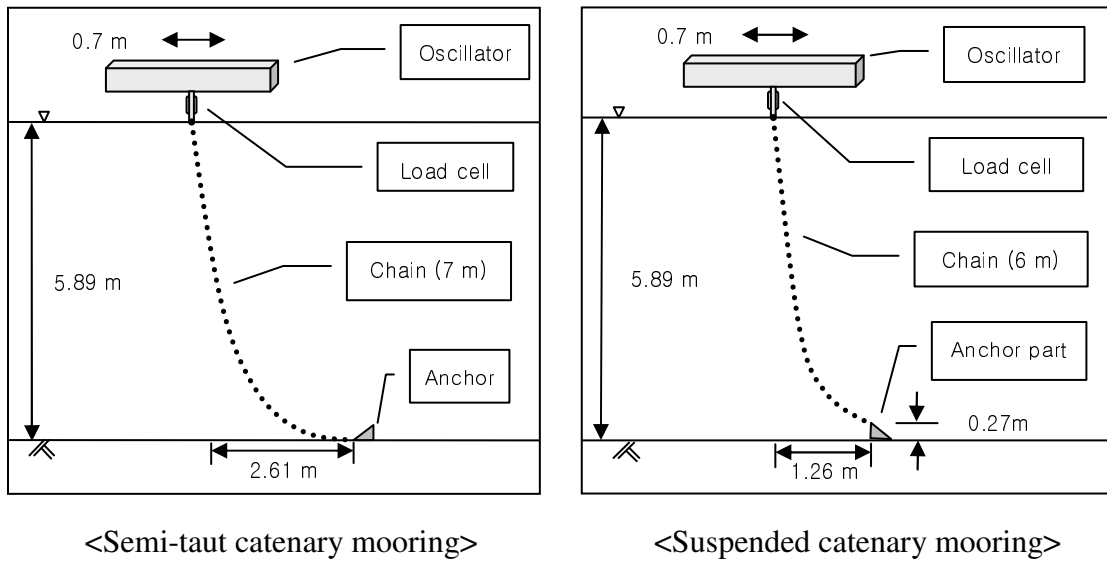
Table 3.4 lists the lowest natural frequency of vibration for each mooring configuration, as calculated using OrcaFlex, and shows that the modal natural periods for all tests were less than 3.15 seconds. With reference to the forcing frequencies provided in Table 3.2, it appears that only in the combined low+high frequency tests where the period of the high frequency oscillations was 1.5 sec is there a possibility for direct excitation of resonant modes in the line. Although direct (linear) excitation of resonant line motions was generally avoided, there is a possibility that resonant vibrations were excited by nonlinear forcing mechanisms associated with the fluid-structure interaction.
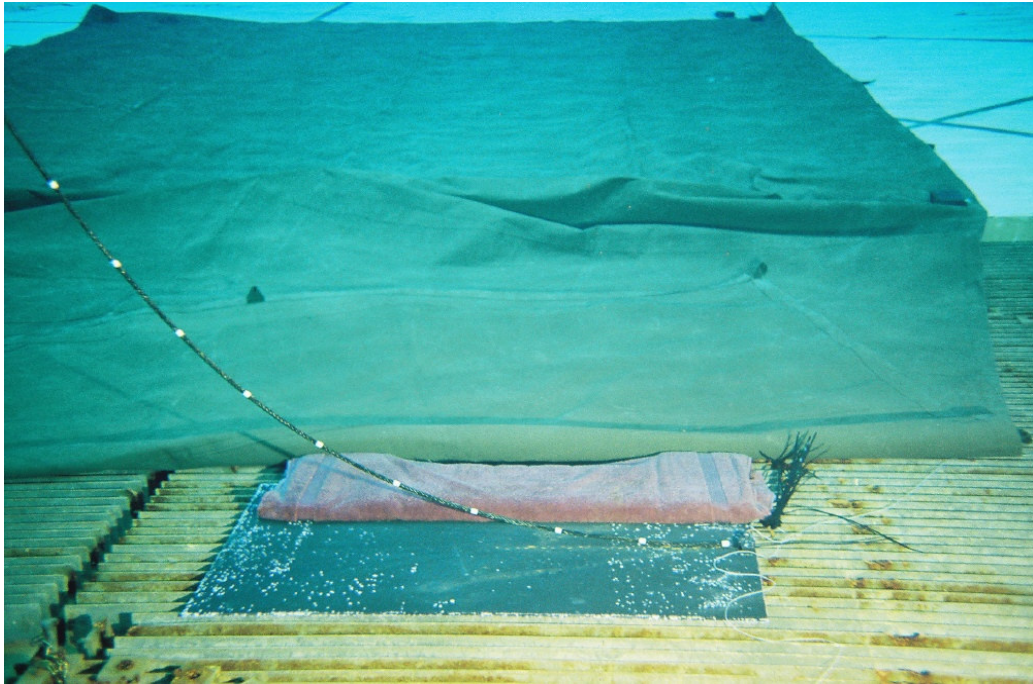
Figure 3.10   Semi-taut catenary mooring mount
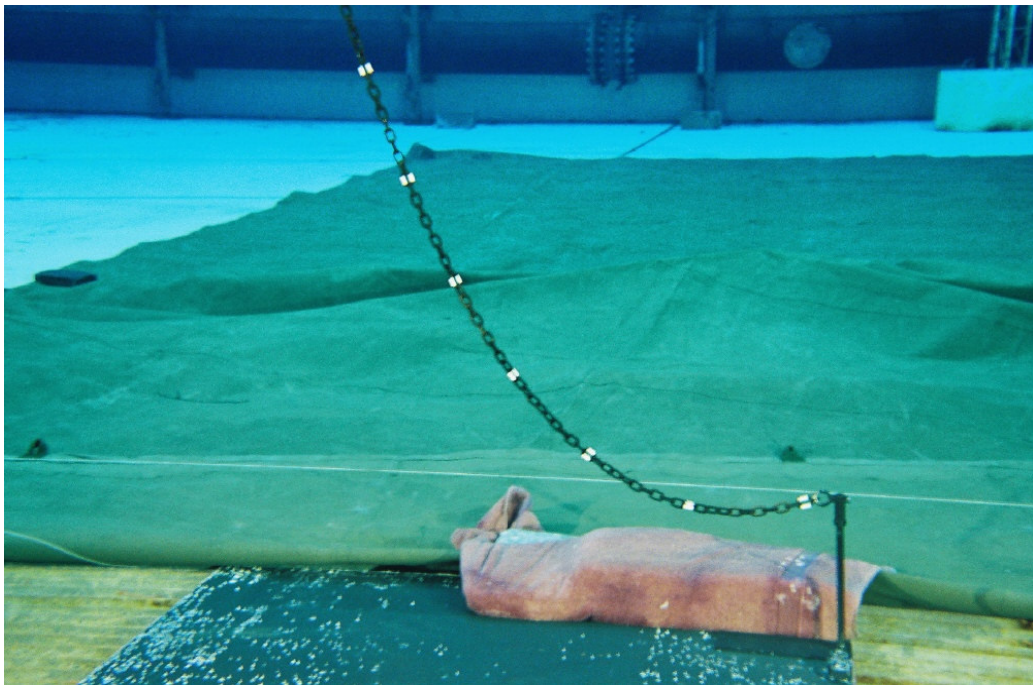
Figure 3.11   Suspended catenary mooring mount

<Semi-taut catenary mooring>   <Suspended catenary mooring>

Figure 3.12   Line configurations for forced oscillation tests

Table 3.4   Lowest natural frequency for each mooring configuration

Natural frequency [Hz]		Semi-taut catenary mooring			Suspended catenary mooring		
		Small	Medium	Big	Small	Medium	Big
Chain	Mode1	0.30719	0.30893	0.31072	0.31425	0.31602	0.31785
	Mode2	0.46220	0.46476	0.46740	0.41428	0.41659	0.41899
	Mode3	0.61064	0.61409	0.61766	0.63627	0.63985	0.64357
Wire	Mode1	0.28591	0.29064	0.29103	N/A		
	Mode2	0.43082	0.43784	0.43842			
	Mode3	0.56833	0.57774	0.57852			
Chain - Wire	Mode1	0.29416	0.29749	0.28863	N/A		
	Mode2	0.47075	0.47945	0.52086			
	Mode3	0.54753	0.55987	0.66401			

<Semi-taut catenary mooring>   <Suspended catenary mooring>
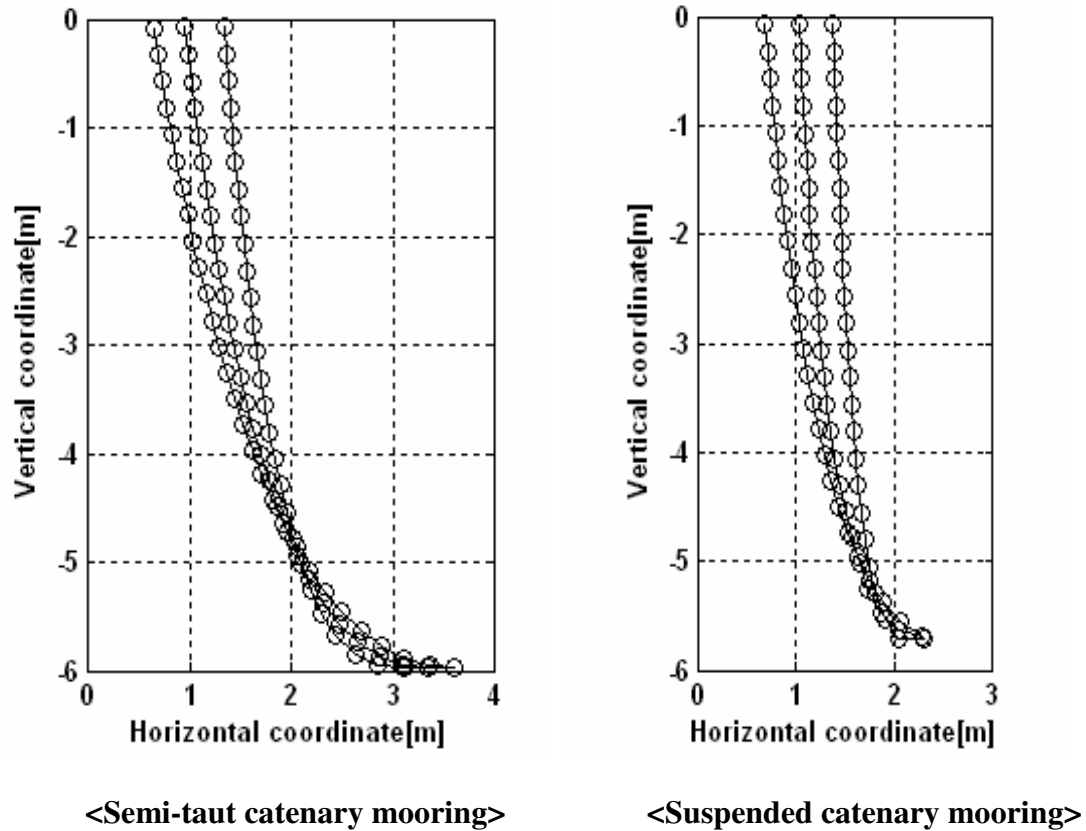
Figure 3.13   Sample trajectories from forced oscillation tests (maximum, mean,

and minimum excursion)

3.2. Data Processing

3.2.1. Video Processing

The video files recorded by the optical tracking camera were processed to extract time histories of position for all markers. Custom image processing software was developed using Matlab and applied to automate the video processing.

For the free oscillation tests, prior to image processing the time origin of the motion corresponding to the release of the chain should be determined. Since electrical synchronization between the camera and the line-release device was not available, the only way to determine the time origin is to watch the video frame by frame and identify what appears to be the best origin. It is not necessary to find the time origin for the forced oscillation tests since, as mentioned before, all of the experimental devices were synchronized together.

The images of the video are coded in grayscale values. One pixel can take a value from 0 to 255 intensity, 0 for black and 255 for white. The markers have to appear brighter than the background to be easily detected. So, if there were no noise, it would be enough to find those brighter points, above a value of 200 for example. However the video is not perfectly noise-free due to false illumination (reflections), scratches on the observation window, etc., which sometimes causes the video tracking software to fail. Thus some improvement of the image processing was required.

If noise from a certain frame is persistent in adjacent frames, by creating the difference between two frames one can eliminate a large part of the noise. The process is briefly described below:

1. Create the difference $P = 2M_q - M_2 - M_1$ where M_q is the matrix giving the intensity for the current image, M_2 is the matrix of the following image and M_1 the matrix of the prior image.

2. Then, keep every pixel of P above a given value. Those pixels should correspond to the markers.

3. Using the retained points, match one pixel for each marker.

4.   Finally, apply a spatial weighted average to all pixels associated with each marker to find the best middle pixel point of the marker.

To convert pixel values to actual positions, one has to determine the scale.   The scale is normally found by measuring the distance between calibrated marker locations placed at the extremities of the field of view (FOV).   For the large scale experiments in the OTRC basin where the size of the field of view FOV was quite large (approximately 5 m square), creating an array of calibration markers to be placed in the test area was a challenge.   In order to be physically manageable, a 2.5 m square plate that is one quarter of the size of the FOV was constructed with calibration markers evenly spaced in both the horizontal and vertical directions.   As illustrated in Figure 3.14, the calibration array was placed in one quadrant of the FOV at a time and the marker locations were recorded by the video camera for subsequent scale determination.

Two types of length scales were investigated.   One type is based on the distance from the centerline of the FOV.   In particular, calibration points were established at zero, 0.5 m, 1 m, 1.5 m, 2 m, and 2.5 m locations, where zero and 2.5 m indicate the center and outer margin of the FOV, respectively.   From this, two individual orthogonal quadratic curves of scale are obtained at the horizontal and vertical centerlines.   The other type of scale is the regular constant length scale taken from the total length of each row and column of markers (Figure 3.14).
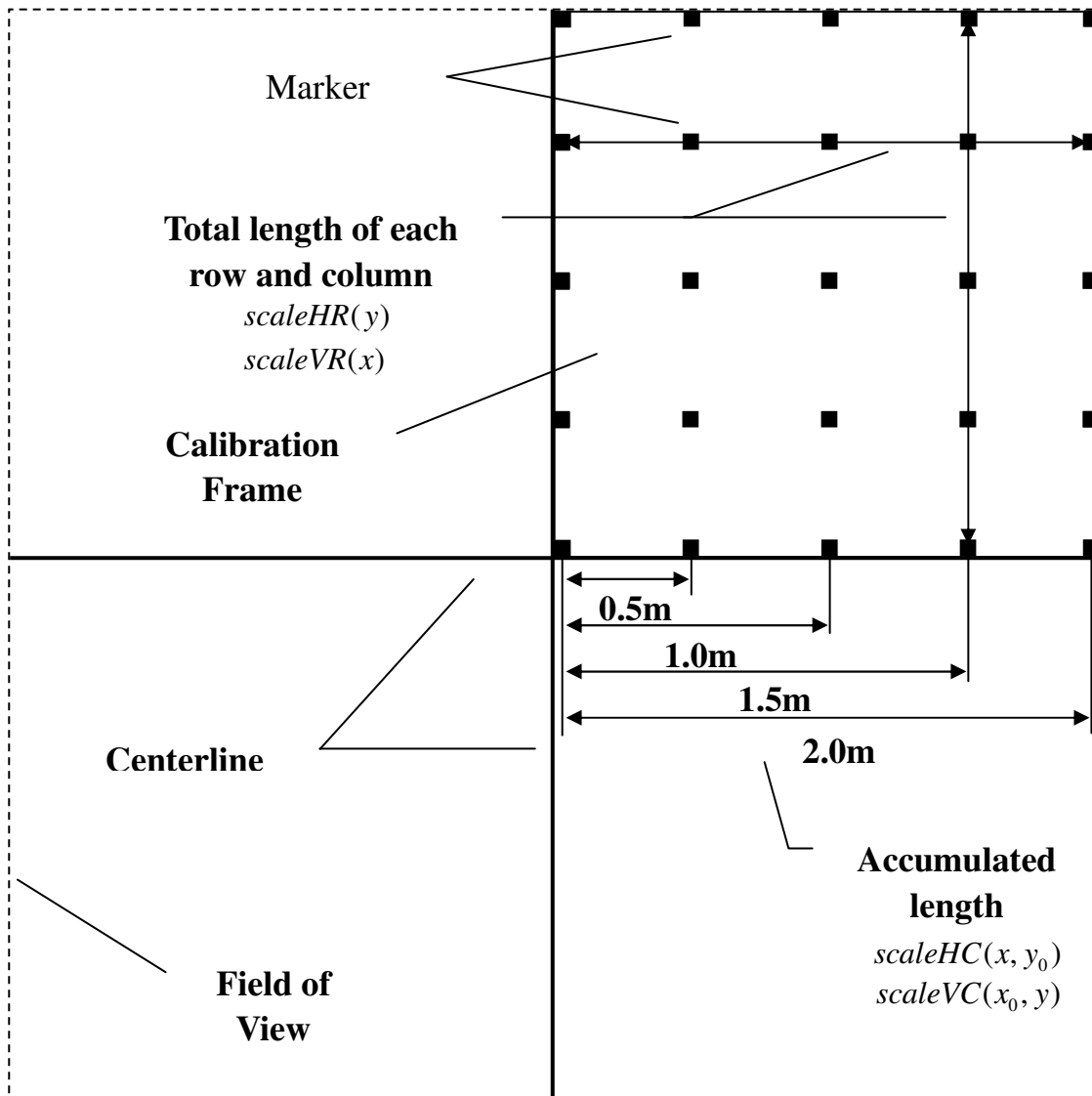
Figure 3.14   Length data for scale calibration

Calibration of scale at any location other than the centerline in the FOV is implemented by following equation:

$$ScaleH(x, y) = scaleHC(x, y_0) \times \frac{scaleHR(y)}{scaleHR(y_0)}$$

$$\text{(3.2)}$$

$$ScaleV(x, y) = scaleVC(x_0, y) \times \frac{scaleVR(x)}{scaleHR(x_0)}$$

where

$ScaleH$ and $ScaleV$: calibrated horizontal and vertical scale

$scaleHC(x, y_0)$ and $scaleVC(x_0, y)$: scale at centerline

$scaleHR(y)$ and $scaleVR(x)$: scale at each row and column

x and y : coordinates of any location within FOV

x_0 and y_0 : coordinates of centerline.

To verify the scale calibration, the inferred length of the mooring line recorded during forced oscillation and derived from use of the regular constant scale and the calibrated variable scale are compared. The total length of line and the time-averaged length of each segment are compared in Figure 3.15 and Figure 3.16, respectively. In both figures, considerably less variation in the inferred length (by almost half) is observed for the calibrated variable scale compared to the constant scale. The remaining small variation in total length associated with the variable scale is assumed to be due to the effect of out-of-plane motion (which is not readily excluded in reality although the experiment is set to be confined to in-plane motion) and due to errors in alignment of the calibration plate at each of the four quadrants.
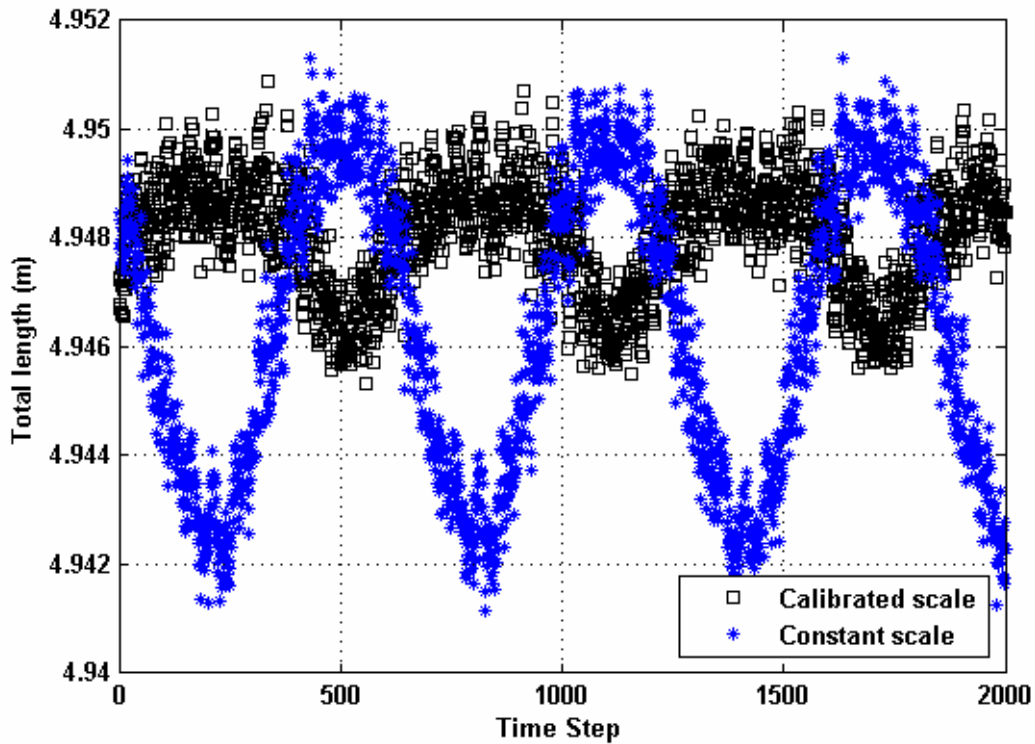
Figure 3.15   Comparison of total length of line between calibrated variable scale and regular constant scale

In Figure 3.16, the pattern of variation in the averaged length is considerably removed, which indicates that the calibration provides a good consistency of scale over the entire FOV.   It should be noted that the length of each segment of chain is not exactly equal due to manufacturing tolerances and errors in placement of markers. Thus, the small variation of the averaged segment length is considered to be acceptable.
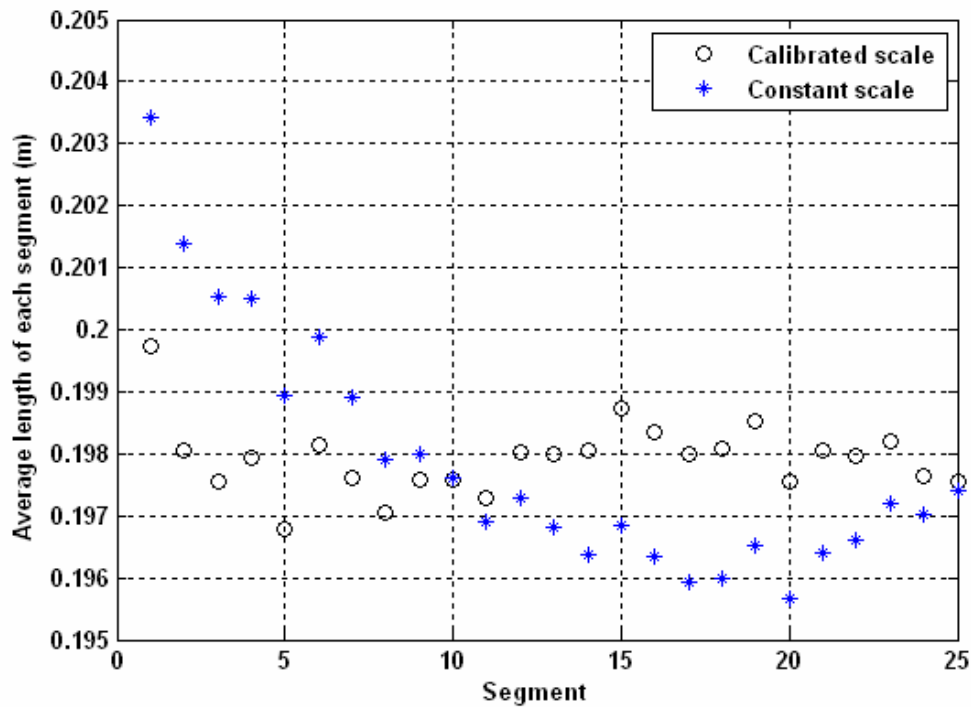
Figure 3.16   Comparison of time averaged length of each segment between

calibrated scale and regular constant scale

3.2.2. Geometric Processing

In the experimental analysis, the Euler angles and the velocity and acceleration of each segment will be used to solve the dynamic equation of motion for the mooring line. From the measured position vectors, the velocity and acceleration of each node can be directly calculated using finite difference formulas.   To find the Euler angles between the mooring line and the horizontal axes at the node points of interest, cubic spline interpolation is used to approximate the shape of the curve.   Cubic spline interpolation

means that each portion of the line between two nodes is interpolated using a third order polynomial function, which ensures that the first and second order derivatives are continuous everywhere, including at node boundaries between line segments.
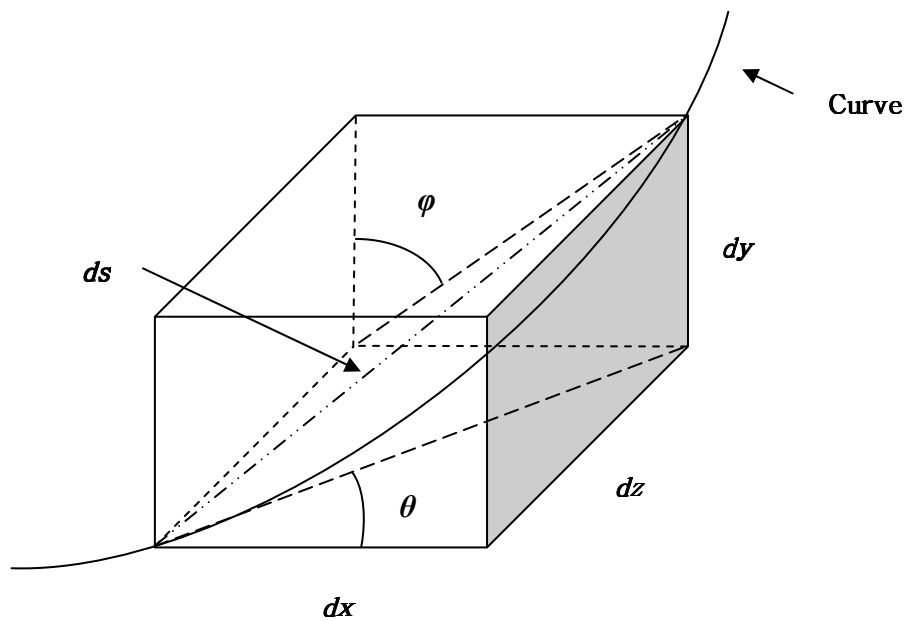
Figure 3.17   Geometry of differential length of curve

Once the polynomial functions for each segment are obtained, the angles and length can be calculated straightforwardly. If $y = f(x)$, and $z = g(x)$ are the polynomial functions for the space curve segment between nodes A and B, the Euler angles and the length of the segment (length of the curve) are

$$\phi \;=\; \tan^{-1}\left(f(x)'\right) \quad \text{and} \quad \theta \;=\; \tan^{-1}\left(g(x)'\right) \tag{3.3}$$

$$S \;=\; \int_A^B ds \;=\; \int_A^B \sqrt{1+\left(\frac{dy}{dx}\right)^2+\left(\frac{dz}{dx}\right)^2}\; dx \tag{3.4}$$

where $\quad ds = \sqrt{dx^2+dy^2+dz^2} \;=\; \sqrt{1+\left(\dfrac{dy}{dx}\right)^2+\left(\dfrac{dz}{dx}\right)^2}\; dx \quad$ (refer to Figure 3.17).

For calculation of values at mid-points of line segments, the averaged kinematic values of two adjacent nodes might be used in the analysis, but this would generate some unnecessary errors. To prevent this, the effect of the curvature of the line segment should be considered. The mid-point of any given segment can be found as follows:

1. First, divide the segment into N parts, A_1, A_2, …, A_n, … as shown in Figure 3.18.

2. Calculate the length from point A to each A_n.

3. When this length is equal to L/2, the position vector of the mid-point is obtained.

Using the interpolated point, the velocities, accelerations and angles are calculated, instead of using the mid-point of the straight segment AB. Furthermore, by using this procedure the discretization of one segment into several sub-segments can be readily accomplished.
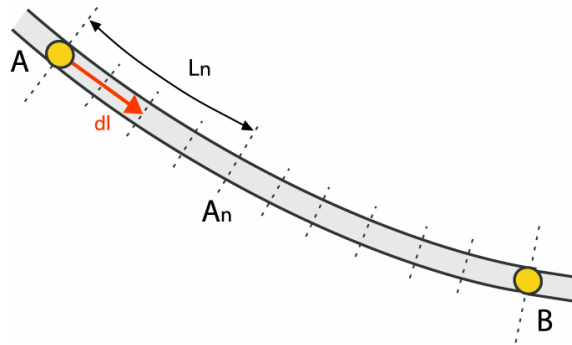
Figure 3.18 Discretization of individual segment

3.2.3. Optical Tracking Error

Comparing the length of line over the entire time series of motion gives an indication of the errors involved with recording and extracting the coordinates of each node, because as shown in Figure 3.19 considerable difference in length is observed Recording errors are caused by distortion of the picture and 3-D (out-of-plane) motion effects. The distortion is generated by parallax of the camera lens, and can be perfectly solved with a parallax compensation lens. However such a lens was not employed in this study, so scale calibration has been implemented to reduce the scaling error of the distorted image (Section 3.2.1). The transverse (out-of-plane) motion of the line might be induced by fluid lift forces and VIV (vortex-induced-vibration) which are real, unavoidable effects. Out-of-plane motions can also be generated if the ends of the mooring line are not perfectly aligned in the plane of the FOV at initial set-up. Thus, even if the experimental set-up is intentionally confined to 2-D planar motion, 3-D effects cannot be completely excluded. Introducing another camera to record

information on the transverse coordinate would handle the issues addressed above but at the expense of increased complexity in image processing.
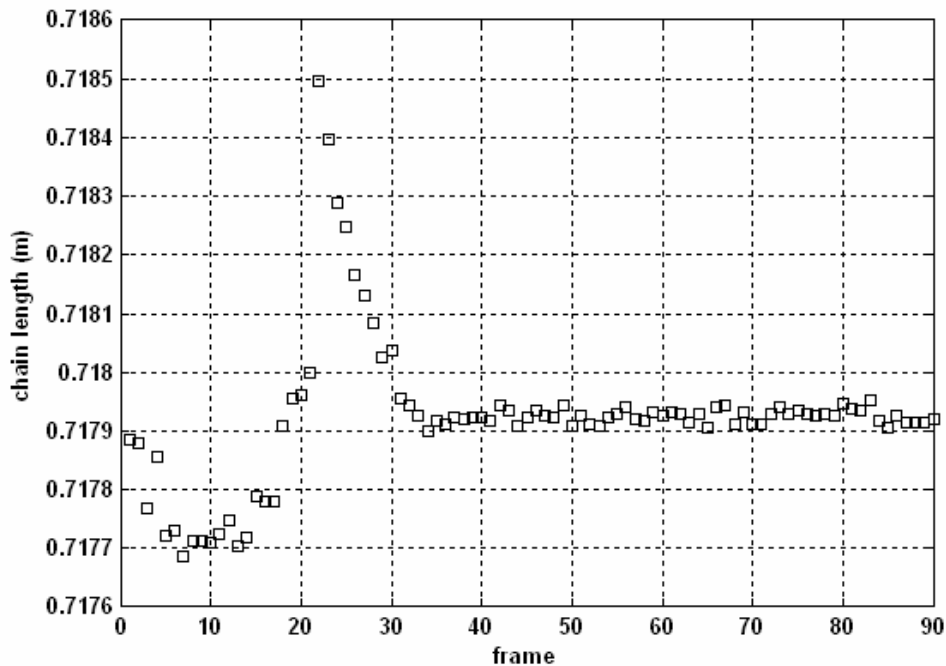
Figure 3.19   Variation of the measured length of the big chain during free oscillation

Another possible optical tracking error is inconsistency in detecting the center-point of each reflective marker from frame to frame.   In the recorded image, any given marker is composed of several pixels.   The number of pixels associated with each marker in the initial time step should be retained over the entire time series. However,

due to the relatively high speed of the mooring line motion and the non-uniform intensity of lighting, some pixels occasionally appear to be blurred or some of them are not clear enough to be identified as part of the marker. Moreover mooring line torsional rotation during oscillation results in a change of the original shape of the marker in the image. All of these effects increase the error associated with node-center selection.
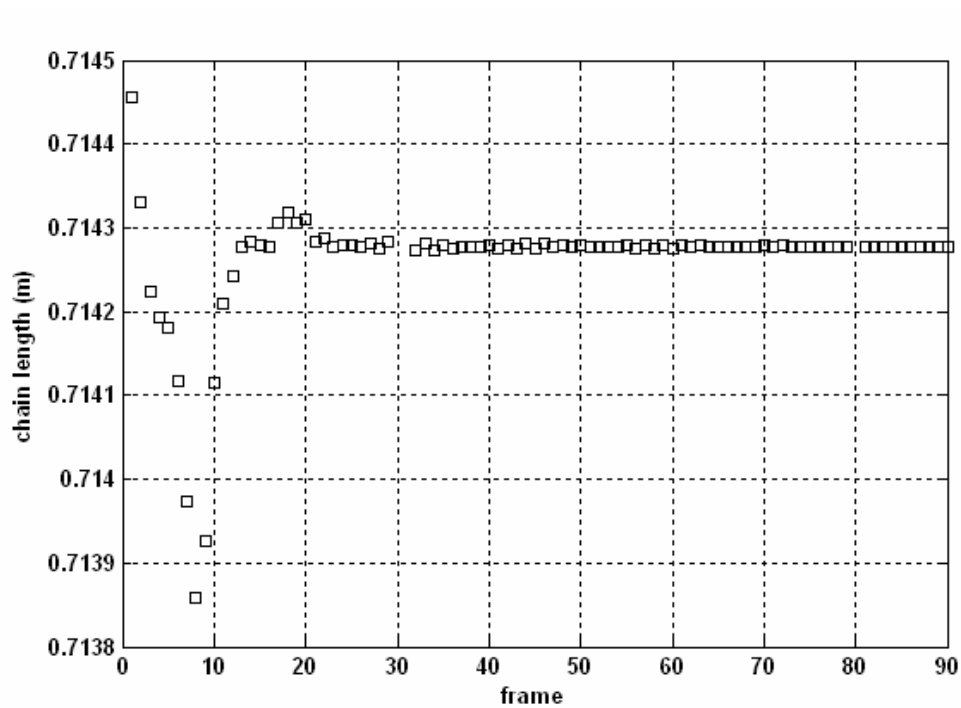

Figure 3.20   Variation of the length of the big chain during numerical simulation of free oscillation

Another source of error is numerical errors in the data processing algorithm. To investigate this error, a numerical simulation of a free oscillation test was performed and the simulation data was processed in the same was as for the experimental data. Figure 3.20 shows the line length results from the numerical simulation of the test corresponding to the results in Figure 3.19. It appears that the numerical processing errors are comparable to the experimental optical tracking errors, resulting in length errors of less than 1 mm over a total length of ~715 mm (i.e. errors of order 0.1%).

3.2.4. Data Resampling by Polynomial Regression

When we plot the linkage of all the nodes initially extracted from an image, it looks like a connection of straight line segments with angle-inconsistency at node (marker) locations resulting from the position measurement errors described above. In Figure 3.21, the middle node is located above the polynomial regression line while the other two are below the line. This indicates an inconsistency in the shape of the curved line. By nature, a single curved line must be smooth and angles at adjacent nodes must be consistent. In order to make a line smooth and achieve consistency, resampling is carried out by means of polynomial regression. Alternative equations such as exponential and hyperbolic equations might be applied but, after testing various equations, the polynomial equation proved to be the best approximation for the curvilinear shape of a mooring line in motion.
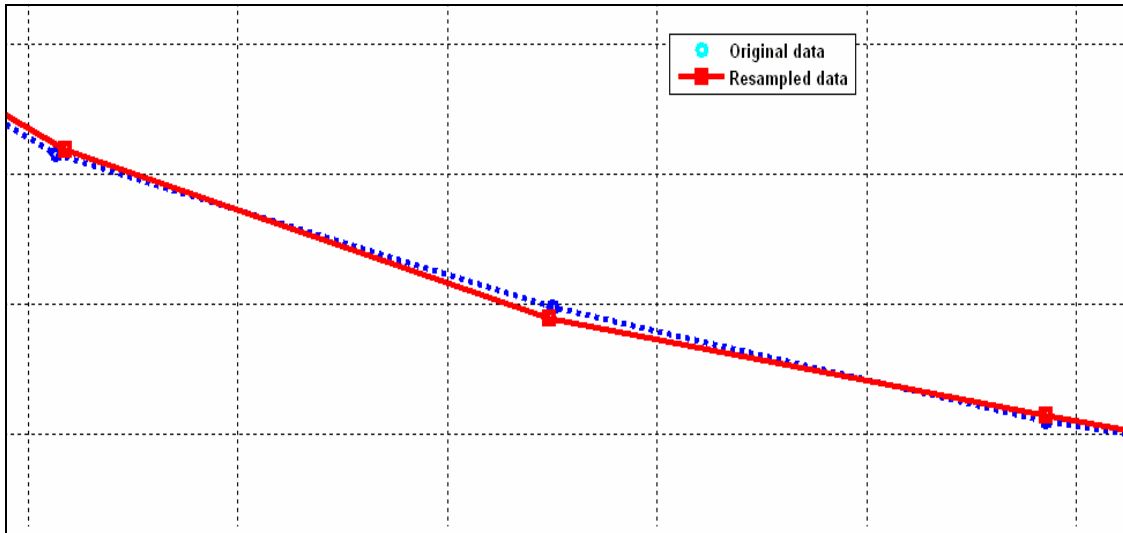
Figure 3.21   Comparison of three node positions for original and resampled data

Since the length of each segment is known, each node point is newly selected by the method given in section 3.2.2, providing frame-to-frame consistency in the total length of the moving line.   The order of the polynomial is determined through trial and error by checking the curve of the original data and the new resampled data until a satisfactory result is obtained.   Various orders of polynomials are required to adequately represent each different configuration of mooring line (semi-taut or suspended catenary). Occasionally two polynomial equations of low order might be preferable to a single equation of higher order.   In that case, the mooring line is split into two sections with at least one overlapping segment to provide continuity between the two sections, and then each low order equation is fitted to a corresponding section while forcing a match at the joint nodes.
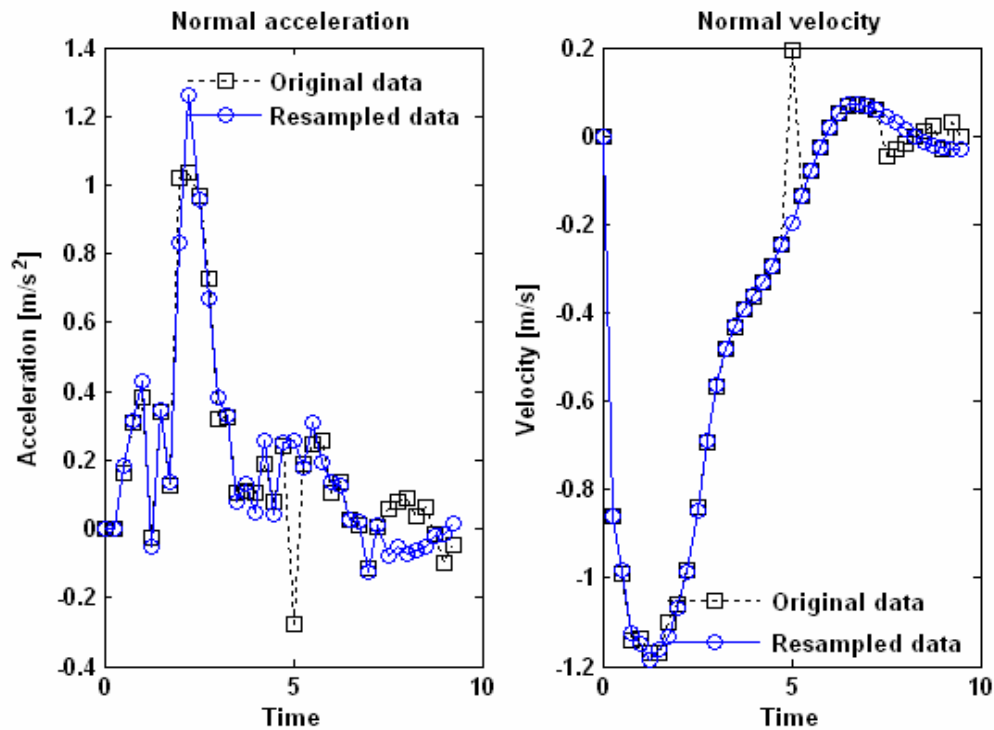
Figure 3.22   Comparison of kinematic profile between original and resampled data

In general, one might expect the overall motion to become smooth and consistent in time after polynomial resampling.   The results can be verified through observation of velocity and acceleration time series before and after resampling, as shown in Figure 3.22.   For the case of forced oscillation, the resampling process also partly contributes to restituting the sinusoidal pattern of the line kinematics, which hardly remains in the original data.   Also, the resampling process might remove some transverse 3-D effects to a certain degree since both the length and shape of the line are recovered comparatively.

3.2.5. Filtering

Experimental time series data is generally accompanied by some noise which might significantly distort subsequently derived results, so some form of filtering is required to remove the noise. In the present study two different types of measurements were made: force and image data. The former is obtained by a strain gauge device while the latter is recorded by an optical device. Accordingly, the noise characteristics could be different for each device. One might consider designing and applying individual filters to each data set. However compatibilities between the two sets of data should be preserved because they are synchronized and applied for dynamic analysis. Consequently a single low pass filter was designed and applied to all data sets.

The Butterworth filter was selected for low-pass filtering because it has a maximally flat response in the passband with no ripples in either the passband or the stopband, as shown in Figure 3.23. A drawback of the Butterworth filter is that the frequency response rolls off slowly between the passband and the stopband, thus a higher order filter is required to achieve a sharper roll-off.
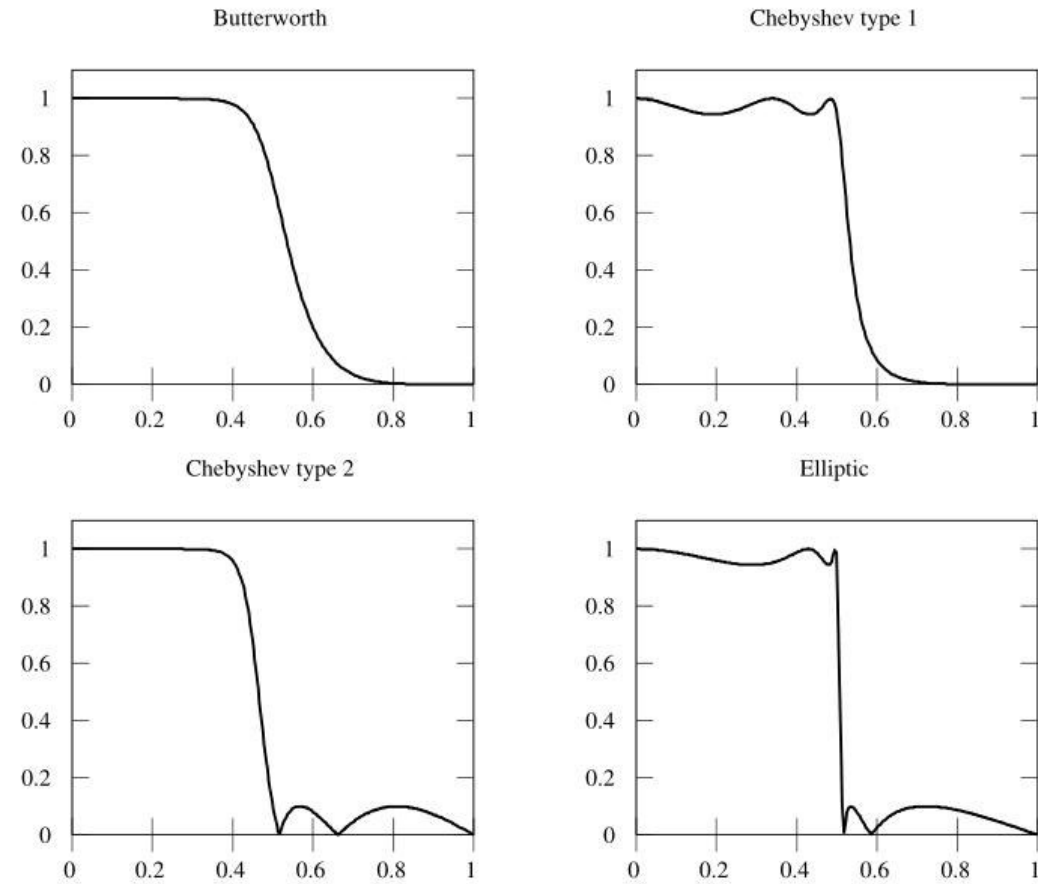
Figure 3.23   Comparison of frequency response for a variety of electronic filters

(horizontal axis: normalized frequency, vertical axis: frequency response)

The transfer function *H(s)* of the Butterworth filter is the ratio of the output signal to the input signal expressed as a function of complex frequency *s* and may be expressed in the polynomial form

$$H(s) \; = \; \frac{X_{out}(s)}{X_{in}(s)} \; = \; \frac{R_0}{\prod_{k=1}^{n}(s-s_k)/\omega_c} \tag{3.5}$$

where $s = \sigma + j\omega$:   complex frequency

n : order of filter

R_0 : frequency response at zero frequency

ω_c : cutoff frequency.

The frequency response $R(s)$ of the Butterworth filter is expressed in terms of the transfer function as

$$R^2(\omega) = \left| H(j\omega) \right|^2 = \frac{R_0^2}{1 + \left(\omega/\omega_c \right)^{2n}} \tag{3.6}$$

and the response as a function of normalized frequency is shown in Figure 3.23. The phase shift induced by the filter is

$$\varphi(\omega) = \arg\left[H(j\omega) \right] \tag{3.7}$$

where $\arg[\ ]$: complex argument.

In order to avoid filter-induced phase distortion in the synchronized data sets, one should employ so-called zero-phase filtering. The process of zero-phase filtering is as follows:

1. filter the time series data once in the forward direction,

2. then reverse the filtered sequence for a second filtering pass, and

3. finally flip the sequence again.

During the process, all induced phases are canceled out by their counterparts. The zero-phase filtering was conducted by the Matlab intrinsic function "filtfilt".
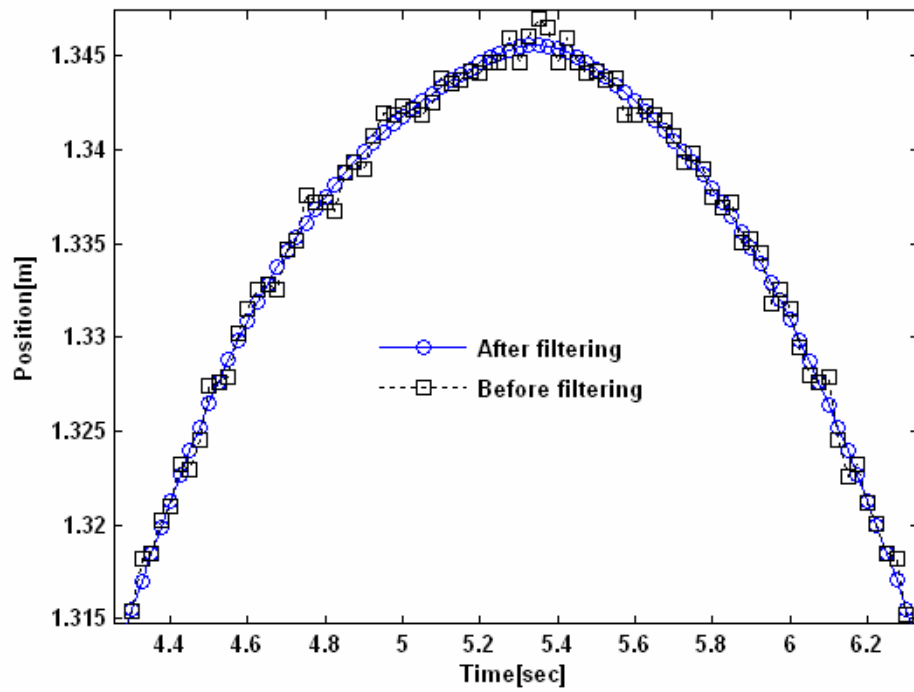
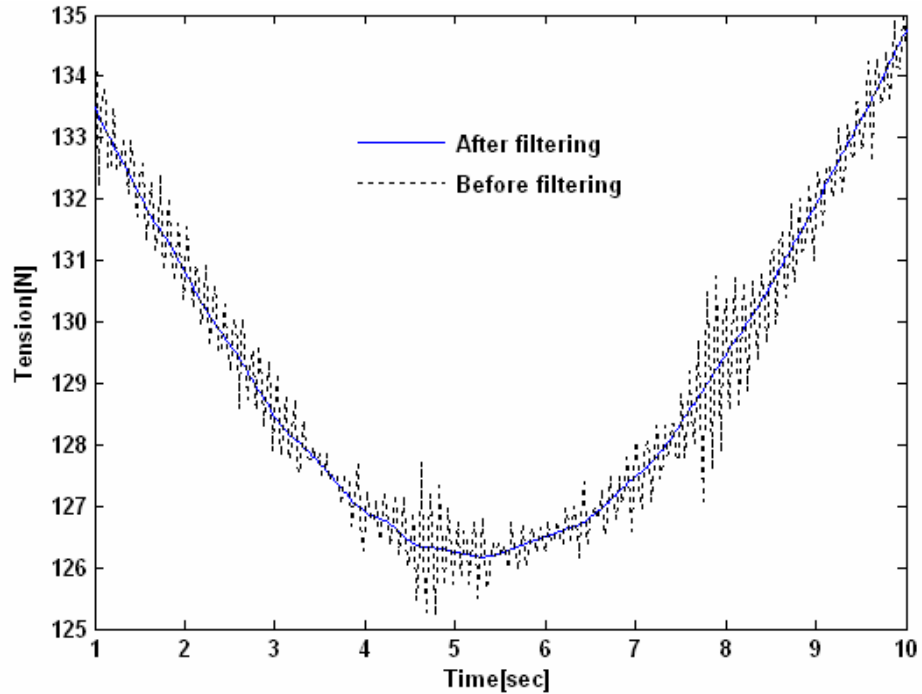**Figure 3.24   Horizontal position vector before and after Butterworth filtering**

Figure 3.25   Tension data before and after Butterworth filtering

The design of a Butterworth filter involves specification of two parameters: the order of the filter and the cutoff frequency. The order of the filter controls the slope of the roll-off between the passband and the stopband, with higher order providing better high frequency attenuation. The cutoff frequency determines the width of the passband. In filtering the recorded data sets, a single 3rd order filter with 10 Hz cutoff frequency was applied.

Figure 3.24 and Figure 3.25 illustrate the effectiveness of zero-phase Butterworth filtering the position and tension data, respectively, in removing the high frequency noise while retaining the sinusoidal response. The effectiveness of the filtering is even more pronounced in the velocity and acceleration signals derived from the filtered position data, as illustrated in Figure 3.26 and Figure 3.27. It is observed that the sinusoidal response is significantly recovered in the normal acceleration signal after reconstructing the position data by filtering. The recovery of the sinusoidal response in the kinematics increases the reliability of the drag or added mass coefficients determined by Fourier analysis of the measured line displacement. From all the results shown, the importance of filtering the experimental data can be clearly perceived.

The wiggly shape of the acceleration still apparent in the filtered signal shown in Figure 3.27 is not a desirable feature in the ideal case. A second filtering pass could be performed to smooth out this apparent extra noise. Or one might process the velocity and acceleration directly instead of applying a filter to the position vector. However, while the profiles of kinematics would become smoother, this would distort each harmonic component and cause the kinematic data to be incompatible with the tension data. Therefore direct filtering of the velocity and acceleration signals is not desirable.
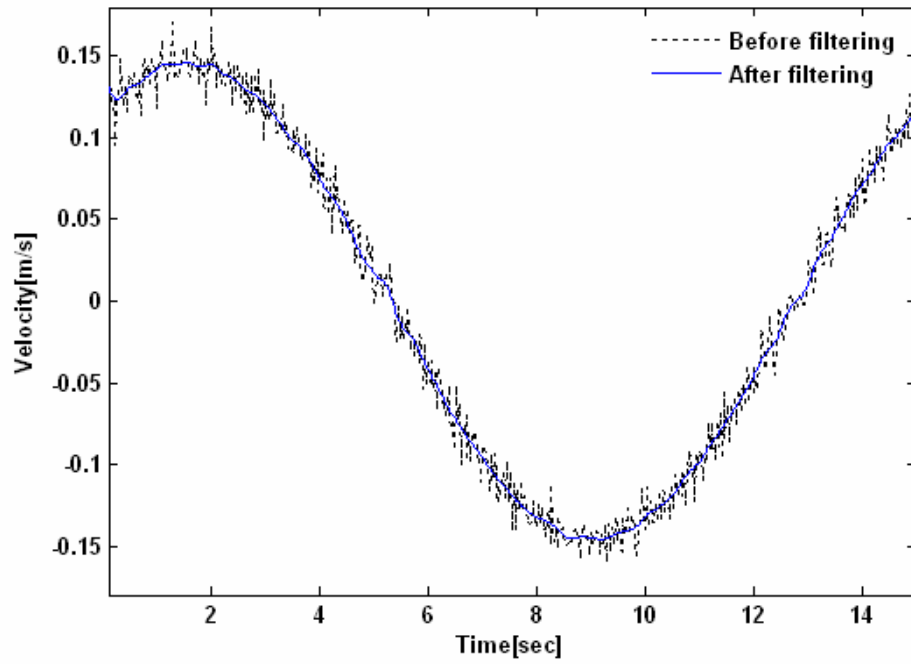
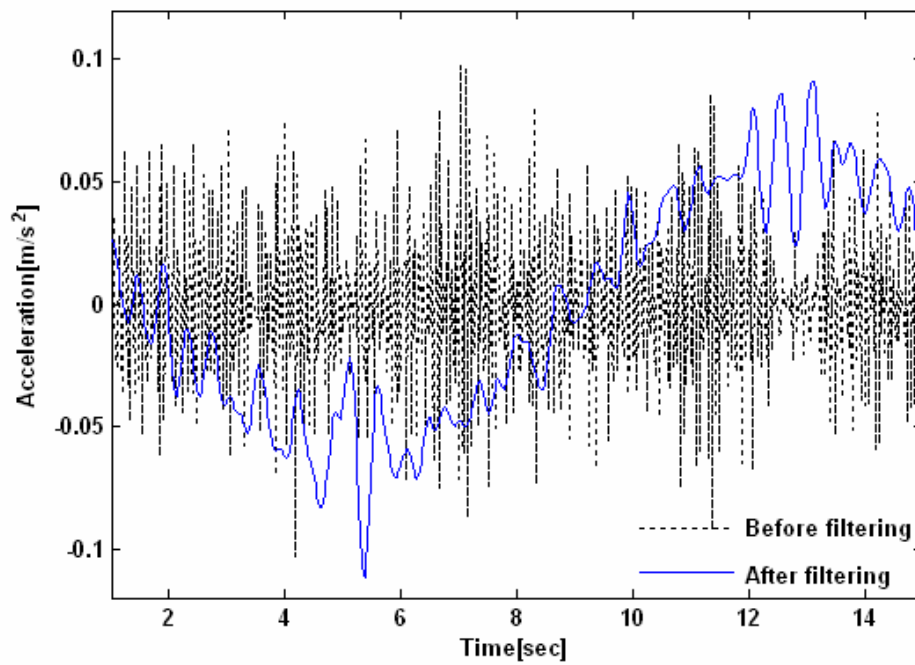**Figure 3.26   Normal velocity before and after Butterworth filtering**

Figure 3.27   Normal acceleration before and after Butterworth filtering

3.2.6. Error Analysis

Since calculation of line dynamics will be conducted using the experimental data, both numerical and experimental errors will exist. Errors associated with measurements of position data are the primary source of error, and this error propagates into the derived velocity and acceleration data. Kinematics are computed through the finite difference method based on position vectors, so numerical truncation error inherently arises. However, since a 5-point scheme is employed for both first and second order time derivatives, one may assume that the truncation error is small enough to be negligible. Thus, a major concern is focused on the measurement uncertainties which might be considered to substantially contaminate the inferred line dynamics and must be analyzed to validate the measurements.

As mentioned, the error in the optical tracking data (position vectors) is mostly attributed to image distortion and inconsistency of node-point selection, which are characterized as systematic and random errors, respectively. Using data from a forced oscillation test, the position uncertainty can be approximately obtained by comparing the optical tracking measurement of the top node with the hydraulic ram displacement measured by the MLDT (Magnetostrictive Linear Displacement Transducer) controller feedback signal, under the assumption that the top node almost follows the driving motion of the ram. The calculated displacement error as a function of time and its standard error are shown in Figure 3.28. In general terminology, the standard error is referred to as the standard deviation of the mean and can be calculated as

$$S_e = \frac{\sigma}{\sqrt{N}} = \sqrt{\frac{\sum_{i=1}^{N}(x_i - \bar{x})^2}{N(N-1)}} \tag{3.8}$$

where N is the number of repeated data. However in the present context the standard error is computed as the standard deviation of error since there is no repeated data for any specific point.

Velocity and acceleration are calculated from measured position data and therefore their corresponding errors can be estimated from the position error. Uncertainty propagation of a derived quantity is predicted as follows. If $F(x_1, x_2, ..., x_n) = R$ is a derived quantity and $x_1, x_2, ..., x_n$ are measurements of n variables, then

$$\Delta R = \sqrt{\left(\frac{\partial F}{\partial x_1}\right)^2 (\Delta x_1)^2 + \left(\frac{\partial F}{\partial x_2}\right)^2 (\Delta x_2)^2 + ... + \left(\frac{\partial F}{\partial x_n}\right)^2 (\Delta x_n)^2} \tag{3.9}$$

If $R = x_1 \pm x_2 ... \pm x_n$, then

$$\Delta R = \sqrt{(\Delta x_1)^2 + (\Delta x_2)^2 + ... + (\Delta x_n)^2} \tag{3.10}$$

where ΔR : uncertainty in the derived quantity

$\Delta x_1, \Delta x_2, ..., \Delta x_n$: uncertainty in each measured variable.
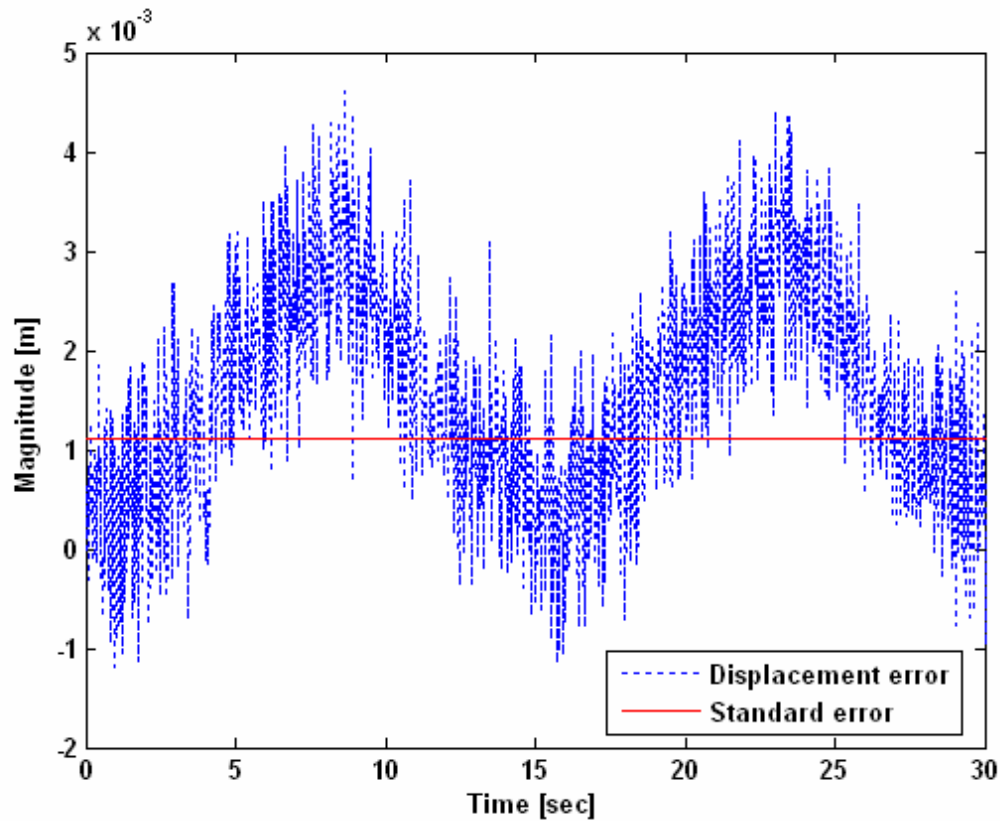
Figure 3.28   Experimental error and standard error for the position vector of the

top node at each time step

For the case of low-frequency (1/15 Hz) forced oscillation, using the standard error

of 0.0011 m at the sampling rate of 40 Hz (Figure 3.28), the error propagation in velocity

and acceleration are predicted as 0.0312 m/s and 4.3251 m/s^2, respectively.   Reducing

the sampling rate from 40 Hz to 10 Hz results in significant improvement, reducing the

error to as low as 0.0066 m/s and 0.2282 m/s^2.   Comparing with the mean value of

velocity (0.1038 m/s) and acceleration (0.0435 m/s^2), the uncertainty associated with

acceleration appears to be much larger than the mean value while the uncertainty in velocity is less than 10% of the mean. It is therefore inferred that acceleration-dependent results such as the added mass coefficient might not be reliable without further reduction of the error. However for the case of high-frequency (1/5 Hz) oscillations, the mean of the acceleration is twice the magnitude of the uncertainty, which might provide 50% reliability. Note that along with decreasing the sampling rate, data filtering is applied to reduce experimental errors.

CHAPTER IV
RESULTS AND DISCUSSION

4.1. Introduction

The previous chapters have documented the theoretical and experimental techniques employed for this study of the dynamics of mooring lines. In this chapter, a detailed discussion regarding the hydrodynamic characteristics of various mooring elements is presented, based on the results of free and forced oscillation tests. Instead of analyzing the motion of the mooring line itself, the primary focus is on extracting the hydrodynamic force transfer coefficients, which in deepwater may have a significant influence on the motion of a moored body. Before the analysis of the oscillation tests, the measurement of bending stiffness for wire rope elements is presented. In order to validate the present experimental method of identifying force transfer coefficients for mooring lines, forward simulation of a mooring line with experimentally derived hydrodynamic coefficients is performed using the commercial program OrcaFlex. Also, comparisons of numerical simulations with experimental data are provided focusing on the impedance to horizontal floater motions provided by hydrodynamic forces on a mooring line.
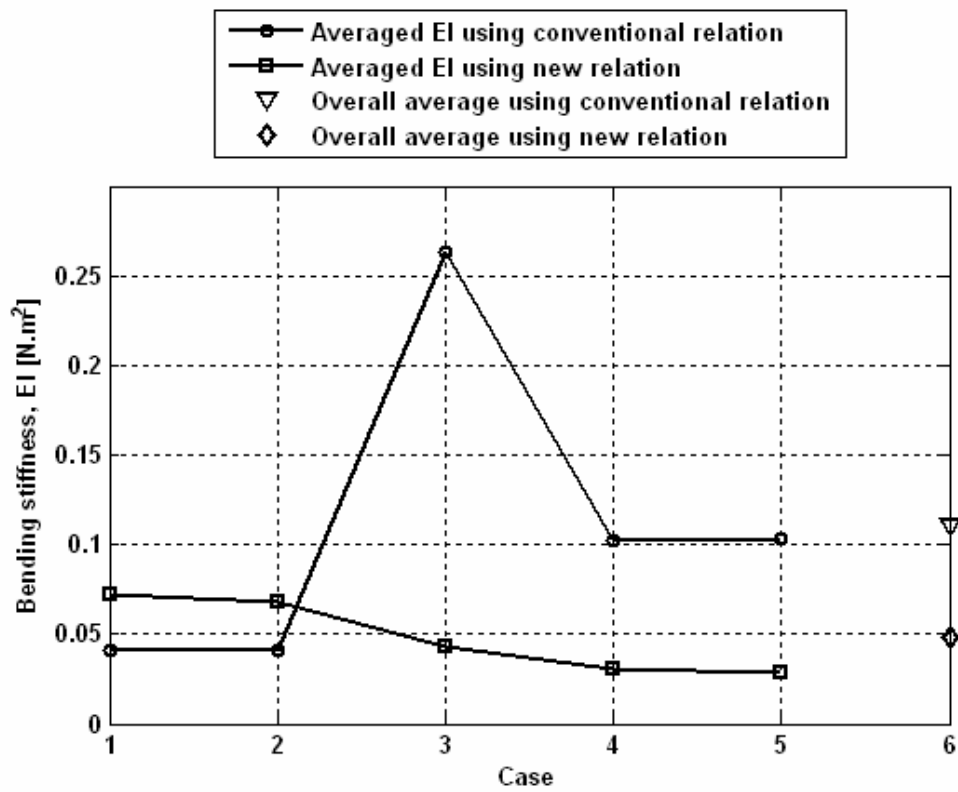
4.2. Measurement of Bending Stiffness

Steel cable and wire rope are widely used as mooring line elements. For lengths on the order of hundreds of meters the effect of bending stiffness may generally be

neglected. However for lengths of order 10 m or less (as used in the experiments described in Chapter III), the bending stiffness of the cable may cause significant internal shear forces due to line curvature. In this case if the bending stiffness is neglected the inferred hydrodynamic force that is oriented in the normal direction can be significantly contaminated if bending stiffness effects are not taken into account. For this reason, attempts were made to measure the bending stiffness of the wire rope segments used in this study, in order to further investigate the effect of bending stiffness on the hydrodynamics of a mooring line.

As mentioned in Section 2.8, an indirect measurement technique was applied which derives the bending stiffness by solving the static equilibrium equation (2.55) with the measured position vector and the measured internal end force of a hanging wire span. Measurements were made for wires of three different diameters (Table 3.3) and each wire was tested for various line lengths and spans, as indicated in Table 4.1, where span is the straight horizontal distance between both ends of the hanging wire. Applying a finite difference scheme with variable grid size to equation (2.55) yields the explicit system equations from which tension and shear force at each node can be calculated. Then, the bending stiffness at each node is obtained through the relations in equations (2.56) or (2.59). Since this is an indirect measurement with some errors in the position vector, variation of the inferred bending stiffness along the longitudinal section is expected. Averaging of the variation over the entire uniform section is therefore justified to arrive at a single representative value of the bending stiffness.

Table 4.1   Length and span of wire for each test of bending stiffness

Case	1	2	3	4	5
Length [m]	0.5	0.5	1.0	1.0	2.0
Span [m]	0.37	0.45	0.74	0.90	1.75

Figure 4.1   Bending stiffness of big wire

In Figure 4.1 through Figure 4.3, results from both relations (2.56) and (2.59) are presented for each measurement case and 'Case 6' indicates the case-averaged value for each wire. As expected, increase in the size of the wire is correlated with increase in the bending stiffness. The ratio of diameter to stiffness for the three wires is not obvious because the wires are built up with different strand structures varying from 6 by 19 to 6 by 37, where the first numeral denotes the number of strands and the second numeral denotes the number of sub-wires constituting a single strand.

Considerable variation in bending stiffness among the cases is observed for both relations. This may be attributed to several sources: measurement errors of position vector and internal force, and distorted material characteristics associated with the inherent condition of the pre-rolled shape from the manufacturer. The former can be improved by developing a fit-for-purpose laboratory device and measurement skill, but it is not feasible to handle the latter. As shown, the magnitude of the bending stiffness is quite small for the wire rope segments studies, less than 0.1 N-m^2. So, if one applies the present measurement technique to materials with less bending flexibility, these errors are expected to become negligible.

Generally, the bending stiffness inferred from relation (2.56) appears to be larger and more variable compared with that from (2.59). Since the exact value of bending stiffness is unknown, evaluating the performance of both methods from the results given here is not readily achievable. However, relation (2.59) should be more accurate than (2.56) as it does not depend on an assumption of small curvature, and this seems to be supported by the lower degree of variability in the EI values derived using relation (2.59).
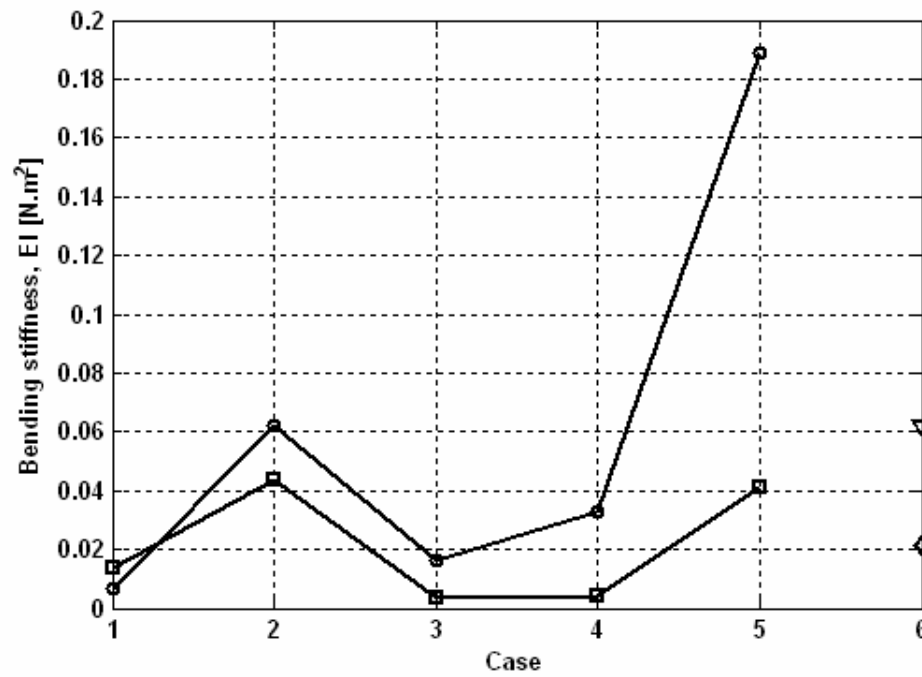
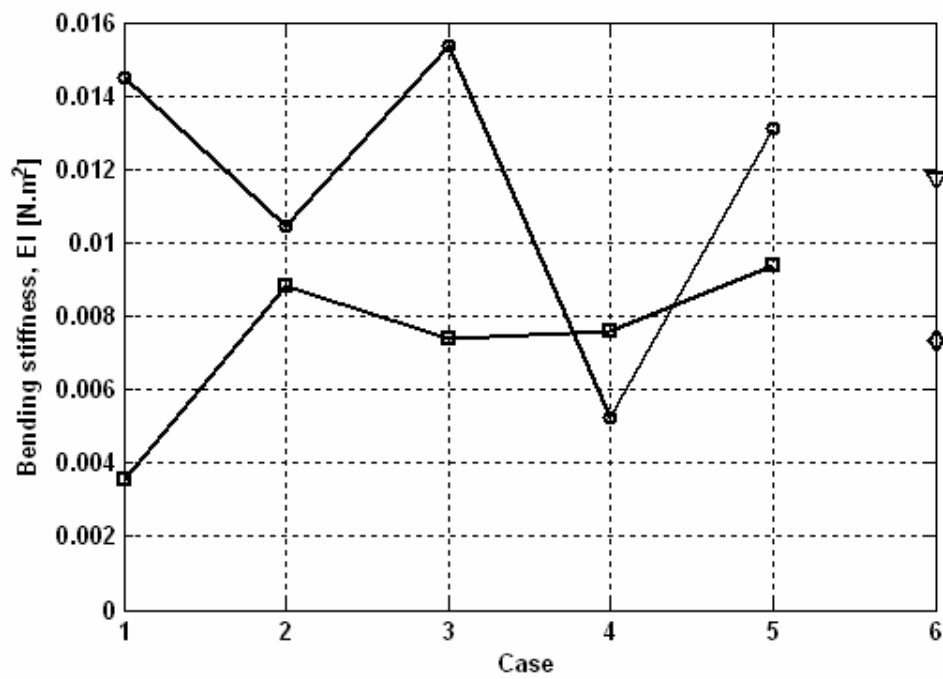**Figure 4.2   Bending stiffness of medium wire**

Figure 4.3   Bending stiffness of small wire

The present measurement method is found to be more efficient for the case with short length and span because in that case larger shear forces relative to tension are generated at both ends, so that static equilibrium and bending stiffness can be computed with relatively small error. If the end tension is set to too small in the laboratory setup, large errors could be generated as a result of the static calculation, resulting in a fluctuating pattern of bending stiffness along the length of the cable. Thus, it is noted that length and span must be adjusted to keep an adequate ratio between shear force and tension, for example, one where the shear force is twice as large as the tension. For experiments with materials with large bending stiffness, the results might not be much affected by the shear:tension ratio.

4.3. Free Oscillation Tests

4.3.1. Preliminary Results

For free oscillation tests only one force coefficient out of two is obtained by solving the dynamic equations given in the previous chapter because Fourier analysis is not applicable. All kinematics are derived from the measured position vector, and hence only the internal force and hydrodynamic coefficients remain unknown. The number of unknown variables is still more than the number of equations, thus an assumption associated with the hydrodynamic force is required to yield a closed system. By introducing the boundary condition of zero tension at the free end of the line and the assumption that the added mass coefficient is known and constant, the equation of motion can be solved for the instantaneous value of the drag coefficient at every time

step.   The above assumption is made on the basis that, for free oscillations, the inertia force due to the added mass is generally an order of magnitude smaller than the drag force.

The calculated drag coefficients, C_d, of the big chain are plotted against Reynolds number (Re) in Figure 4.4.   As shown in the figure, C_d at low Re, corresponding to the velocity data collected in the upper part of the chain, is unreasonably larger than conventional C_d values for a cylinder and there is considerable scatter in the C_d values. This may be due to several factors.   One is related to numerical error accumulated from the free-end segment toward the pivot-end segment as the explicit calculation proceeds. For segments close to the pivot point, every term in the equation of motion is very small so that even a very small error can have a big influence on the results.   Another factor is the simplifying assumptions made in the analysis, such as no friction drag, constant added mass coefficient, Morison force representation of hydrodynamics, etc.

To check the influence of added mass, C_d values derived by assuming $C_m=2$ are plotted in Figure 4.5.   Comparing Figure 4.4 and Figure 4.5, it is evident that for free oscillations C_m does not have a large effect on the hydrodynamic behavior of the chain in the tested range of Reynolds number, which is in agreement with the assumption made in the computational procedure.   Further increasing the added mass coefficient does not significantly affect the results, thus Cm of unity is assumed to be a reasonable value for the calculation of C_d from free oscillation tests hereafter.   However, in order to estimate reliable force coefficients applicable to real design of mooring line systems, it is desirable to make a parallel investigation of both drag and added mass force.
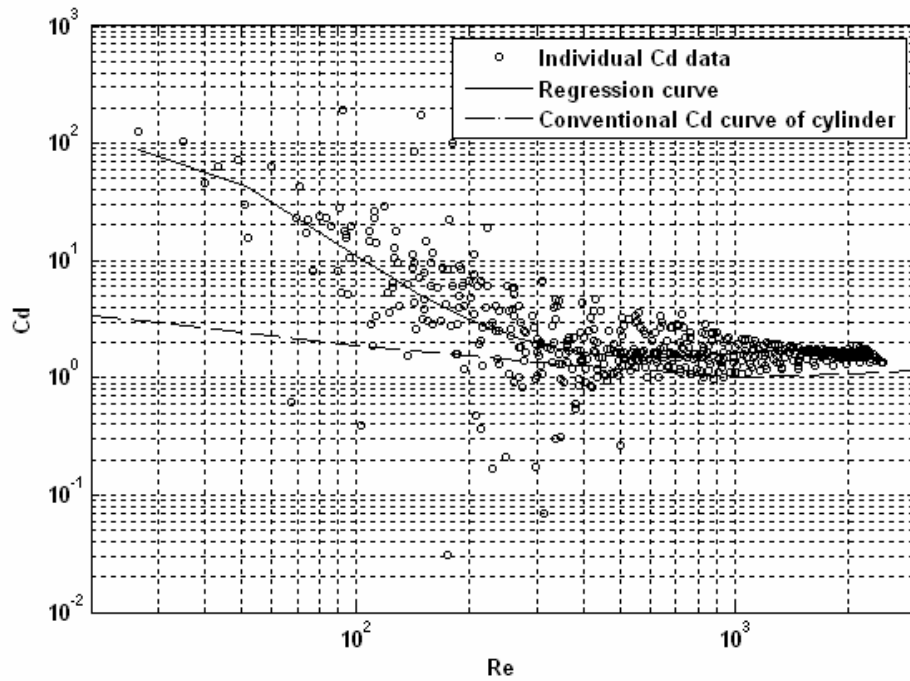
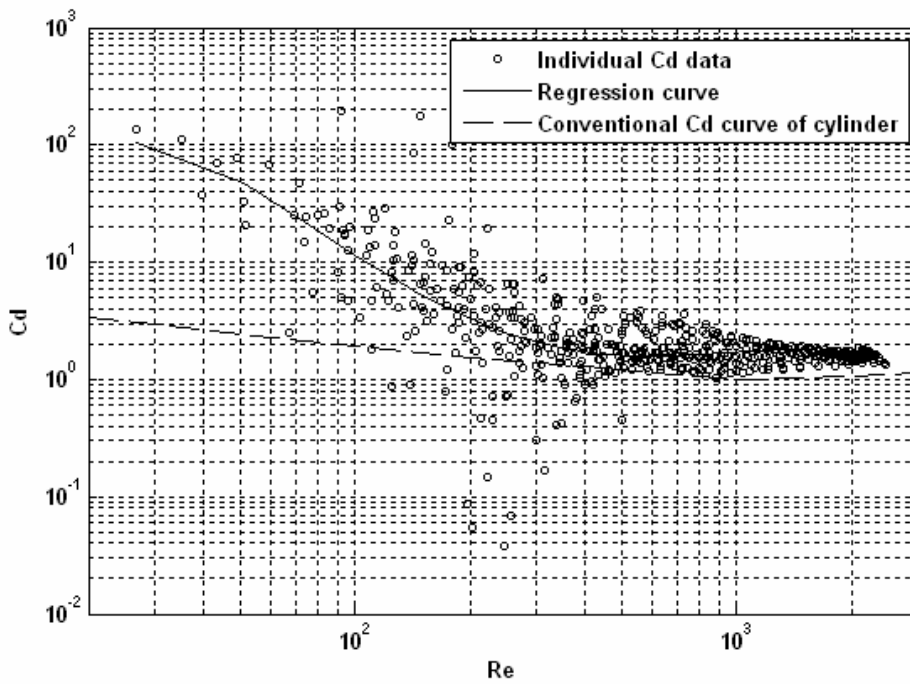**Figure 4.4 C_d versus Reynolds number for the big chain, assuming $C_m = 1$**

**Figure 4.5 C_d versus Reynolds number for the big chain, assuming $C_m = 2$**

4.3.2. Criteria for Improvement of Drag Force Data

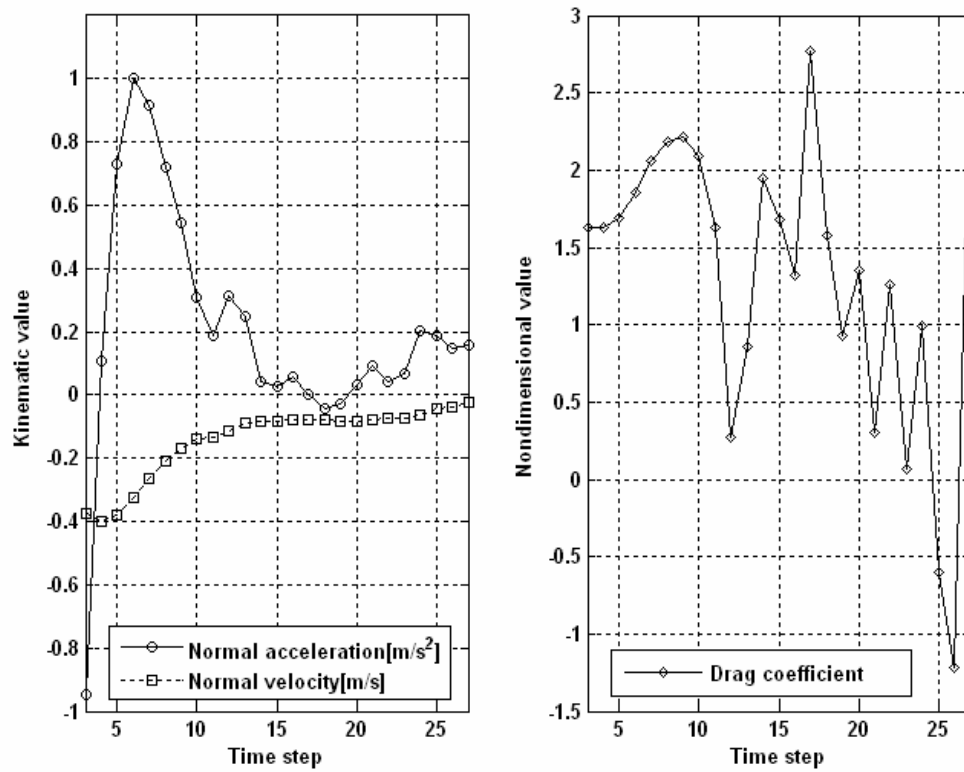**4.3.2.1. Ratio of Inertia to Drag Force**

Figure 4.6 illustrates an interesting relation between the drag coefficient and the ratio of the inertia force to the drag force, both of which have been plotted against the segment number for the chain.   The segments are numbered from the pivot end toward the free end.   The two curves are similar in shape; as the inertia to drag force ratio increases the drag coefficient also increases at a similar rate.   This might indicate that Morison's equation is not valid at inertia to drag force ratios larger than a certain value because in such case the Morison drag coefficients are characterized by the balance between drag and inertia force, not by the velocity.   This region is the so-called inertia dominant regime.   Also it is inferred that employing a constant added mass coefficient for the inertia dominant regime is not appropriate for modeling the line dynamics, even if the added mass doesn't have a significant contribution to the total force balance.

From the above observation it is concluded that not all data points in Figure 4.4 are reliable.   To remove the data points falling within the inertia dominant regime, only those points associated with an inertia to drag force ratio less than 1.0 were retained. However it was found that for inertia to drag force ratios around 1.0 (the so-called drag-inertia regime) inaccuracies in the determination of the acceleration caused scatter in the inferred inertia force, which in turn affected the inferred drag force.   From Figure 4.7 it is clearly observed that the derived drag coefficients oscillate with fluctuations of acceleration.   In other words, data with less scatter can be obtained in the drag dominant regime when the inertia to drag force ratio is of order 0.5 or less.
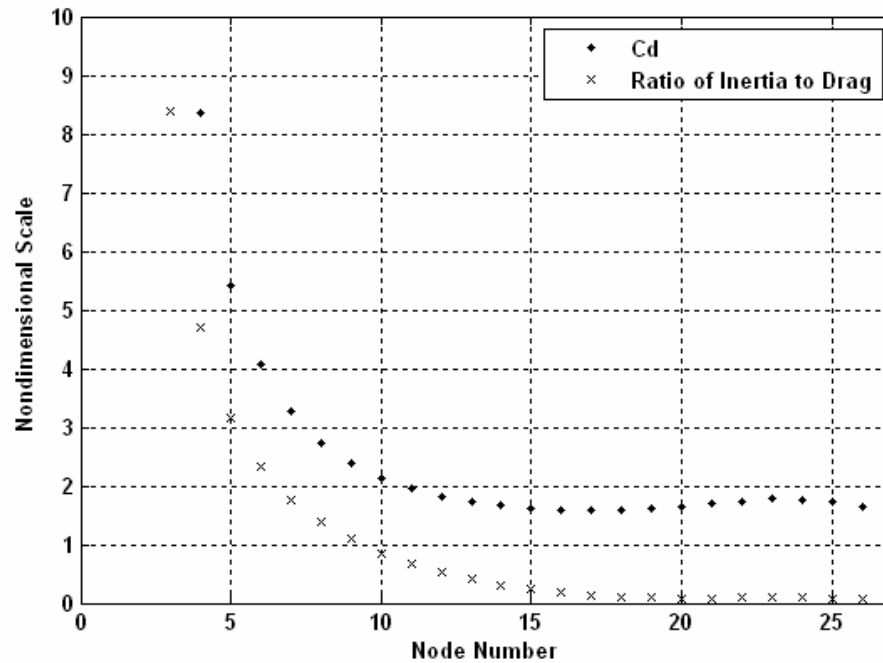
Figure 4.6   Relationship between C_d and the ratio of inertia to drag force for each

segment, assuming $C_m=1$

Figure 4.8 is the C_d vs Re curve obtained by considering only those points associated with an inertia to drag force ratio less than 0.5.   Unlike in Figure 4.4, in this case there is much less scatter in the data, especially at low Re.   The regression curve for the data and the conventional curve for a smooth circular cylinder show a similar trend over the tested range of Reynolds number even though there is small difference in magnitude (as expected for chain).   Consequently, the inertia-drag force ratio should be considered as a criterion to test the validity of extracted force coefficients, as well as for determining the validity of Morison's equation in the analysis of mooring line hydrodynamics.

Figure 4.7   Kinematics and drag coefficient of single node at mid section of chain
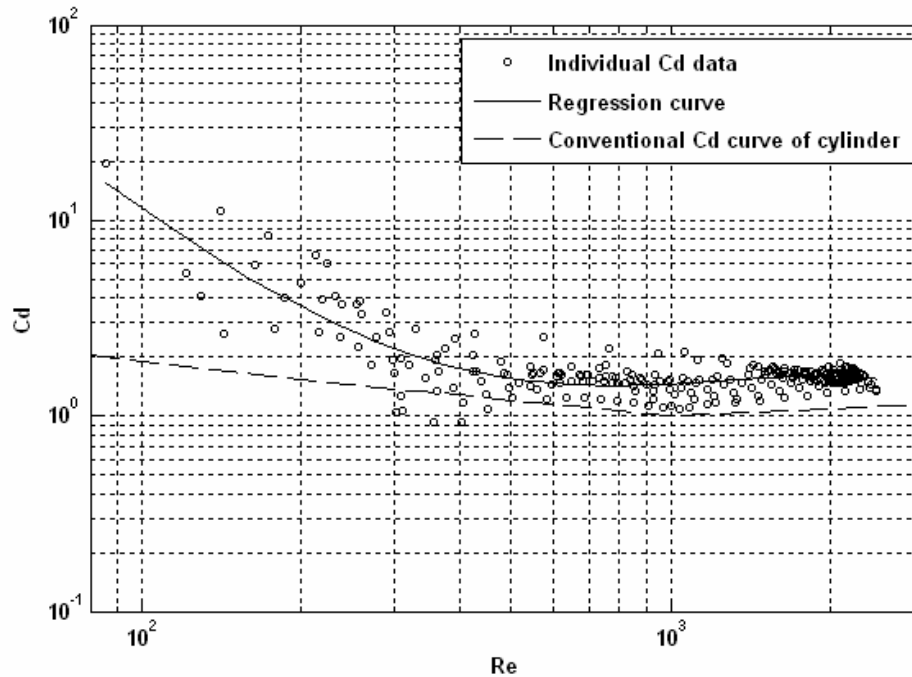
Figure 4.8 C_d versus Reynolds number for the ratio of inertia to drag force less

than 0.5, assuming C_m=1

4.3.2.2. Ratio of Tension to Drag Force

The motion of the upper section of the line close to the pivot point is mostly driven by the dynamics of the lower section.   This implies that the drag force on the upper segments is not only a function of the local normal velocity but also a function of the tension and hydrodynamic forces on the lower segments. And the drag force in the upper section of the line is usually much smaller than the other forces such as inertia, weight and tension.   For these reasons, it is difficult to resolve the drag force among the other

forces in the upper part of the line.

In solving the equation of motion using an explicit scheme, the tension at a given node is obtained from the previous segment and is used as a boundary condition for solving the force equilibrium for the next segment. The tension term seems to have a complex effect on the other dynamic forces. For the reasons mentioned above, a certain relation between tension and drag force could be taken as a criterion to filter out the drag coefficient data driven by the dynamics of lower sections of the line. This criterion is defined as the ratio of the contribution of tension in the normal direction to drag force, and results with a higher ratio than a selected threshold value will be filtered out.

The result of applying a threshold ratio of 1.0 is presented in Figure 4.9. Compared to Figure 4.4, the large values of C_d at low Re have been removed significantly while small C_d values which are mostly excluded in Figure 4.8 still remain. This indicates that the small C_d values might be the result of a distorted balance of hydrodynamic forces caused by low accuracy in determining the kinematics.

It therefore appears that combining two criteria (one for the inertia-drag force ratio and the other for the tension-drag force ratio) will provide a reasonable, mutually complimentary filter for the present drag force. The thresholds should be chosen carefully. Setting the thresholds of both ratios to values that are too small will result in loss of valuable information over the low Reynolds number range. Figure 4.10, provides the C_d vs Re results after applying threshold criteria of 0.5 for the inertia-drag force ratio and 1.0 for the tension-drag force ratio. Even though most of the data at low Re have been filtered out, a narrow band of data is observed for the range of Reynolds

number from about 300 to 1500. The scatter is considered within an acceptable range considering the drag coefficient is derived under an unsteady state condition in which the added mass coefficient might not always be equal to a constant value. To a certain extent the scatter is expected due to the assumption of constant added mass coefficient made at the outset.
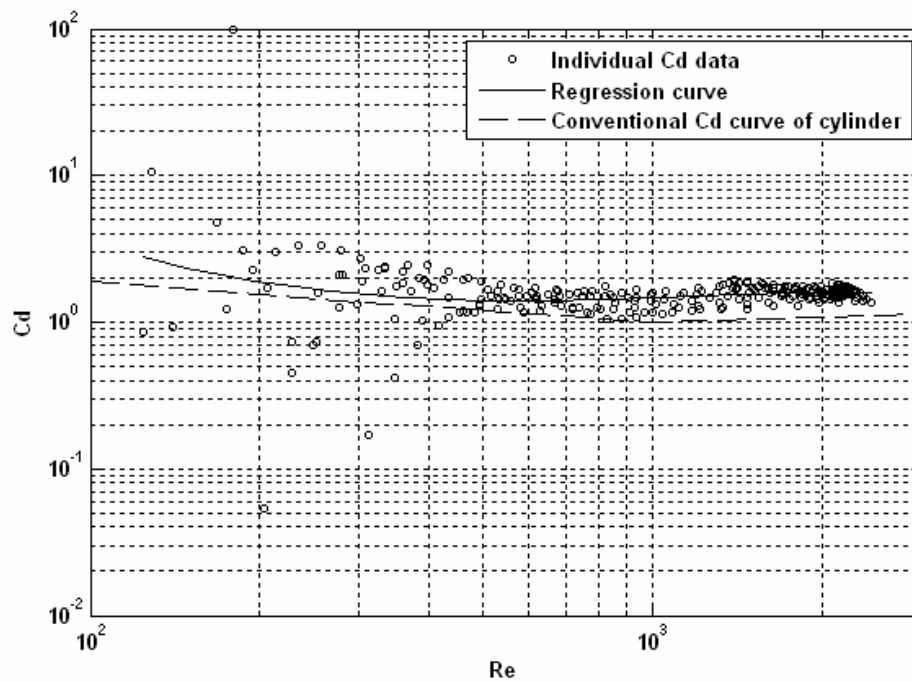
Figure 4.9 **C_d versus Reynolds number for the ratio of tension to drag force less than 1.0, assuming $C_m=1$**
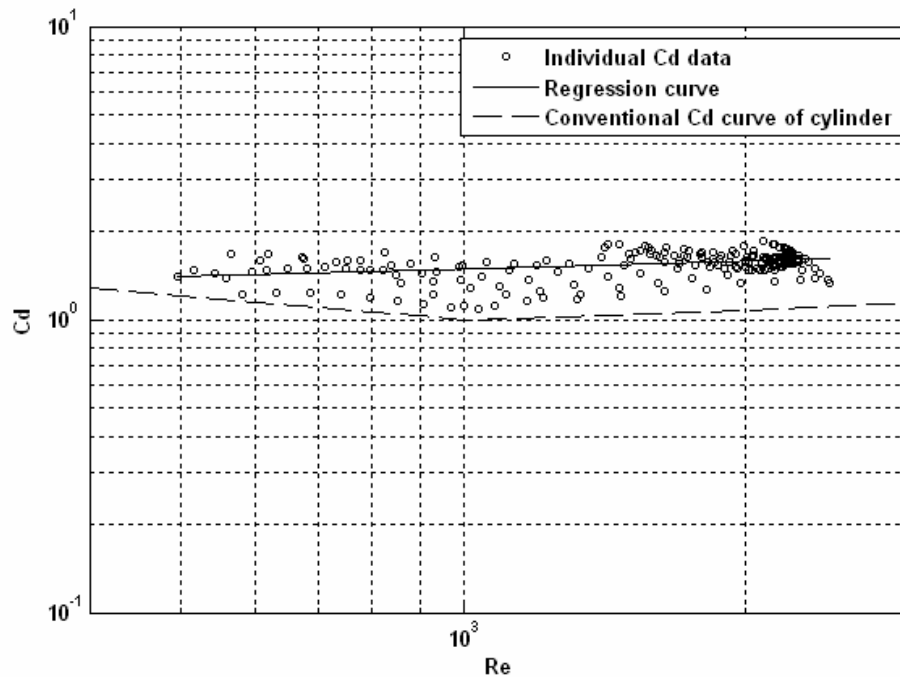
Figure 4.10 C_d versus Reynolds number for the ratio of inertia to drag force less

than 0.5 and the ratio of tension to drag force less than 1.0, assuming $C_m=1$

4.3.2.3. Angle Versus Reynolds Number

The criteria developed above may be used to filter out unreliable data on the basis of line dynamics.   Here an intuitively derived criterion is introduced which aims to filter out data subject to large experimental errors.   There are two kinds of errors that can be considered: one is node extraction error from the image which propagates into errors in the derived kinematics, and the other is accumulated error in the tension term when solving the equation of motion from the free end to the pivot end.   Both types of errors

are significant in the low Reynolds number region corresponding to the upper section of the line. In the area associated with very small kinematics, the node extraction and accumulated tension errors might be larger than the kinematics themselves.

In order to remove the highly contaminated results, one specifies a certain Reynolds number threshold at each angle of the line (i.e. each time step) in its sequence of falling motion. This is determined by checking the acceleration and velocity profile with the drag coefficients at each time step of free oscillation to see if there are any abrupt changes. Once the first node point with an abrupt change in the magnitude of the drag coefficient has been identified, then the Reynolds number corresponding to that node and time step is set as the lower limit. For Reynolds numbers below these threshold values, all of the associated drag coefficients are discarded.

Figure 4.11 displays the upper boundary of the trust zone for each time step (angle). The drag coefficients obtained from the node points below the solid line are considered as less contaminated by error. In the middle of the graph, a lower boundary is observed which seems to be caused by acceleration fluctuation over the chain from the free end to the pivot end. Typically for this area (angle range), the maximum Reynolds number threshold is about 450, unlike other areas (angle ranges) where the maximum Reynolds number threshold is around 200 to 300.
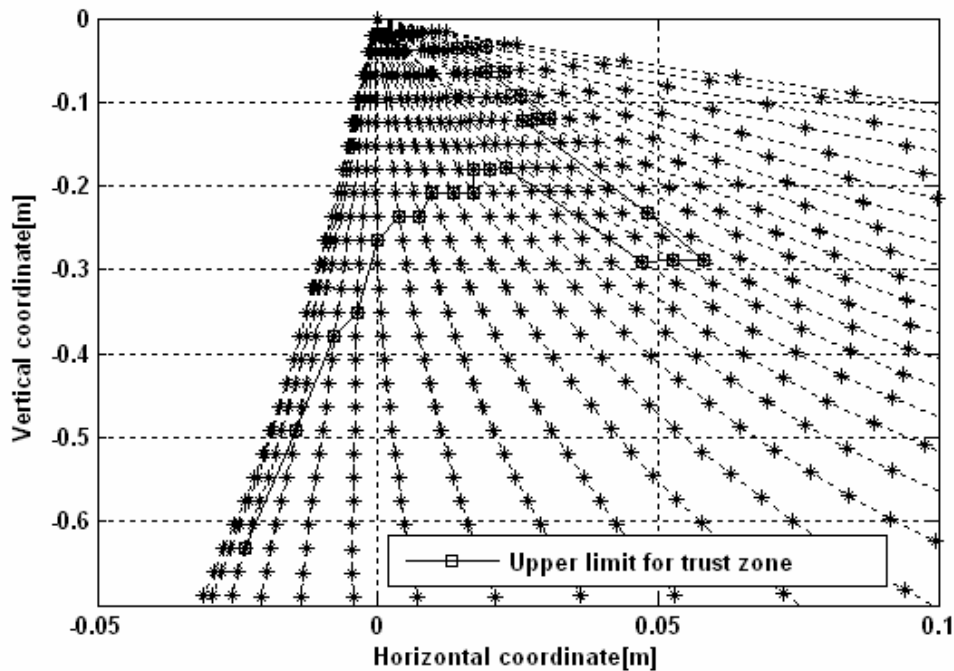
Figure 4.11   Trust region of analysis for experimental data

To investigate how the errors accumulate when moving up the chain, the data analysis procedures were applied to an equivalent data set generated by numerically simulating the free oscillation test using OrcaFlex.   In the simulation the drag coefficient was set to 1.2 for the full Reynolds number range.   The backward analysis of the simulation data results in inferred drag coefficient values that are slightly scattered around 1.2.   This means that there are some errors in obtaining the kinematics from position data.   This may in part be due to the formulation of line dynamics in OrcaFlex being different than the dynamic formulation employed in this analysis, which would cause inconsistencies between the forward simulation and the backward analysis.

However the kinematic error is considered to be more significant because it is coherently observed in the analysis of the experimental data.

The trust region boundary for the simulation data shown in Figure 4.12 was determined by drag coefficients that are bigger or smaller by 0.5 than the input value of 1.2. The reason for applying different filtering criteria for the experimental and numerical data is because the characteristics of two data sets are not equal: one is based on real motion and the other is artificially created. The two plots (Figure 4.11 and Figure 4.12) exhibit a similar trust region boundary, which has a relatively high Reynolds number threshold for the middle the stage of motion. Therefore it can be inferred that the intuitively chosen trust zone looks reasonable for identifying data distorted by experimental error.

The filtered experimental data (i.e. data falling within the trust zone) are plotted as C_d versus Re in Figure 4.13. Some of the data scatter at low Re is still retained, however the overall trend of the data appears to be unbiased. By comparing Figure 4.13 with Figure 4.10, it is noticed that many of the scattered data are associated with common errors related to both the dynamic analysis and experimental techniques used in the present study. Thus, applying any of the criteria (inertia-drag ratio, or tension-drag ratio, or intuitive Re) would be sufficient to isolate the results considered to be in error no matter whether the errors are associated with experimental or numerical deficiencies. However in the subsequent analyses of the free oscillation tests, the data have been filtered by applying the inertia-drag ratio and tension-drag ratio criteria, not the intuitive Re criterion.
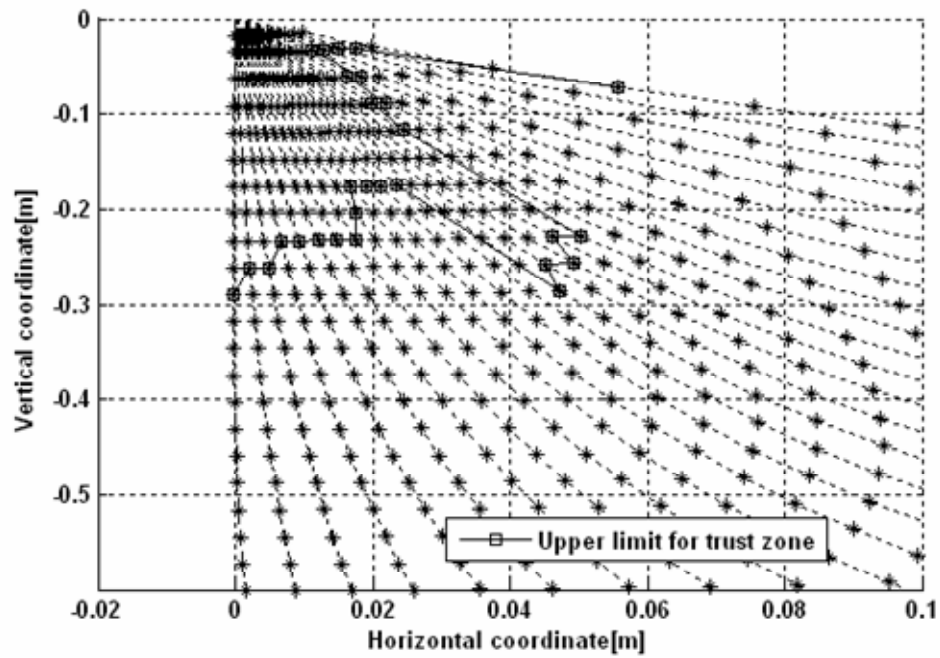
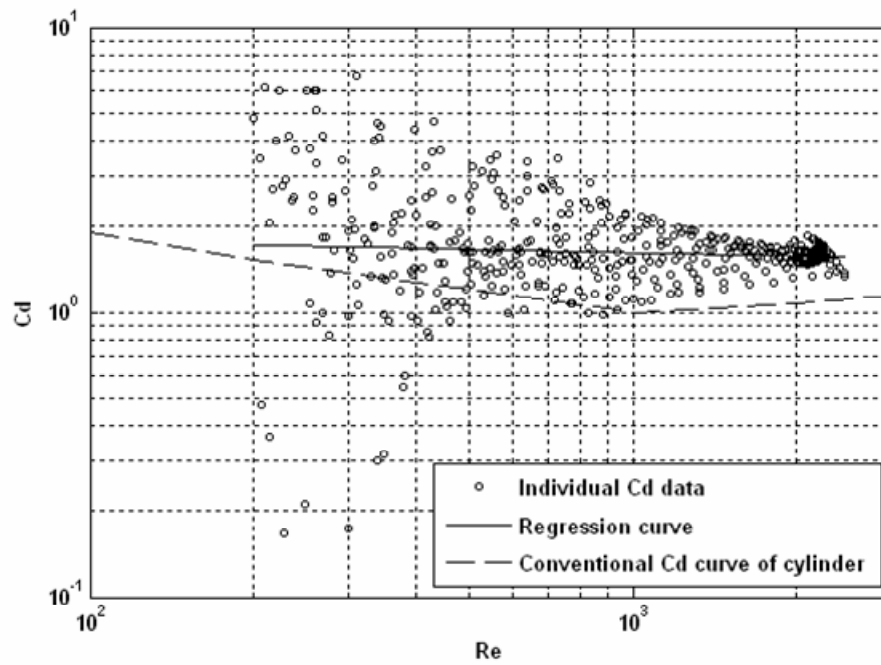**Figure 4.12   Trust region of analysis for simulation data**

Figure 4.13 C_d versus Reynolds number after filtering with intuitional criteria,

assuming $C_m=1$

4.3.3. Results of Small Scale Experiments

The detailed procedures for extracting and filtering the instantaneous values of drag coefficient from the free oscillation tests have been explained. Using these procedures, all the measured data of various sizes of chain were processed to determine the correlation between drag coefficient and Reynolds number. The actual sampling rate of optical tracking was 150 Hz, but in order to reduce the error associated with velocity and acceleration the sampling rate was reduced to 15 Hz by decimation. Since there was significant overlap in Reynolds number with the data sampled at 150 Hz, the factor of 10 reduction did not affect the scope of the data much. The inertia-to-drag force and tension-to-drag force filtering criteria were applied instead of the intuitive criteria discussed in the previous section, because the former are more objective and easy to justify from an engineering perspective.

Each experiment was conducted three times for each test chain. Instead of averaging the derived coefficients, individual results from all the repeated data are plotted on an arithmetic scale in Figure 4.14 to Figure 4.16. The overall trend is for the drag coefficient to increase gradually with increasing Reynolds number, for the Re range represented by the tests. The narrow band of scatter in the data is due to fluctuation of the inertia force and unintended transverse motion of the chain. The fluctuation of the inertia force can be a real hydrodynamic phenomenon and it can also be due to inaccuracy in numerical computation of the acceleration. The transverse motion is mainly created by lift force on the chain during the initial stage of falling right after release and its magnitude seems to increase with decreasing weight of chain, although

exact lift forces are not determined quantitatively. Consequently the band width of the scatter in the drag coefficient tends to increase with decreasing chain size: approximately 0.5 to 1.1 for big to small chain.

Particularly in the results for the small chain, one additional narrow band of scatter with relatively small values of drag coefficients is observed at Reynolds numbers ranging from 500 to 1700. The data points in this band are from the first two segments from the free end of the chain. These low tension sections of chain experience severe transverse and torsional motions, which results in abnormal behavior of the kinematics, especially the acceleration, compared to that of neighboring sections. This end-effect occurs in all chain sizes, but the impact on the inferred drag coefficient is only noticeable in the results for the small chain. This means that as the chain gets larger and heavier, the influence of the transverse force is diluted by the influence of the other applied forces, such as the weight and the in-line hydrodynamic force. Thus, the results from the larger size chain can be considered more accurate and reliable.

In Figure 4.17, drag coefficients from all sizes of chain are included. Since the chains used for the small scale tests have a similar twisted shape for the different sizes, coherence of the results between the three chains should be maintained. Even though there are slight differences in the slope of the regression curve for the plots for each individual chain and all chains lumped together, all data are forming a shape of data scatter that is consistently connected, with a tendency that is similar to those observed in the three individual plots. Also, the representative correlation curve is considered to adequately follow the trend of each individual case.
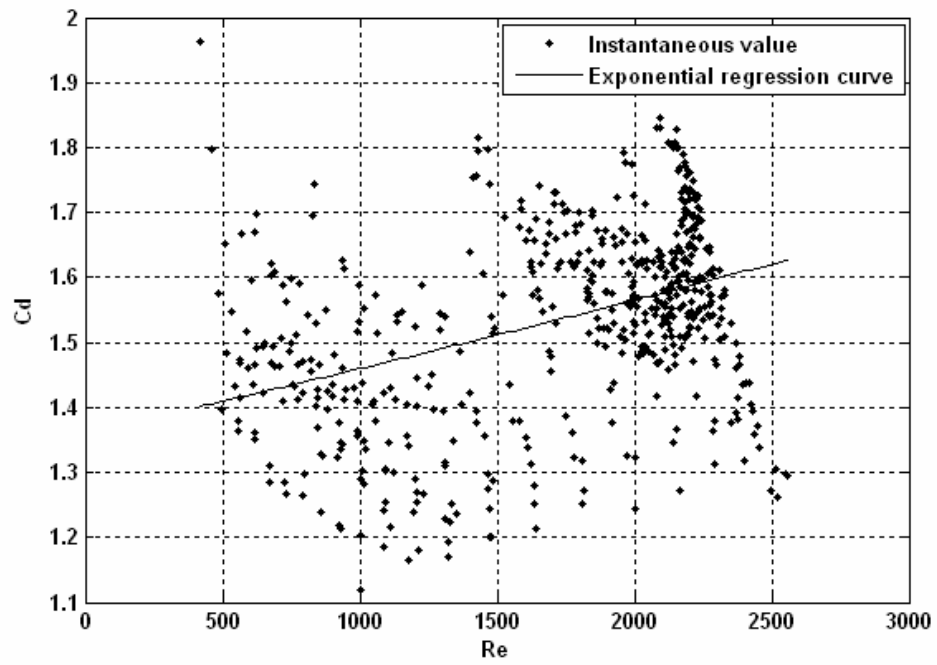
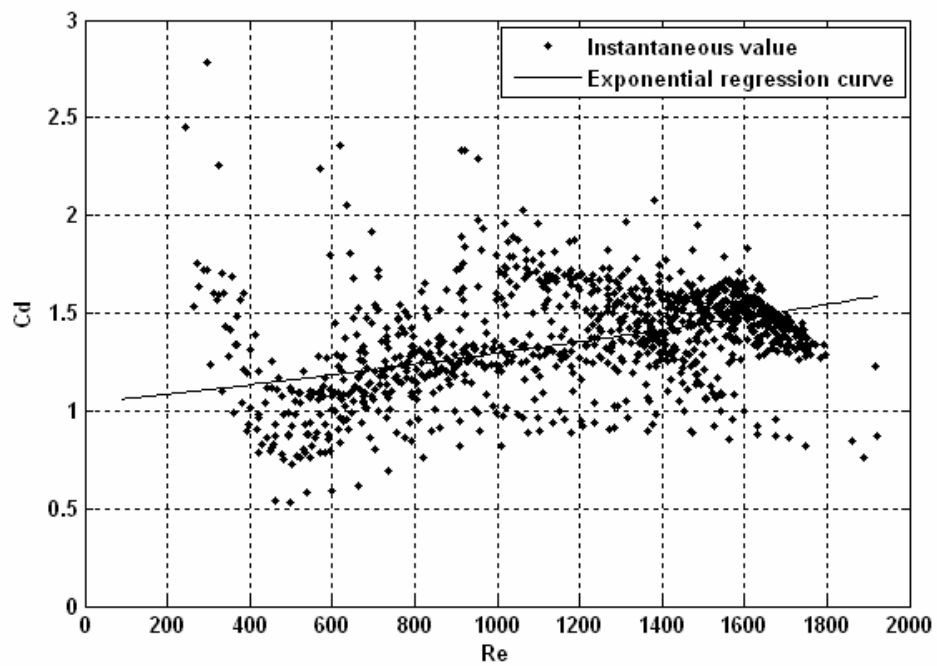**Figure 4.14   Drag coefficients for big chain (diameter: 4.8mm)**

Figure 4.15   Drag coefficients for medium chain (diameter: 4.1mm)
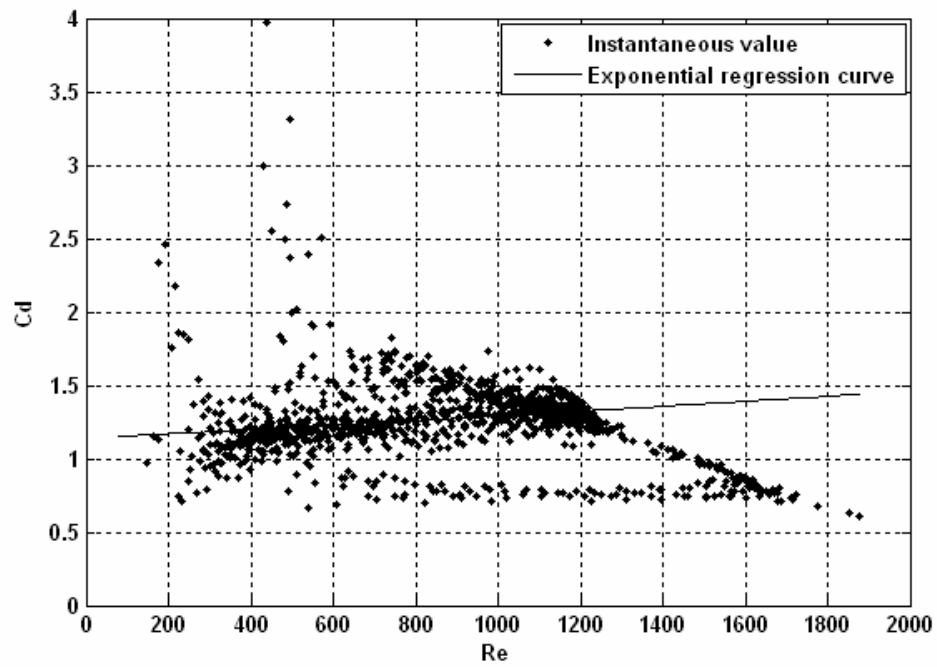
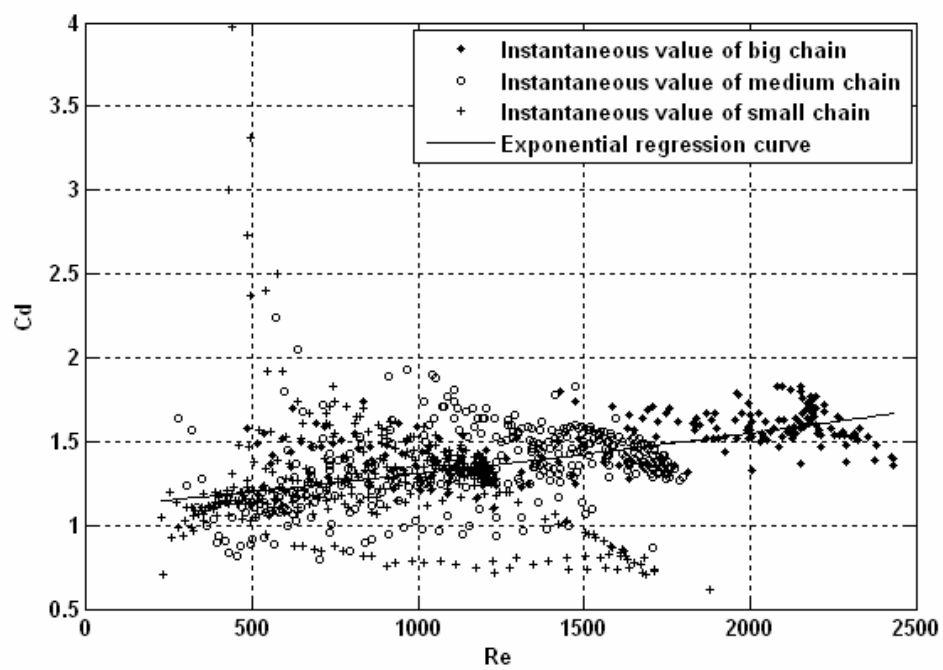**Figure 4.16   Drag coefficients for small chain (diameter: 3.4mm)**

Figure 4.17   Drag coefficients for all chain in small scale test

### 4.3.4. Results of Large Scale Experiments

The analysis procedures for the large scale experimental data are identical to those for the small scale data since all the conditions are the same except for the line size, shape and length. At large scale another accuracy issue arises from optical tracking because the degree of image distortion is comparatively larger. The result is that uncertainty in the position data, and the derived velocity and acceleration, increases significantly. The acceleration profiles show a white noise pattern, which can induce large error in the extraction of drag coefficients due to the distorted balance of hydrodynamic forces. Thus, applying a digital filter to the position vector at each node is essential to obtain smooth and reasonable profiles of kinematics, as illustrated in Figure 4.18.

As for the small scale tests, tests for big, medium and small size of chain were repeated three times, but only the small and big chain data were analyzed due to imperfections in the image data for the medium size chain. More severe scatter and bias in the drag coefficient data is observed since additional error involved with optical tracking is weighting on the pre-existing experimental and analysis errors suggested and discussed in previous sections. For filtering of these errors, both inertia-drag ratio and tension-drag ratio of unity (=1) are employed and the results are given in Figure 4.19 and Figure 4.20.

As discussed for the small scale experiments, wider scatter is observed in the small chain results due to the bigger transverse motion end-effect. It is observed that the trend for each of the two data sets (small and large chain) is different: one regression

curve is inclined while the other is declined with respect to increasing Reynolds number. This might be explained by the difference in the shape of each chain. They are both plain type in shape but different in the ratio of length-to-width of the links: the big chain has a standard ratio but the small chain has an elongated length. Nevertheless the data from both chains show good agreement at Reynolds number of 4000~6000. Thus, these two sets of results have been combined in Figure 4.21 to provide data for a wide range of Reynolds number. Since all repeated tests for each size of chain indicated similar results, a single data set for each chain size has been plotted in Figure 4.21.
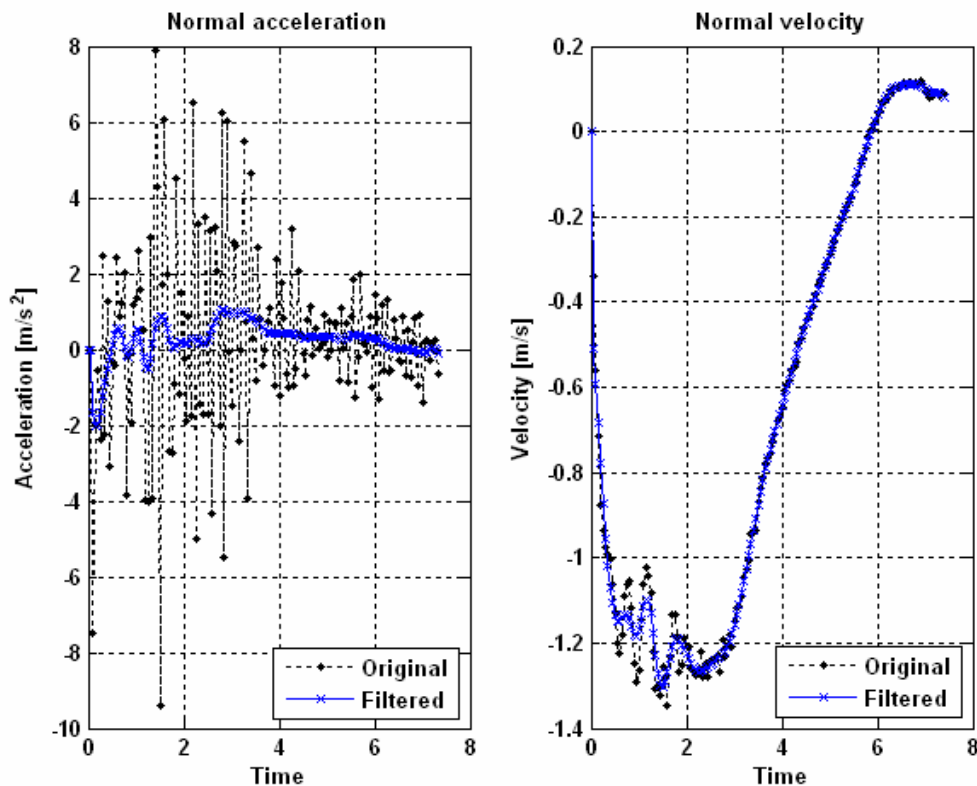
Figure 4.18   Profile of kinematics in normal direction at arbitrary single node
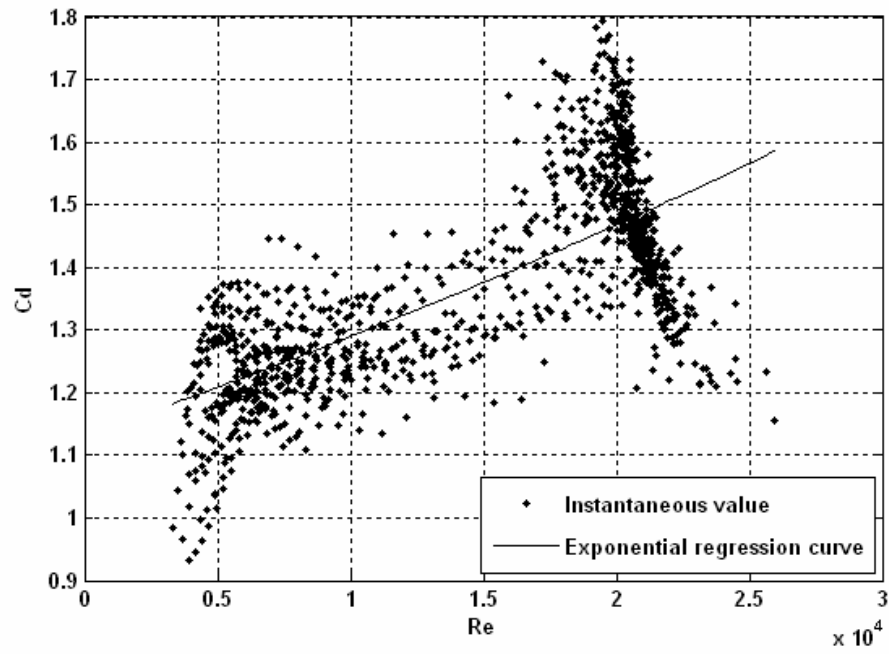
Figure 4.19   Drag coefficients for big chain (diameter: 1.954 cm) in large scale test
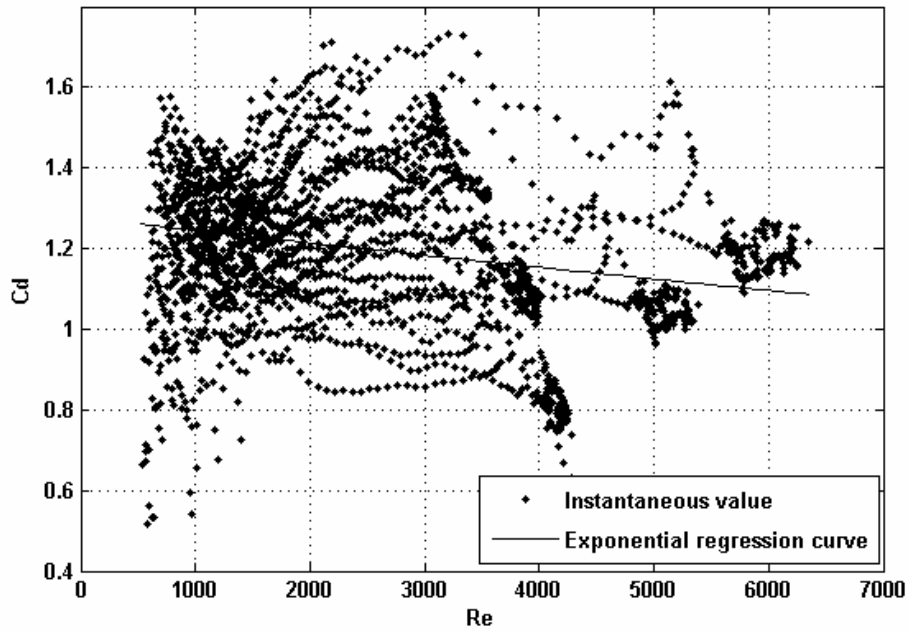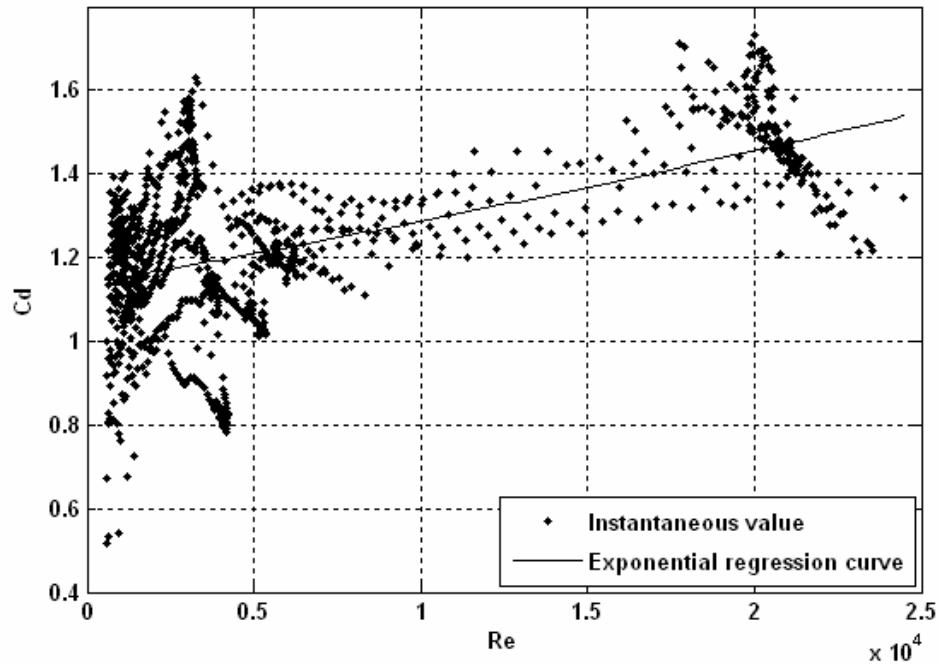

Figure 4.20   Drag coefficients for small chain (diameter: 0.584 cm) in large scale

test

Figure 4.21   Drag coefficients for all chains in large scale test

4.4. Forced Oscillation Tests

4.4.1. Fourier and Time Averaged Coefficients

As opposed to the free oscillation case, for the forced oscillation tests the mooring line was anchored at the bottom and the top was forced to move in a prescribed unidirectional harmonic motion consisting of one or two frequency components.   The nonlinear response of the mooring line could be comprised of many frequency components.   The total hydrodynamic force acting on each section of the line also can be decomposed into individual components with corresponding frequencies because it is

purely motion-dependent. Converting the hydrodynamic force time series into frequency components by Fourier transform enables the extraction of both drag and added mass coefficients.

The hydrodynamic force is obtained by solving the equation of motion in a similar manner as for the free oscillation case with the exception that the measured top tension is applied as a boundary condition at each time step. The resulting force coefficients can be time- or frequency-averaged values according to the methods of analysis explained in section 2.6. These averaged values are expected to be more reasonable than the instantaneous ones obtained from free oscillation tests for the following reasons: no assumption is made for the added mass force and errors associated with kinematics may be reduced by the averaging process.

Due to the similar trends of the estimated coefficients for the three different-sized chains and wires tested, only the results of the "big" size mooring are discussed in this chapter. All other corresponding results for the other chain and wire sizes are presented in the Appendix A.

Even though the motions of the mooring line consist of various harmonics, only harmonics with the frequencies of the forced oscillation are considered for the estimation of Fourier averaged values. This is because the magnitudes of the harmonics for frequencies other than the forcing frequency are in general much smaller and those small quantities may not be resolvable with sufficient accuracy even by the averaging process. On the other hand, those small frequency components are taken into account when determining time-averaged coefficients (as opposed to frequency-averaged coefficients).

Occasionally it is observed that a dominant harmonic in the total hydrodynamic force

is not aligned with the forcing frequency. In such a case, the resulting coefficients show unrealistic and unreasonable values when compared to other coefficients determined at similar Keulegan-Carpenter or Reynolds number. This indicates that the measured motion of the line might be significantly distorted by errors arising from either optical tracking or the filtering procedure, or both. Thus, results from any other frequency than the forcing frequency are not acceptable.

With Fourier analysis the Reynolds number (Re) does not appropriately represent the hydrodynamics of the oscillating mooring line because it only characterizes the amplitude of the velocity, not the frequency. Thus, even though the line could be oscillated at various frequencies but with amplitudes that result in identical characteristic velocities, scaling with the Reynolds number could not distinguish between these cases. To better distinguish the effect of the oscillation frequency, the Morison coefficients obtained from the forced oscillation tests will be plotted against the Keulegan-Carpenter number

In Figure 4.22, the Fourier-averaged results from five different oscillation tests of a single chain are given as function of the Keulegan-Carpenter number. As can be seen, there exists a certain relation between the drag and added mass coefficients; rapid increase of C_m corresponds to large decrease of C_d, with negative-valued coefficients occasionally being indicated. This trend is commonly observed but not so obvious when the level of variation in magnitude is moderate. The occurrence of negative-valued coefficients is attributed partially to the Fourier averaging process and inaccuracy of the derived kinematics. The added mass coefficient shows especially large negative values and this mostly stems from large errors in the derived acceleration.
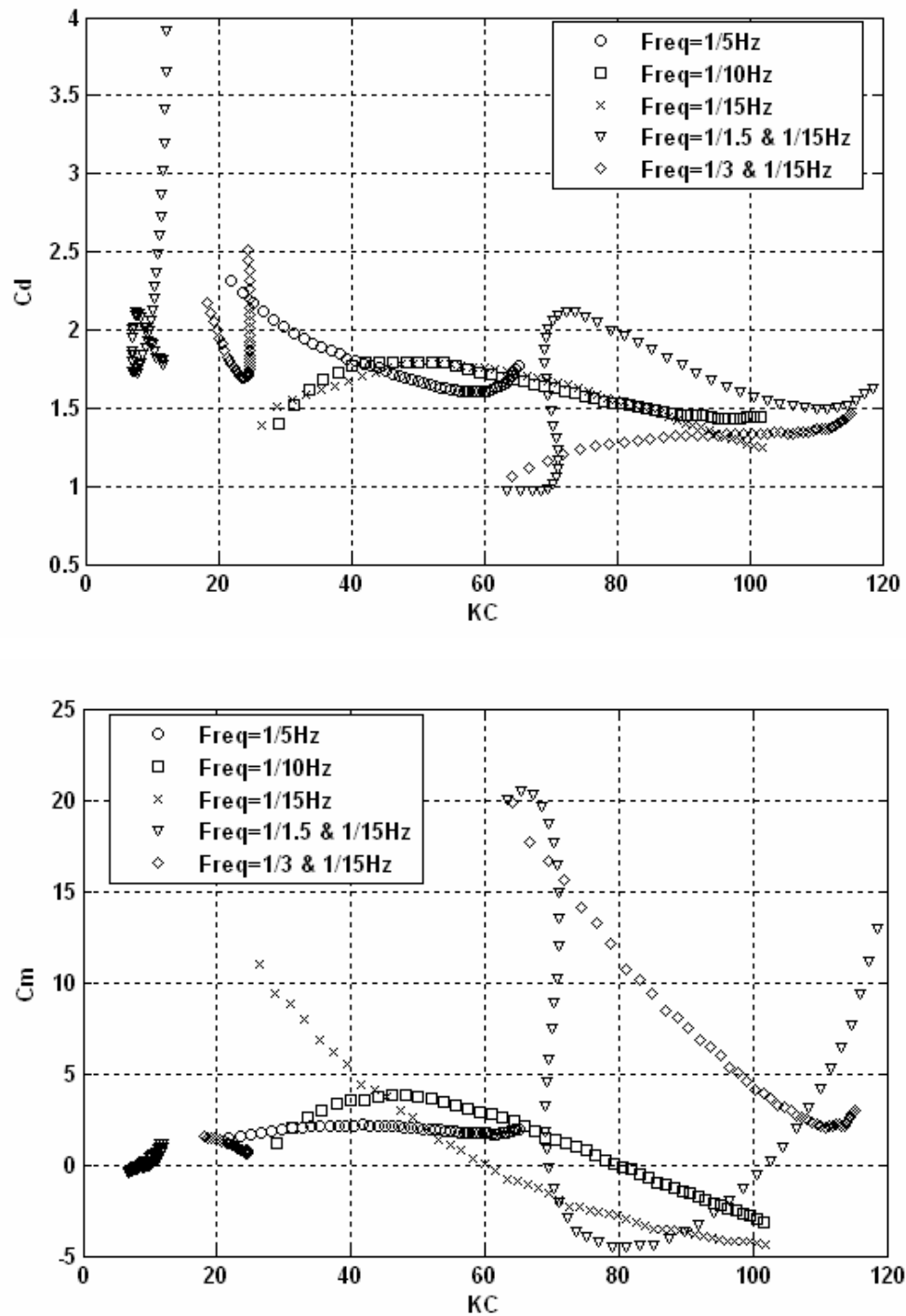
Figure 4.22　**Fourier-averaged drag and added mass coefficient of chain (diameter:**

1.954 cm) with semi-taut catenary configuration

The effect of Fourier averaging is clearly explained from the drag coefficient results for the 1/1.5 Hz and 1/15 Hz combined frequency test shown in Figure 4.22. Coefficients at low KC (0~20) increase above a level around 2.0 while those at high KC (60~80) decrease below 2.0 by a similar amount, which indicates that the balance between all individual force components is maintained by reciprocal variation. This also can be seen in the added mass results but it is not quite as clear for the drag coefficient.

As exhibited in the variation with KC in Figure 4.22, significant inconsistency between the five different frequency tests is observed in the results for both Morison coefficients.   At first sight this might be regarded as the influence of measurement error but apparent inconsistencies can also arise from the following factors:

1. Reynolds number effects, which are different for the five different test conditions, and

2. the possible fluid-induced transverse oscillation which is not taken into account in the present analysis.

Figure 4.22 shows that at KC number less than 20 the drag coefficient increases dramatically while the added mass shows a gradual decrease.   Data in this range of KC correspond to the high frequency motion in the combined low-high frequency forced oscillation test.   A mooring line undergoing combined frequency forced oscillation is expected to experience both in-plane and transverse (out-of-plane) oscillations of small amplitude due to wake reversal as the line returns back into its pre-induced wake zone, leading to anomalous pressure gradients.   Thus, in this case the variation in drag coefficient at low KC is considered to be mostly affected by small fluctuating motions

which are scarcely resolved by optical tracking with a field of view as large as that employed in this experiment.

As discussed above, Fourier averaging, unidentified small vibrations, and experimental error can be the source of variations or abnormal trends in the force coefficients. In addition to these factors, a biased ratio of inertia to drag force is also associated with such variations, which was investigated in the analysis of the free oscillation tests. For instance, in the drag dominant regime the added mass coefficient is more variable, while in the inertia dominant regime the drag coefficient is more variable. When this is superimposed with uncertainty of the experimental determination of kinematic values, the degree of fluctuation in the force coefficient intensifies severely. Thus, it is inferred that employing Morison's equation to any hydrodynamic regime does not always guarantee a reliable consequence.

Figure 4.23 corresponds to Figure 4.22 except that in this case the Morison force coefficients have been determined by time averaging. Here the expected trend of one coefficient increasing while the other decreases is not as readily apparent. From the results of the 1/10 Hz and 1/15 Hz single frequency tests, it is recognized that inaccuracy in determining the acceleration in single low frequency oscillation could not be readily recovered by time averaging but, in conjunction with high frequency motion, significant reduction of error is achieved. Compared to the results of harmonic-averaging, overall the drag coefficient results seem to vary with KC in a more consistent manner, except for some of the data associated with small amplitude motion at low frequency (which corresponds to the motion of sections of the line near the anchor point). However, this consistency is not retained in the added mass coefficient results due to the relatively

large uncertainty of determining the local acceleration of the line.
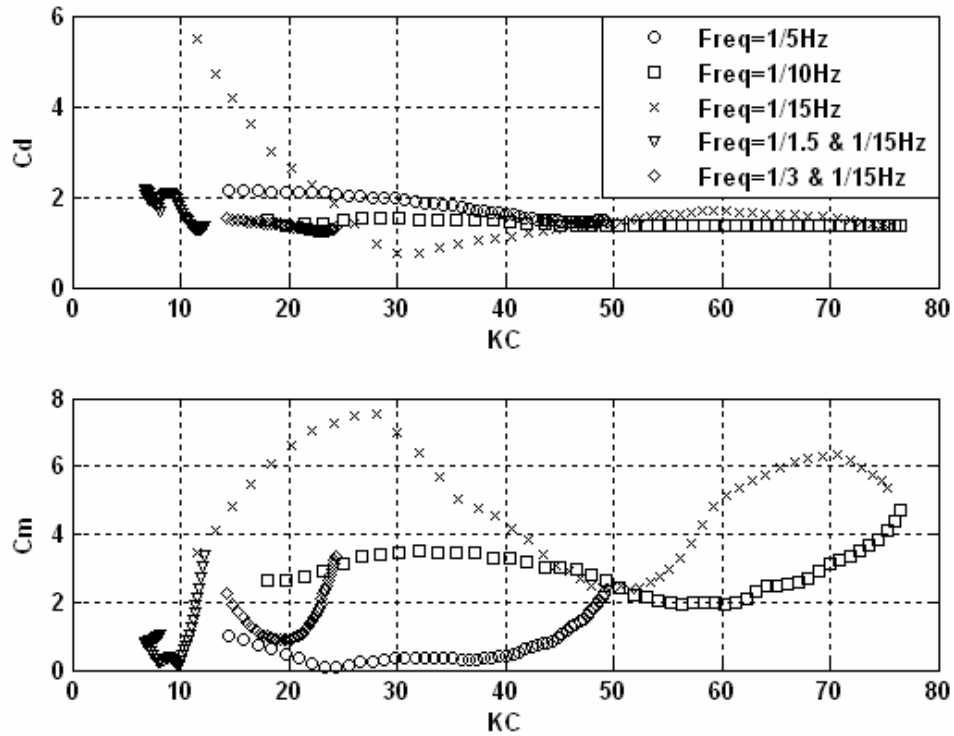
Figure 4.23   Time-averaged drag and added mass coefficient of chain (diameter:

1.954 cm) with semi-taut catenary configuration

As stated, two different configurations of mooring line were tested (semi-taut catenary and suspended catenary) to explore the seabed effect on the hydrodynamic behavior.   Rather large variation of the Morison coefficients at high KC is observed in the results for the suspended catenary mooring (Figure 4.24), where high KC indicates the motion of the upper section of the mooring line.   Since the motion of the line near

the anchor is slow (low KC), contact with the seabed does not seem to have a significant influence on the hydrodynamics of the mooring line.

The abnormal hydrodynamic coefficients from the upper part of the line may be due to a higher degree of transverse oscillations being present in the suspended line compared to the semi-taut line. Or, when the dominant frequency of motion is close to one of natural frequencies of the mooring line, as may have occurred with the combined 1/1.5 Hz + 1/15 Hz forcing, possible resonant motion at a certain section of the line can occur, which might give rise to abnormal hydrodynamic behavior. The bottom part of the suspended mooring is less constrained to transverse motion than that of the semi-taut mooring and tension variations associated with transverse motions may be present in the measured top tension. Tension information that is inconsistent with 2D motions may give rise to large variation of the coefficients at the initial stage of the calculation, as the explicit computation proceeds from the top to the bottom of the mooring line and the degree of 3-D effect in tension decreases. Except for the anomalous behavior at high KC, most of the trends and characteristics in the force coefficients for the suspended catenary mooring test appear to be similar to those shown for the case of a semi-taut catenary mooring.
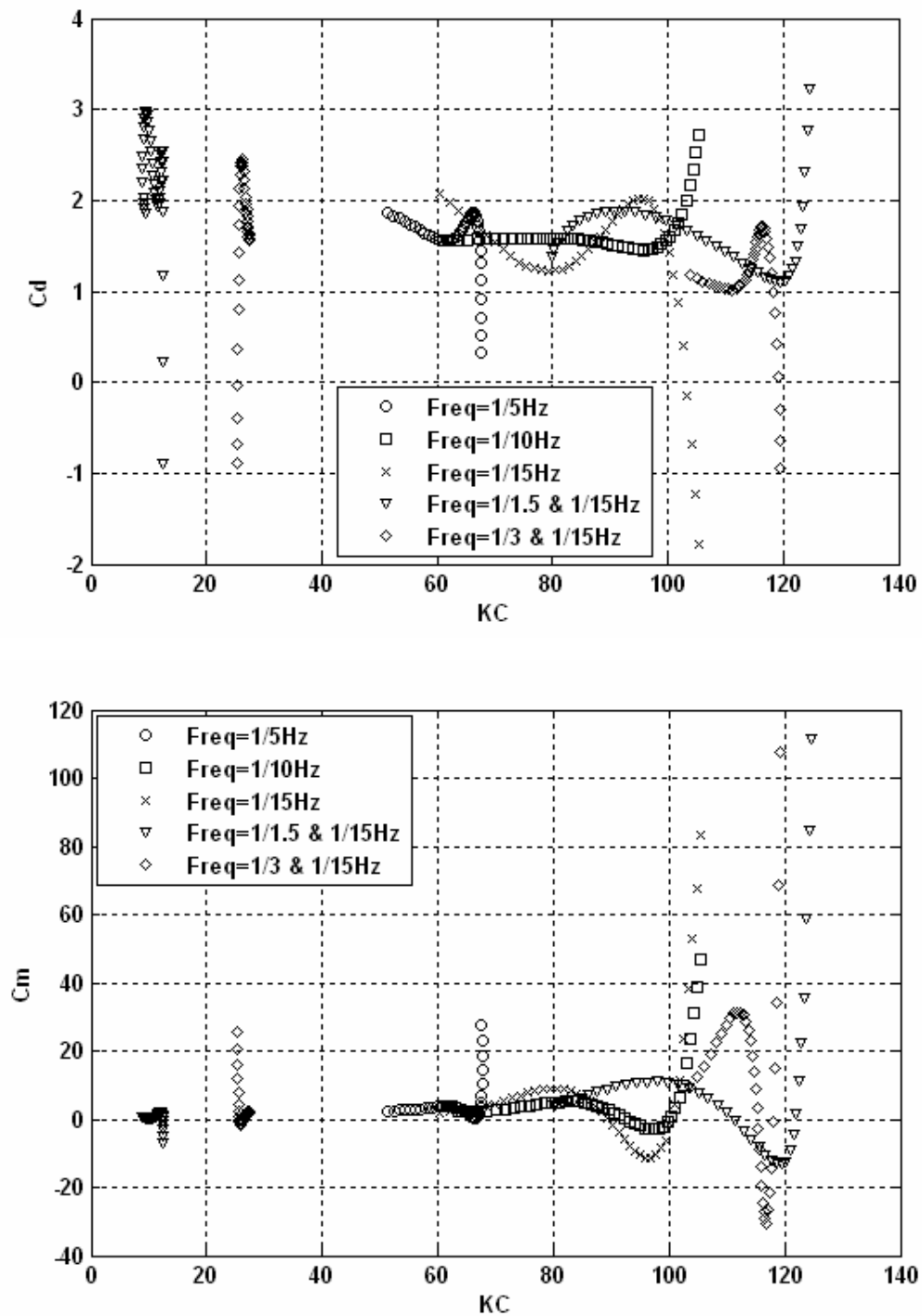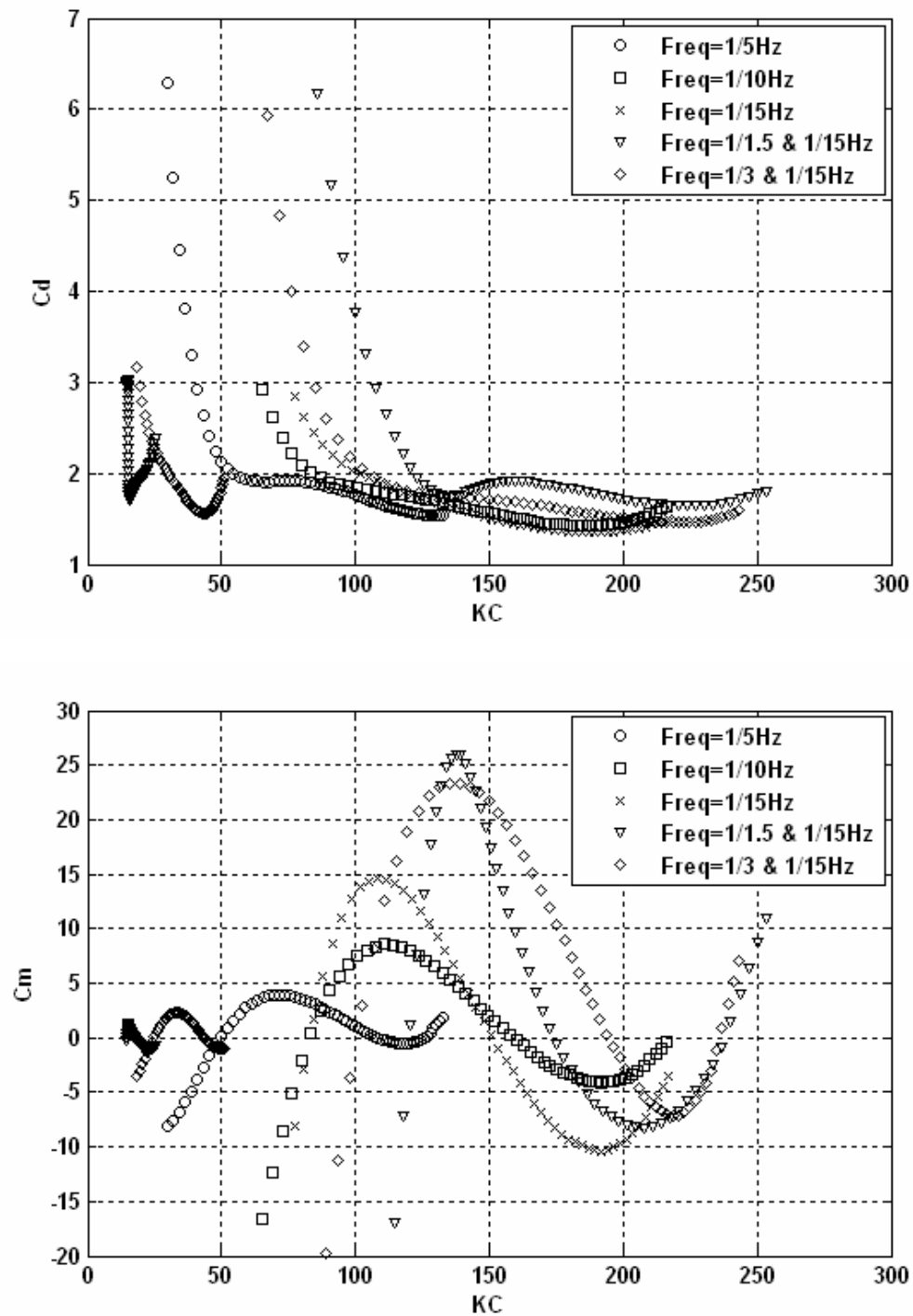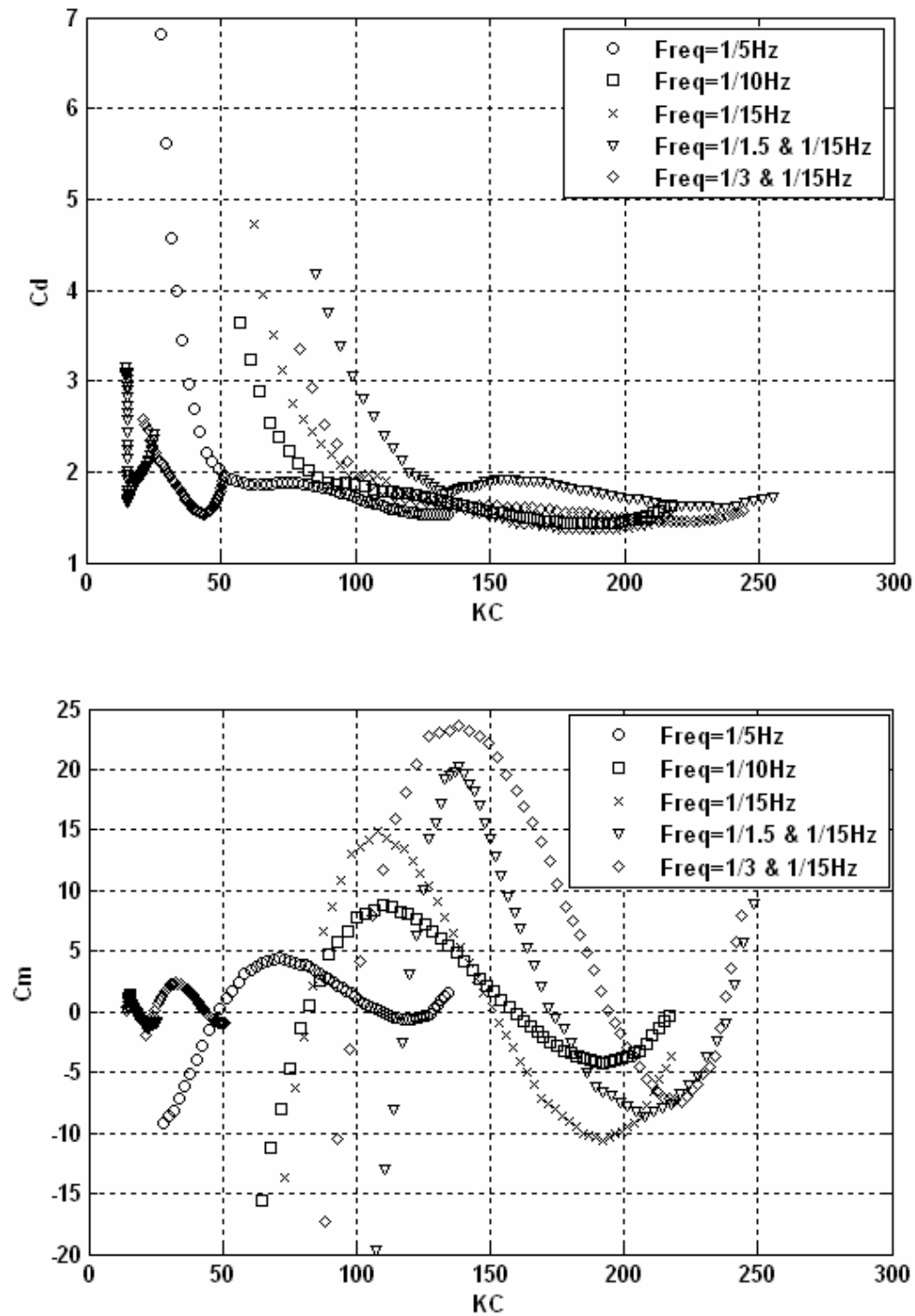
Figure 4.24   Fourier-averaged drag and added mass coefficient of chain (diameter: 1.954 cm) with suspended catenary configuration

Results for the big size wire without considering bending stiffness are shown in Figure 4.25. The bending stiffness of wire tested in this study was small enough to be neglected in the dynamic computation because the hydrodynamic results from the finite bending stiffness (EI = 0.1 N-m^2) (Figure 4.26) and no-bending stiffness (Figure 4.25) conditions show no remarkable difference. As shown in the chain tests, the drag coefficients are confined to a rather narrow band whereas the added mass coefficients display a large variation with KC. However, the degree of added mass variation in the wire results is larger than for the chain results, which can be attributed to the fact that a slackened wire may undergo relatively large transverse motion due to twisting and bending. Thus, the variation of the added mass seems to be mostly attributed to the kinematic error arising from measurement and to material properties (torsional and bending stiffness).

At low KC, the drag coefficient increases as the added mass coefficient decreases dramatically. This usually occurs in the inertia dominant regime where the magnitude of both the velocity and acceleration is relatively small so that even tiny errors in the kinematics can distort both hydrodynamic coefficients. In the drag dominant regime the drag coefficients seem to be reasonable while the added mass coefficients exhibit a large variation. Thus, it can be inferred that the variation of the added mass coefficient at low KC is mainly affected by experimental error and the variation at high KC is driven by both experimental error and the fact that the Morison equation is reliable only in the drag-inertia regime.

Figure 4.25   Fourier-averaged drag and added mass coefficient of wire (diameter: 0.915 cm) with semi-taut catenary configuration

Figure 4.26   Fourier-averaged drag and added mass coefficient of wire (diameter:

0.915 cm) with semi-taut catenary configuration in consideration of EI=0.1
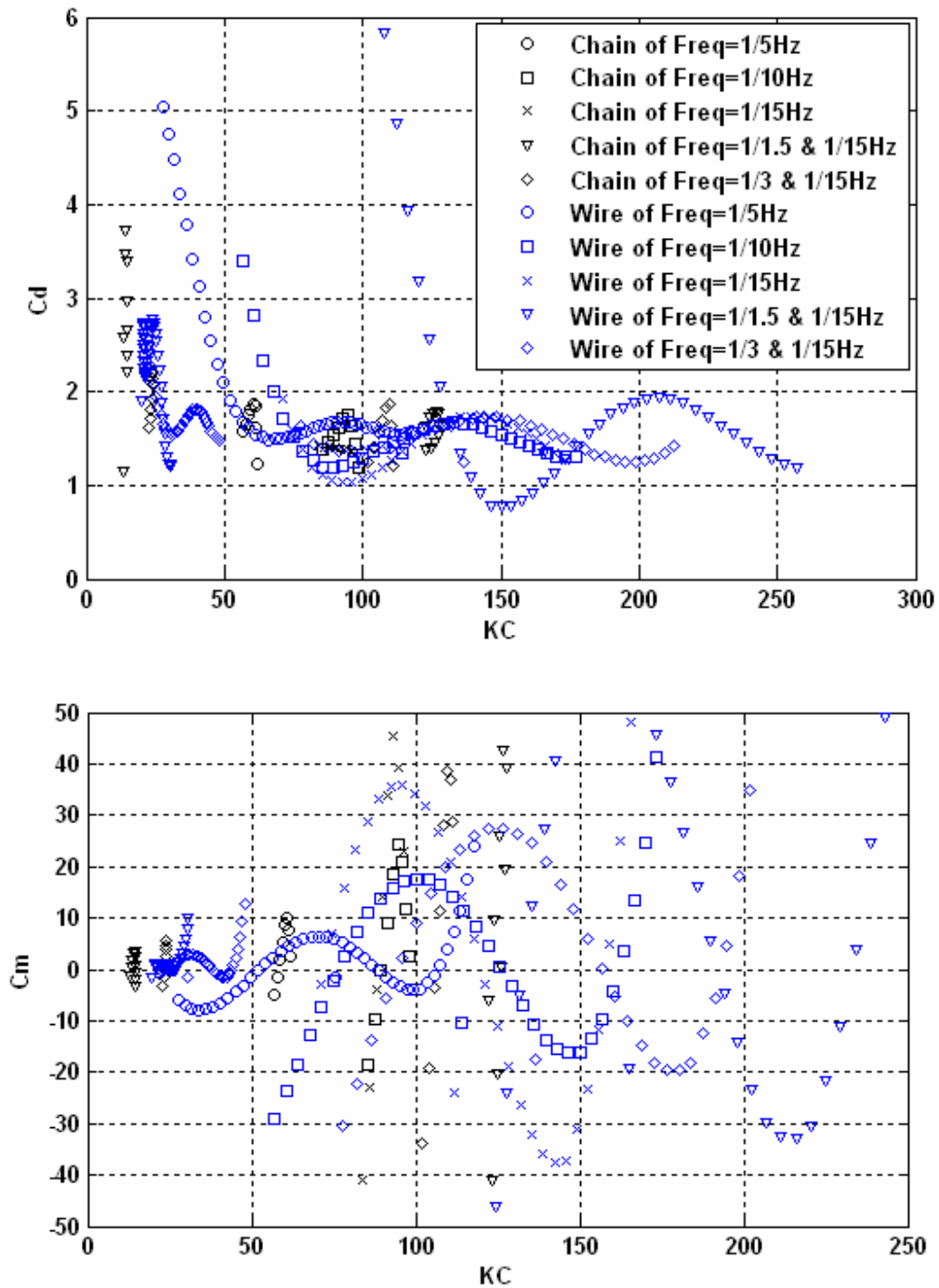
Figure 4.27 Fourier-averaged drag and added mass coefficient of chain – wire

(diameter : : 1.954 cm - 0.915 cm) with semi-taut catenary configuration
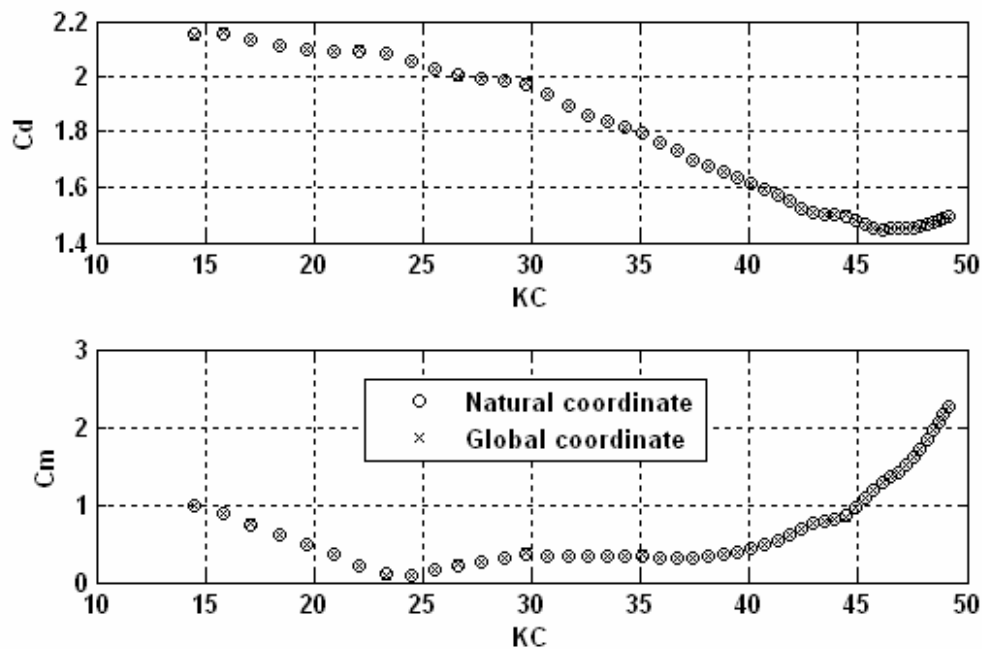
Figure 4.28   Comparison of time-averaged coefficients between natural coordinate and global coordinate systems

Similar trends with a larger amount of scatter are observed in the results for the combined chain-wire-chain mooring (Figure 4.27).   The line was comprised of 5 m of wire with 1 m long lengths of chain at each end.   Since the wire occupied most of the length of the line and both ends of the wire were less confined in the transverse direction than in the case of an all-wire mooring line, more uncertainties in the measured displacement and tension associated with 3-D effects are expected.   Also, the connections between the chain and wire are regarded as discontinuities in the system, which can intensify the uncertainty.

Equations of motion in both the natural coordinate system and the global coordinate

system were provided for the purpose of comparison in Chapter II. All the results previously shown are the outcome of applying the equations of motion in the natural coordinate system. In Figure 4.28, the results from applying the equations of motion in both coordinate systems for the test with the big size chain with 1/5 Hz forced oscillation are given. It is observed that the hydrodynamic force coefficients computed from both formulations are almost identical. Thus, the performance of those equations in terms of the computation of the hydrodynamic force can be deemed as being equivalent.

4.5. Coupled Dynamics of a Mooring Line Attached to a Floating Body

In deep water the impedance provided to the motions of a floater by its mooring system can be significant. Both the mass (inertia) and damping provided by the mooring can be significant contributions to the system mass and damping. Modeling of the system dynamics therefore requires coupling the dynamics of the floater with that of the mooring system.

It is important to distinguish between the local hydrodynamic inertia and damping forces that affect the mooring line motion and the contribution to the inertia and damping of the floater provided by each of the mooring lines. In this section we are concerned primarily with the latter.

For example, mooring line damping is usually classified into friction damping and hydrodynamic damping, which is the major concern of the present study. In addition to that, inertia forces from the mooring and the weight of the mooring line can contribute to the total tension exerted at the top of the line (i.e. at the attachment to the floater). The

horizontal component of this tension that is 90° out of phase with the horizontal motion of the floater contributes to damping of the floater motions. The horizontal component of tension that is either in phase or 180° out of phase with the horizontal motion of the floater contributes static restoration or inertial resistance to the floater motions, respectively.

Note that in deep water the contribution to the dynamic top tension of the mooring line from the integrated effect of the hydrodynamic forces acting on the mooring line will be relatively small. In this case the dynamic top tension is determined primarily by the balance between the line inertia and weight.

Consider the simple case of a floating body moored with a single mooring line and undergoing simple harmonic motion $X = A \sin(wt)$ under the action of monochromatic waves acting on the body. The corresponding equation of motion in the horizontal direction can be expressed as

$$M_b \ddot{X} + B \dot{X} = T_{HD} + T_{HS} + F_{HW} \qquad (4.1)$$

where X : horizontal displacement of floating body $= A \sin(wt)$,

M_b : mass of floating body (including added mass),

B : damping coefficient,

F_{HW} : hydrodynamic horizontal wave exciting force,

T_{HD}, T_{HS} : dynamic and static component of horizontal tension, respectively.

The damping coefficient B in equation (4.1) does not contain the influence of the dynamic behavior of the mooring line. The static tension balances the mean drift force component of the wave exciting force, so that the floater oscillations are referenced to

the mean offset position of the floater. The dynamic tension is the fluctuating part of the tension due to the motion of the body and the induced motion of the mooring line. Since the mooring line dynamics are nonlinear, the dynamic tension could be composed of various harmonic components including a component at the oscillation frequency of the floating body which is supposedly dominant. Separating the in- and out-of-phase components from the dominant harmonic of line tension can clearly demonstrate the role of line tension in the overall motion of the floating body.

The single harmonic component of horizontal tension can be written as

$$T_{HD} = C\sin(wt+\phi) = C_1\sin(wt)+C_2\cos(wt) \tag{4.2}$$

The first term on the right hand side can be regarded as the inertia or restoring component of tension and the second term is obviously the damping component. Determining whether the in-phase component is inertia or restoring force is purely dependent upon the phase of the harmonic. Thus, if a phase shift of 180° is indicated then the in-phase component plays the role of inertia, while if a 0° phase shift is indicated then the in-phase component plays the role of a restoring force. From the simplified example given above, it is deduced that tension can provide contributions to inertia or restoring force of the floating system as well as to the system damping.

The forced oscillation tests described in the previous section can be analyzed to determine the relative contribution of hydrodynamic forces on the mooring lines to the in- and out-of-phase horizontal components of top tension. Such an analysis may provide insight into the effect of uncertainty in the Morison force coefficients on the inertia and damping forces provided by a mooring line to a floating body.

Figure 4.29 illustrates the decomposed top horizontal tension and hydrodynamic

force components for the case of single harmonic forced oscillation at 1/15 Hz. Recalling that the large scale experiments were designed to be representative of a 1:50 scale mooring system, the 1/15 Hz oscillation frequency is representative of low frequency surge motion of a large displacement moored floater. In addition, the magnified displacement signal associated with the forced oscillation of the top of the line is given to facilitate the comparison of phase shift between each harmonic force.

It is noticed that in-phase tension is more significant than out-of-phase and thus tension mostly contributes to the horizontal restoring force in the case of low frequency motion of a floating body. Since the influence of the hydrodynamic force is very small, the tension is considered to be rather driven by inertia of the line and weight variations as the line lifts off and drops back onto the seafloor. However the small out-of-phase component of horizontal tension that does contribute to damping of the horizontal floater motions is almost entirely due to the hydrodynamic force on the mooring line.

On the other hand, for relatively high frequency motion the situation is quite different, as illustrated in Figure 4.30. In this case the horizontal tension and the hydrodynamic force are comparable in magnitude but about 145° out of phase. And the horizontal tension is almost 90° out of phase with the top displacement. This indicates that in high frequency motion the mooring line provides mostly damping, but also a relatively large restoring force to the floater. The out-of-phase horizontal tension (or damping force) is dominated by the hydrodynamic forces on the line. The hydrodynamic force also contributes significantly to the in-phase horizontal tension, which provides a restoring force to the floater.
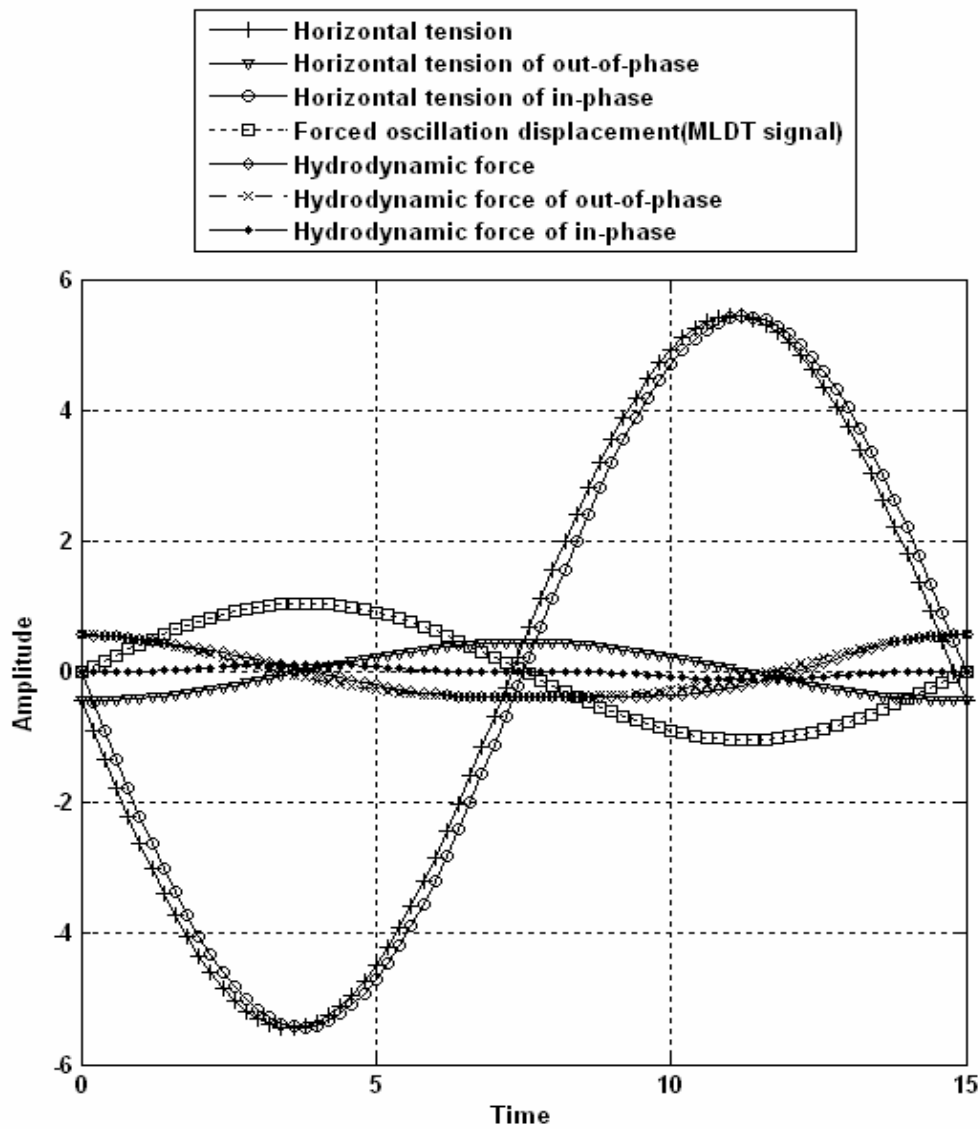
Figure 4.29   Experimentally determined top horizontal tension and hydrodynamic force components of mooring line (chain of 1.954 cm) undergoing forced oscillation at 1/15 Hz [Unit of force is Newton]
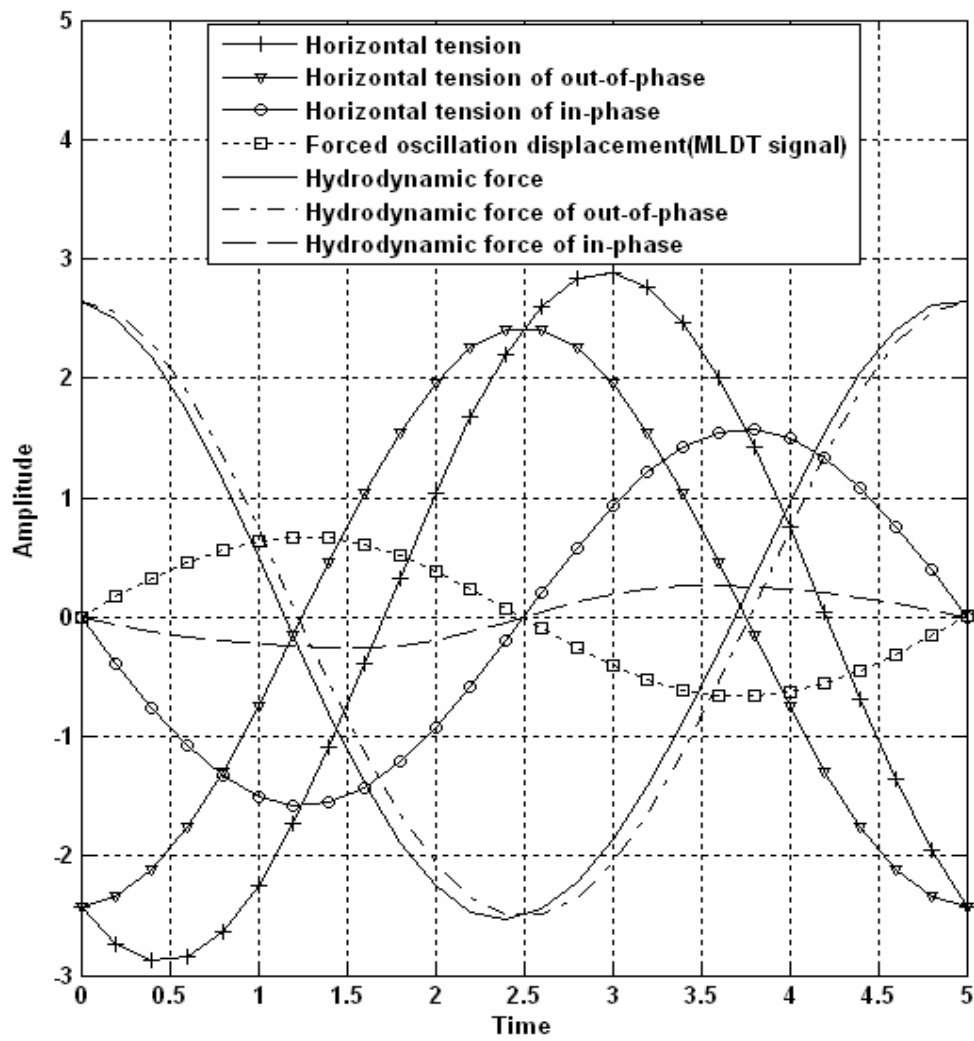
Figure 4.30   Experimentally determined top horizontal tension and hydrodynamic

force of mooring line (chain of 1.954 cm) undergoing forced oscillation of 1/5 Hz

[Unit of force is Newton]
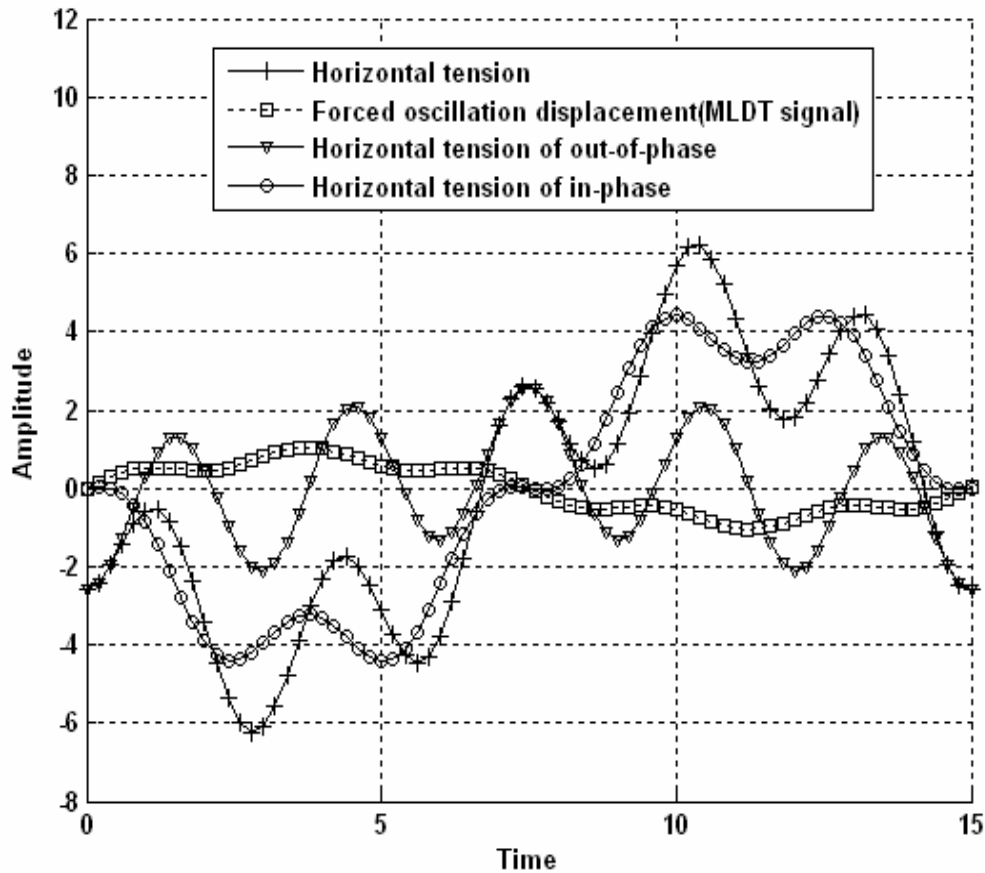
Figure 4.31   Experimentally determined top horizontal tension and hydrodynamic

force of mooring line (chain of 1.954 cm) undergoing forced oscillation with

multiple frequencies of 1/3 Hz and 1/15 Hz [Unit of force is Newton]

For forced oscillation at combined low and high frequencies, the summation of the

two dominant harmonic components of tension is provided in Figure 4.31.   Since the

amplitude of low-frequency oscillation is much larger than that of high-frequency

motion, the overall trend and magnitude of tension appear to be similar to the low

frequency case.   It is observed that the damping portion of tension is mainly attributed to the high frequency motion while the restoring portion of tension is attributed to low frequency motion.   As a result of the superposition of high and low frequency motions, amplification of the dynamic tension is achieved.   Through all the results given, it may be concluded that the dynamics of a mooring line attached to a floating body provides both damping and restoring contributions to the floating system, that in most cases the hydrodynamic force on the mooring line plays an important role in determining the magnitude of the damping or restoring forces, and that the relative magnitude of such forces is mostly driven by the frequency at which a mooring line oscillates.

The effect of drag and added mass coefficient on mooring resistance is briefly investigated through numerical simulation of a single mooring line.   For the comparison, conventional values of Morison coefficients (C_d=1.2 and C_m=1) and the experimentally-derived values (C_d = time-averaged coefficients from Figure 4.23, and C_m = individual test-averaged coefficients as follows : 0.78 for 1/5 Hz , 4.77 for 1/15 Hz, 1.59 for the combined frequency case) from the present experiments were respectively applied for the simulation of forced oscillation at three different frequencies: two single frequency cases at 1/5 Hz and 1/15 Hz and one combined frequency case of 1/3 Hz plus 1/15 Hz.   The tension results from all six simulations are given in Figure 4.32 through Figure 4.34.

Since, as shown in the results with the experimentally-derived coefficients, the hydrodynamic influence of the mooring line on the horizontal tension is quite small for low frequency motion, the effect of the Morison force coefficients (and uncertainty in the force coefficients) is negligible.   But in the other two cases, a remarkable difference

in the magnitude of tension is demonstrated (increase of 5% in multiple harmonic motions and 20% in high frequency motion). Although 5% might seem to be a negligible improvement, it can still make a more important contribution against resonant motion of a floating body than the improvement in high frequency motion, since the resonance is mostly induced by the low frequency wave drift force. Also, there are small phase shifts which can change the balance between in-phase and out-of-phase components. Thus, for reasonable prediction of the motion of a floating body it is recommended to employ the appropriate values of the force coefficients.

Comparison of the tension results between experiments and simulation enable us to verify the derived hydrodynamic coefficients (Figure 4.29 ~ Figure 4.34). Except the single low frequency motion test, the results of simulations with experimentally determined values of the coefficients show better agreement with measurements, which indicates that the coefficients suggested from the present study reasonably represent the hydrodynamic characteristics of mooring elements. In the case of 1/15 Hz oscillation, underestimated values of tension are observed, which might be the result of employing relatively large added mass coefficients, which in turn result in lower mooring line accelerations. Since the large values of added mass coefficient originated from large uncertainty associated with acceleration, the extracted coefficients from low frequency tests seem to be unreliable.
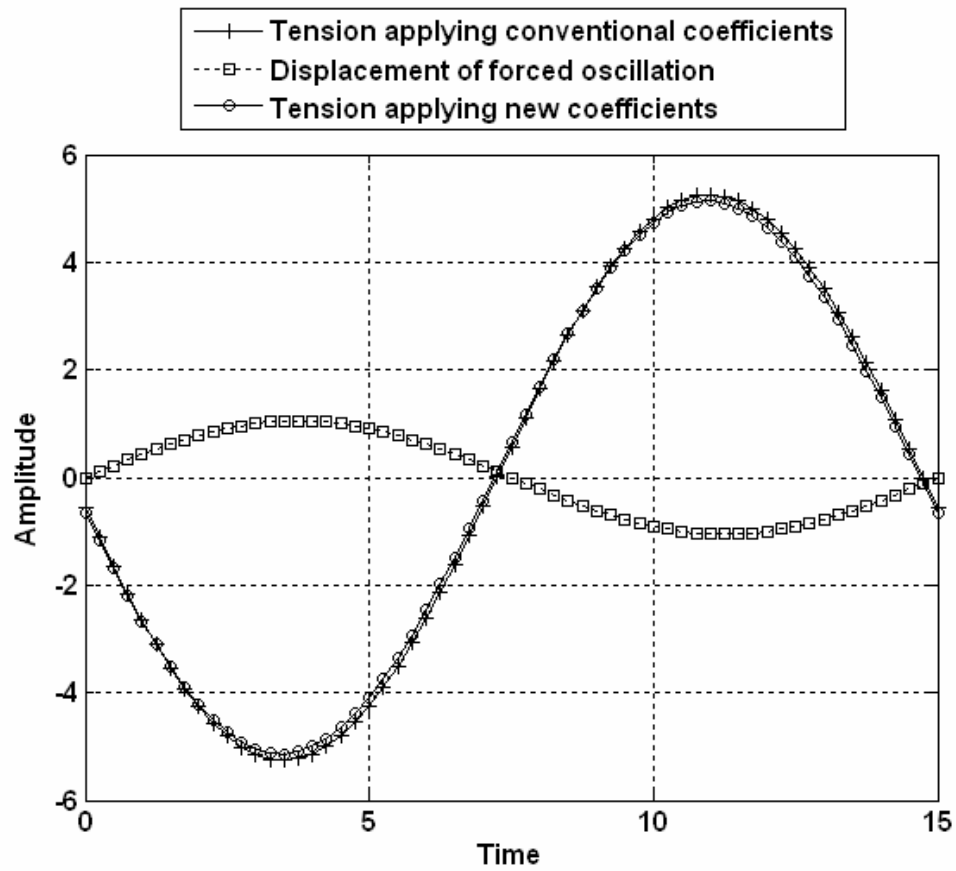
Figure 4.32   Horizontal tension from the simulation of forced oscillation with frequency of 1/15 Hz [Unit of force is Newton]
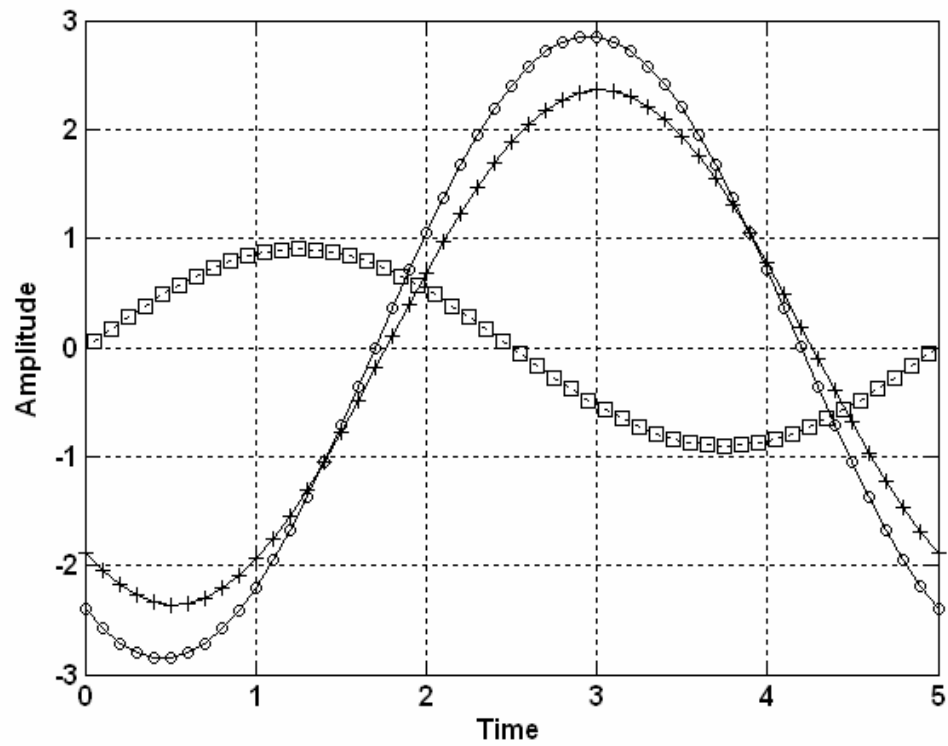
Figure 4.33   Horizontal tension from the simulation of forced oscillation with frequency of 1/5 Hz (legends are same as in Figure 4.32 and unit of force is Newton)
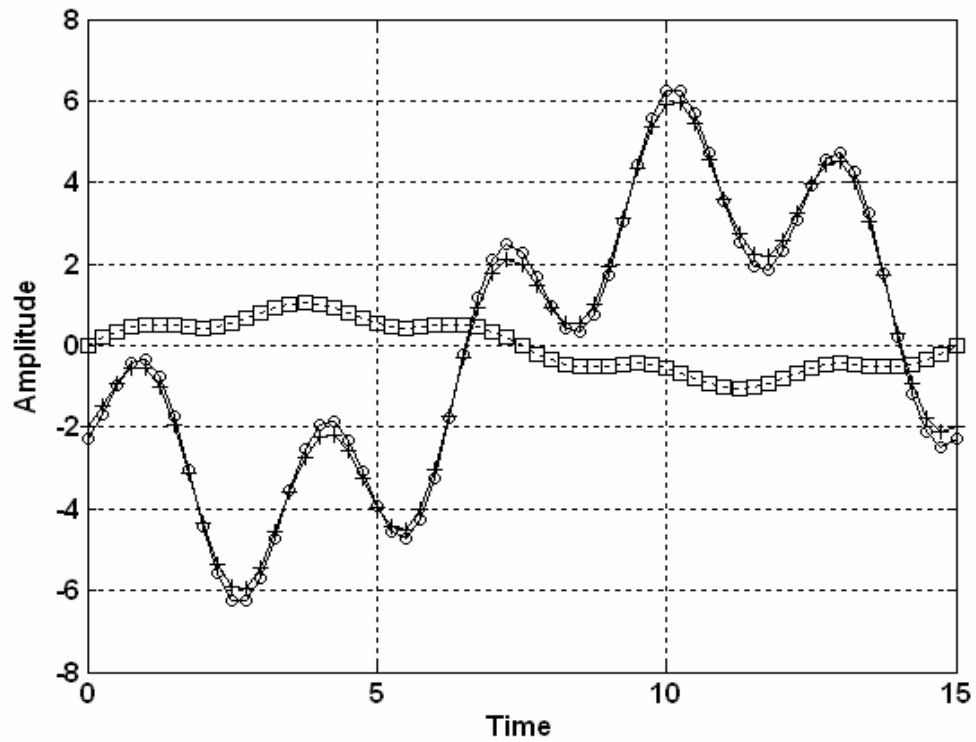
Figure 4.34   Horizontal tension from the simulation of forced oscillation with multiple frequencies of 1/3 Hz and 1/15 Hz (legends are same as in Figure 4.32 and unit of force is Newton)

CHAPTER V
SUMMARY, CONCLUSIONS AND FUTURE STUDY

The present study was structured to develop and establish a efficient, repeatable, automated, low cost, and standardized measurement technique for estimation of Morison drag and inertia coefficients for slender body elements over the full operating range of Re and KC number in three-dimensional flow situations.

The hydrodynamics of two mooring line elements (chain and wire rope) was investigated through small scale and large scale experiments in conjunction with conventional dynamic modeling of slender bodies. Morison's equation was employed for the hydrodynamic force model, in which the force is decomposed into a velocity-dependent drag force and an acceleration-dependent inertia force. These two forces are, in general, well correlated with the Reynolds number and the Keulegan-Carpenter number according to the nature of the surrounding flow around the body. Thus, to provide correlations with both parameters, laboratory tests involving free and forced oscillations of a mooring line were performed.

In order to provide data for a wide range of Re and KC numbers, three different sizes of mooring line elements were investigated for each test condition. During the experiments the displacement of the mooring line at a large number of points and the end force in the line were measured through high speed optical tracking and a triaxial load cell, respectively. In order to reduce the experimental uncertainty, reconstruction of the measured data through polynomial regression (smoothing) and digital filtering was implemented. With the experimentally measured nodal positions along the line and line

end forces as input data, the equation of motion for the line was solved to determine the hydrodynamic force at each time step.

In addition to the hydrodynamic analysis, measurements of bending stiffness for wire ropes were performed, as there was a concern that internal shear forces generated by bending in the relatively short lengths of wire rope employed for the tests could be significant. Two shear-curvature relations were proposed: one with the assumption of small angle, the other with no such assumption. The results from the new relation without the small angle assumption showed less variation than those from the conventional relation. Values of the bending stiffness for all wire ropes tested were found to be small enough to be negligible in the hydrodynamic analysis.

From the free oscillation tests, instantaneous values of drag coefficients were derived from the measurements based on the assumption of constant added mass coefficient. Since the preliminary results had considerable scatter and bias due to measurement error and the assumption of constant added mass coefficient, a couple of criteria were introduced to filter out unreasonable data. The filter criteria were based on the ratio of inertia to drag force and the ratio of tension to drag force, and both were shown to fulfill the task well. The drag coefficients from both the small scale and the large scale tests exhibited a narrow range of scatter and the variation with Re can be summarized as follows: from the small scale data C_d varies from 0.7 to 2 for Re ranging from 250 to 2500, and from the large scale data C_d varies from 0.5 to 1.8 for Re ranging from 500 to 25000.

From the forced oscillation tests, instead of instantaneous values, Fourier- and time-averaged values of both drag and added mass coefficients were obtained as a function of

KC number. Only the Fourier-averaged coefficients from the response harmonic at the same frequency as the forcing frequency were considered because all other (generally much smaller magnitude) harmonic components were contaminated by either the optical tracking error or the filtering process. Due to low accuracy in determining the acceleration, the derived added mass coefficients in general exhibited more scatter than the drag coefficients and they did not have a consistent KC-dependence. Balance transfer between the drag and added mass force was observed through the entire set of results. That is, as the drag coefficient increases, the added mass coefficient decreases, sometimes falling below zero.

Two different configurations of chain mooring were tested, semi-taut catenary and suspended catenary, to investigate the effect of basin floor contact. The anchor point for the suspended catenary mooring was raised above the floor so that the line near the anchor would never come in contact with the floor. This suspended configuration was found to be an improper configuration for the estimation of Morison force coefficients due to the unexpected hydrodynamic behavior of the upper section of the mooring line. The results of all-wire and chain-wire-chain mooring configurations showed larger variations with KC number in the Morison force coefficients, particularly at low KC, possibly due to bending and torsional effects associated with the wire rope construction. Overall, it is observed that the Fourier-averaging process can itself attenuate the errors associated with measurement of line kinematics.

Time-averaged Morison coefficients were estimated by applying the least-square method to the amplitude spectrum of the Morison force. The coefficients appeared to be larger in magnitude than the Fourier-averaged coefficients at low KC number due to

the relatively low accuracy in determining the kinematics, which could hardly be recovered by the time averaging process. Two different dynamic equations, one formulated on the natural (body-fixed) coordinate system and the other on the Cartesian global coordinate system, were examined for the computing performance of the hydrodynamic force on the mooring line and it is concluded that both formulations carry out the task equivalently.

The impedance provided by a mooring line attached to a floating body was discussed in terms of the damping and restoring contribution of the line to the motion of the body. From the experimental results it was shown that in low frequency motion the mooring line mostly contributes a quasi-static restoring force while in high frequency motion the mooring lines generates a large damping contribution to the floater motion. Since the low frequency surge/sway/yaw motions of a moored floater are generally resonant responses, they are controlled by damping. This means that even though in low frequency motion the damping force induced by the mooring line is small relative to the restoring force, to the extent that the damping force is dominated by the integrated effect of the hydrodynamic forces on the line, uncertainty in the Morison force coefficients can be directly related to uncertainty in the predicted low frequency motion of the floater.

For both the validation of experimentally-derived coefficients and the investigation on the importance of Morison force coefficients on mooring impedance, forced oscillations of a mooring line were simulated numerically with both conventional values of force coefficients and time-averaged coefficients estimated from the experiments. By comparison of the simulated dynamic tension based on the experimental coefficients and traditional coefficients, it was noted that the experimental coefficients well recreated

the dynamic tensions observed in the experiment and thus can be considered to be well estimated through the present analysis.

Throughout the entire procedure given here, the objectives of the study have been pursued and most of them have been achieved in the aspect of developing a new measurement technique. However, the accuracy and reliability of the derived force coefficients have not been addressed satisfactorily due to considerable measurement error. Moreover, detailed investigation of three dimensional flow conditions associated with out-of-plane top end displacements and out-of-plane motions associated with VIV and lift forces has not been performed at all.

Although initially pursued, the planned extension to 3D measurements was found to be unfeasible due to obstruction of the field of view in front of the observation window beneath the wavemaker in the OTRC basin. Therefore, 3-D optical tracking with reduced field of view using multiple cameras installed in waterproof enclosures in the basin could be pursued as future work and is expected to resolve the measurement uncertainty problem to a certain extent. However this will be a very expensive experimental set-up. Improvement of the image calibration technique, which was the toughest challenge during and after the large scale tests, should also be pursued to further minimize the optical tracking error.

REFERENCES

Bearman, P. W., Chaplin, J. R., Grahnam, J. M. R., Kostense, J. K., Hall, P. F., and Klopman, G., 1985. The loading on a cylinder in post-critical flow beneath periodic and random waves. 4th International Conference on Behaviour of Offshore Structures, 213-225.

Bliek, A., 1984. Dynamics analysis of single span cables. Doctoral Dissertation, Ocean Engineering, Massachusetts Institute of Technology.

Borgman, L. E., 1965. Spectral density for ocean wave forces. Journal of Waterways and Harbors Division, ASCE, 147-182.

Borgman, L. E., 1967. Random hydrodynamic forces on objects. The Annals of Mathematical Statistics, 38, 37-51.

Borgman, L. E., 1969. Ocean wave simulation for engineering design. Journal of the Waterways and Harbors Division, ASCE, 95, 4, 557-583.

Bostrom, T., 1987. Hydrodynamic force coefficients in random wave conditions. Dr.Ing. Thesis, Section of Structural Engineering, Norwegian Institute of Technology, Trondhein, Norway.

Braza, M., Chassaing, P., and Ha Minh, H., 1985. Numerical study and physical analysis of the pressure and velocity fields in the near wake of a circular cylinder. Journal of Fluid Mechanics, 165, 79-130.

Bretschneider, C. L., 1967. Probability distribution of wave force. Journal of the Waterways and Harbors Division, ASCE, WW2, 5-26.

Burrows, R., 1977. Quasistatic response of offshore structures using probabilistic

methods. Applied Mathematical Modelling, 1, 325-332.

Dean, R. G., and Aagaard, P. M., 1970. Wave forces: Data analysis and engineering calculation method. Journal of Petroleum Technology, 368-375.

Dercksen, A., Huijsmans, R. H. M., and Wichers, J. E. W., 1992. An improved method for calculating the contribution of hydrodynamic chain damping on low-frequency vessel motions. Offshore Technology Conference, OTC 6967.

Driscoll, J. R., 1972. Forces on cylinder oscillating in water. Thesis, Naval Postgraduate School, Monterey, CA.

Garrison, C. J., Field, J. B., and May, M. D., 1977. Drag and inertia forces on a cylinder in periodic flow. Journal of the Waterways, Port, Coastal and Ocean Division, ASCE, 103, 2, 193-204.

Horton, T. E., and Feifarek, M. J., 1981. Vorticity transport intergral concept for determining wave forces on submerged bodies. Journal of Hydronautics, 15, 34-38.

Horton, T. E., and Rish III, J. W., 1981. A study advancing wave-force methodology - a one-dimensional formulation of the inertial pressure concept. International Symposium on Hydrodynamics in Ocean Engineering, 585-600.

Howell, C. T., 1992. Investigation of the dynamics of low-tension cables. Doctoral Dissertation, Ocean Engineering, Massachusetts Institute of Technology.

Huse, E., 1986. Influence of mooring line damping upon rig motions. Offshore Technology Conference, OTC 5204.

Hwang, Y.-L., 1986. Nonlinear dynamic analysis of mooring lines. Proceedings of the 5th International Offshore Mechanics and Arctic Engineering Symposium, 3, 499-506.

Hwang, Y.-L., 1998. Numerical model tests for mooring damping. 17th International

Conference on Offshore Mechanics and Arctic Engineering, OMAE98-0444.

Justesen, P., 1990. A numerical study of oscillating flow around a circular cylinder. Journal of Fluid Mechanics, 222, 157-196.

Kaplan, P., Jiang, C. W., and Dello Stritto, F. J., 1981. Determination of offshore structure Morison equation force coefficients via system identification techniques. International Symposium on Hydrodynamics in Ocean Engineering, 469-489.

Keulegan, G. H., and Carpenter, L. H., 1958. Forces on cylinders and plates in an oscillating fluid. Journal Of Research of the National Bureau of Standards, 60, 423-440.

Kim, Y. Y., and Hibbard, H.C., 1975. Analysis of simultaneous wave force and water particle velocity measurements. Offshore Technology Conference, OTC 2192.

Lighthill, J., 1979. Waves and hydrodynamic loading. Proceedings of 2nd International Conference on Behaviour of Offshore Structures, 1, 1-40.

Madsen, O. S., 1986. Hydrodynamic force on circular cylinders. Applied Ocean Research, 8, 151-155.

Murashige, S., Kinoshita, T., and Hinatsu, M., 1989. Direct calculations of the Navier Stokes equations for forces acting on a cylinder in oscillatory flow. 8th International Offshore Mechanics and Arctic Engineering Symposium, 411-418.

Nordgren, R. P., 1974. On computation of the motion of elastic rods. Journal of Applied Mechanics, 777-780.

OrcaFlex, Version 8.4. Orcina Limited, Daltongate Ulverston, Cumbria LA12 7AJ, United Kingdom.

Pierson, W. J., and Holmes, P., 1965. Irregular wave forces on a pile. Journal of the

Waterways and Harbors Division, ASCE, 91, 4, 1-10.

Rodenbusch, G., and Kallstrom, C., 1986. Forces on a large cylinder in random two-dimensional flows. Offshore Technology Conference, OTC 5096.

Sarpkaya, T., and Garrison, C.J., 1963. Vortex formation and resistance in unsteady flow. Journal of Applied Mechanics, 30, 16-24.

Sarpkaya, T., 1966. Experimental determination of the critical Reynolds number for pulsating Poiseuille flow. Journal of Basic Engineering, ASME, 88, 589-598.

Sarpkaya, T., 1976a. Vortex shedding and resistance in harmonic flow about smooth and rough circular cylinder at high Reynolds numbers. Naval Postgraduate School Technical Report, No. NPS-59SL76021.

Sarpkaya, T., 1976b. Vortex shedding and resistance in harmonic flow about smooth and rough circular cylinders. Proceedings of International Conference on Behaviour of Offshore Structures, 1, 220-235.

Schulz, K. W., and Kallinderis, Y., 2000. Three-dimensional numerical prediction of the hydrodynamic loads and motions of offshore structures. Journal of Offshore Mechanics and Arctic Engineering, 122, 294-300.

Smith, P. A., and Stansby, P. K., 1988. Impulsively started flow around a circular cylinder by the vortex method. Journal of Fluid Mechanics, 194, 45-77.

Tickell, R. G., 1977. Continuous random wave loading on structural members. The Structural Engineer, 55, 5, 209-222.

Triantafyllou, M. S., Yue, D. K. P., and Tein, D.Y. S., 1994. Damping of moored floating structures. Offshore Technology Conference, OTC 7489.

Webster, W. C., 1995. Mooring-induced damping. Ocean Engineering, 22, 6, 571-591.

Wichers, J. E. W., and Huijsmans, R. H. M., 1990. The contribution of hydrodynamic damping induced by mooring chains on low-frequency vessel motions. Offshore Technology Conference, OTC 6218.

APPENDIX A

HYDRODYNAMIC COEFFICIENTS ESTIMATED FROM THE FORCED OSCILLATION TESTS IN THE OTRC BASIN

A.1. Small Size Mooring

Graph legend [○ : Frequency = 1/5 Hz, □ : Frequency = 1/10 Hz, × : Frequency= 1/15 Hz, ▽ : Frequency = 1/1.5 & 1/15 Hz, ◊ : Frequency = 1/3 & 1/15 Hz]
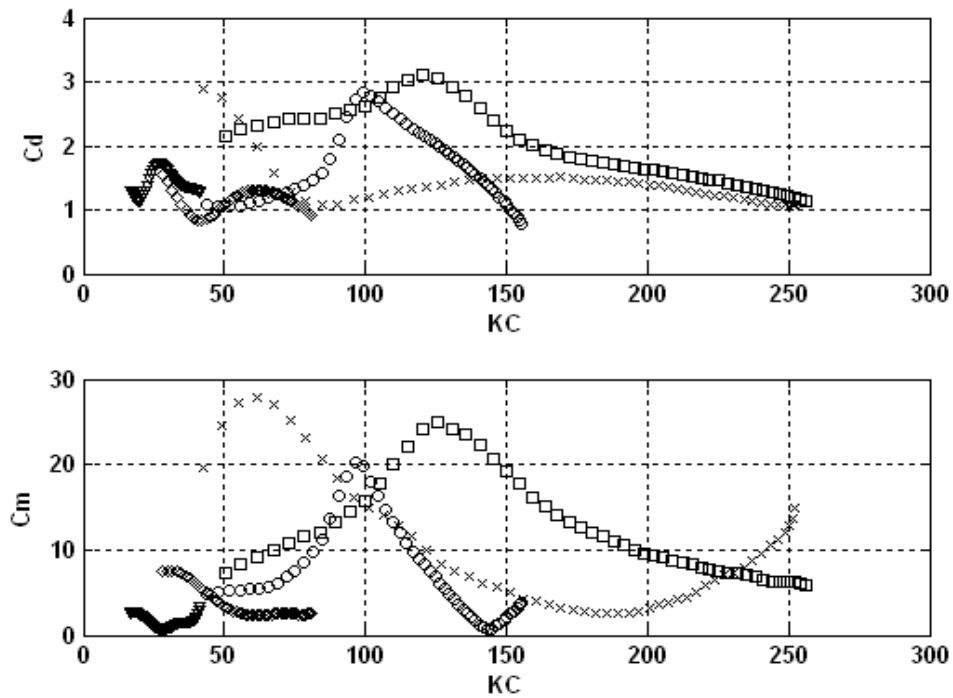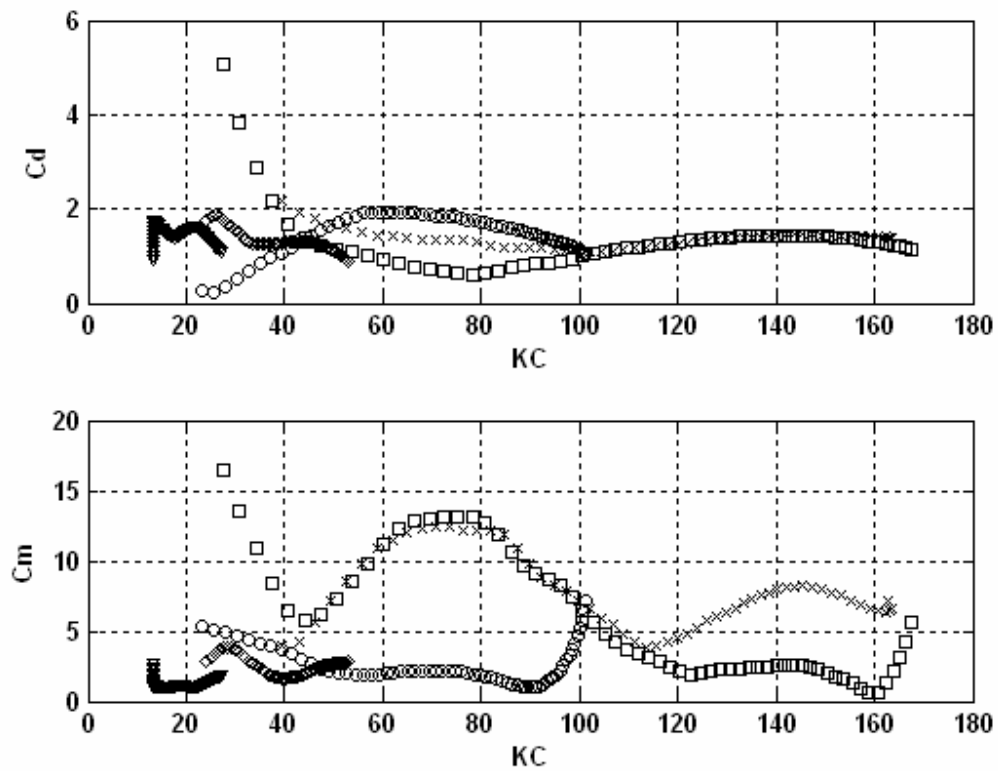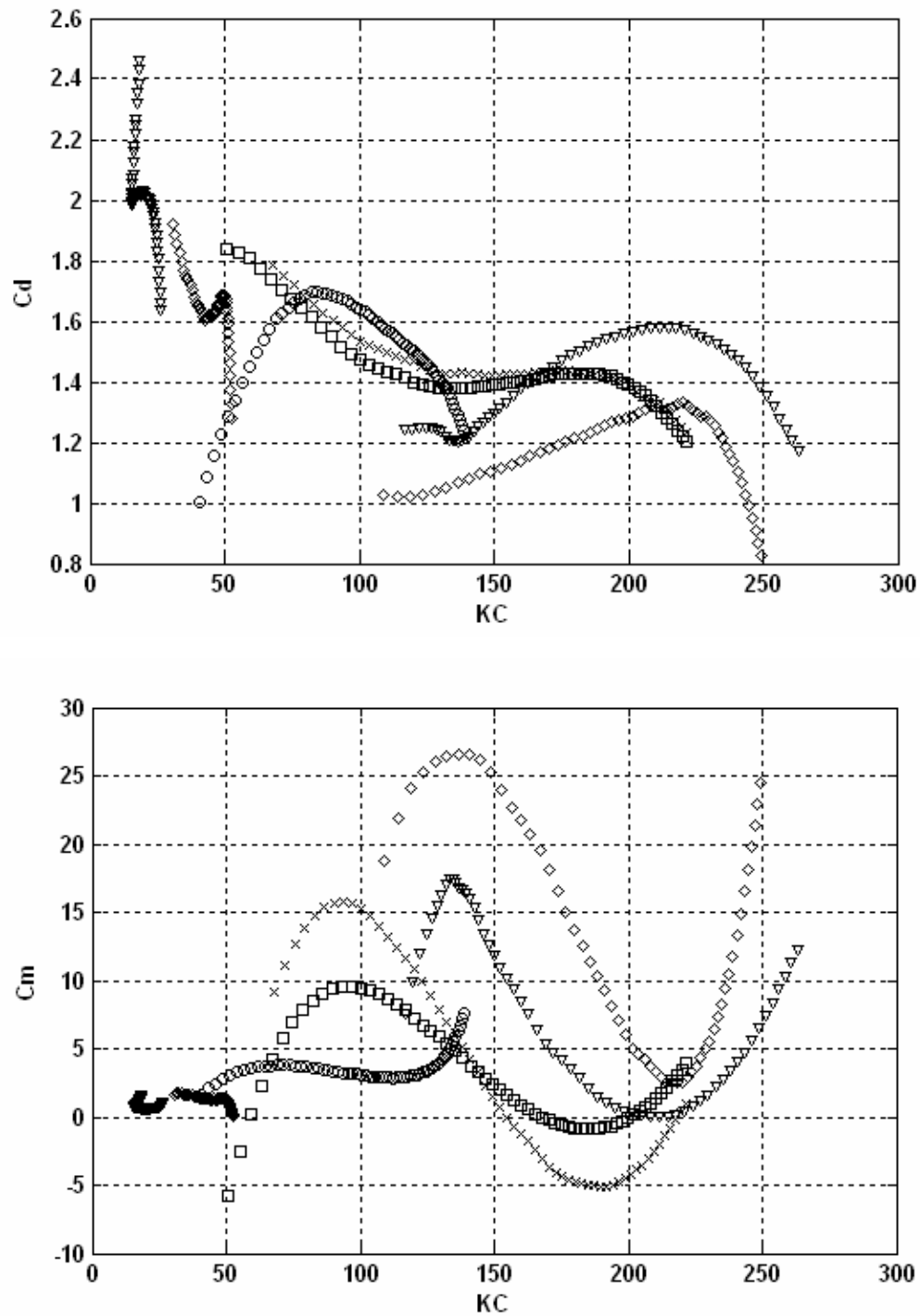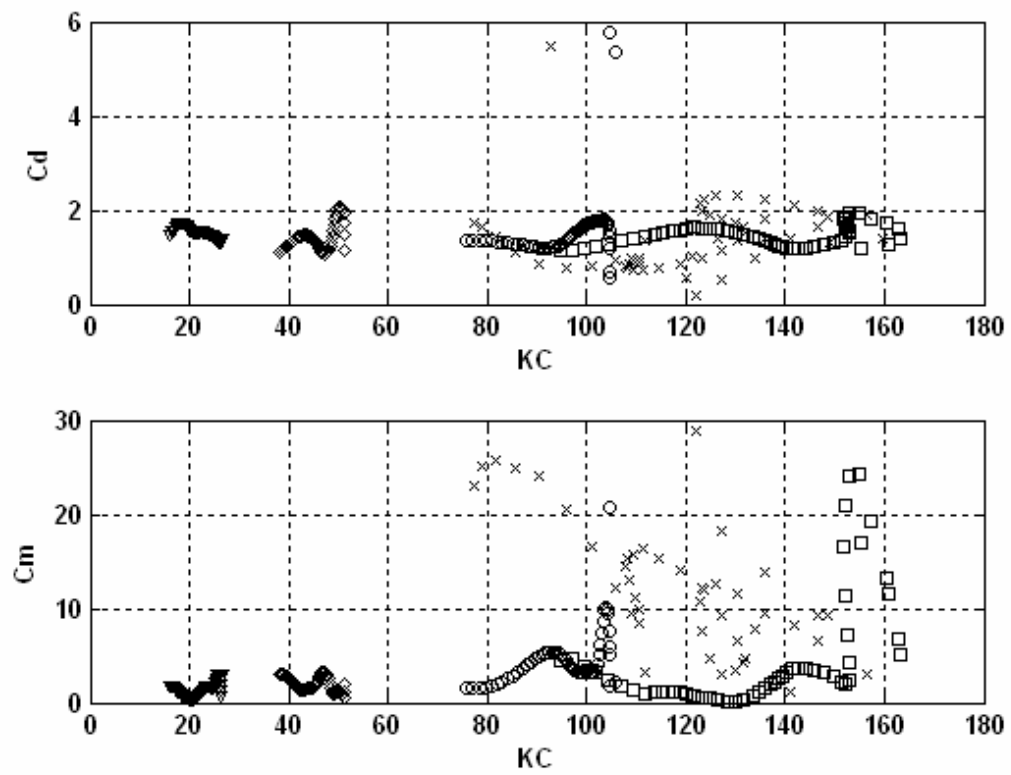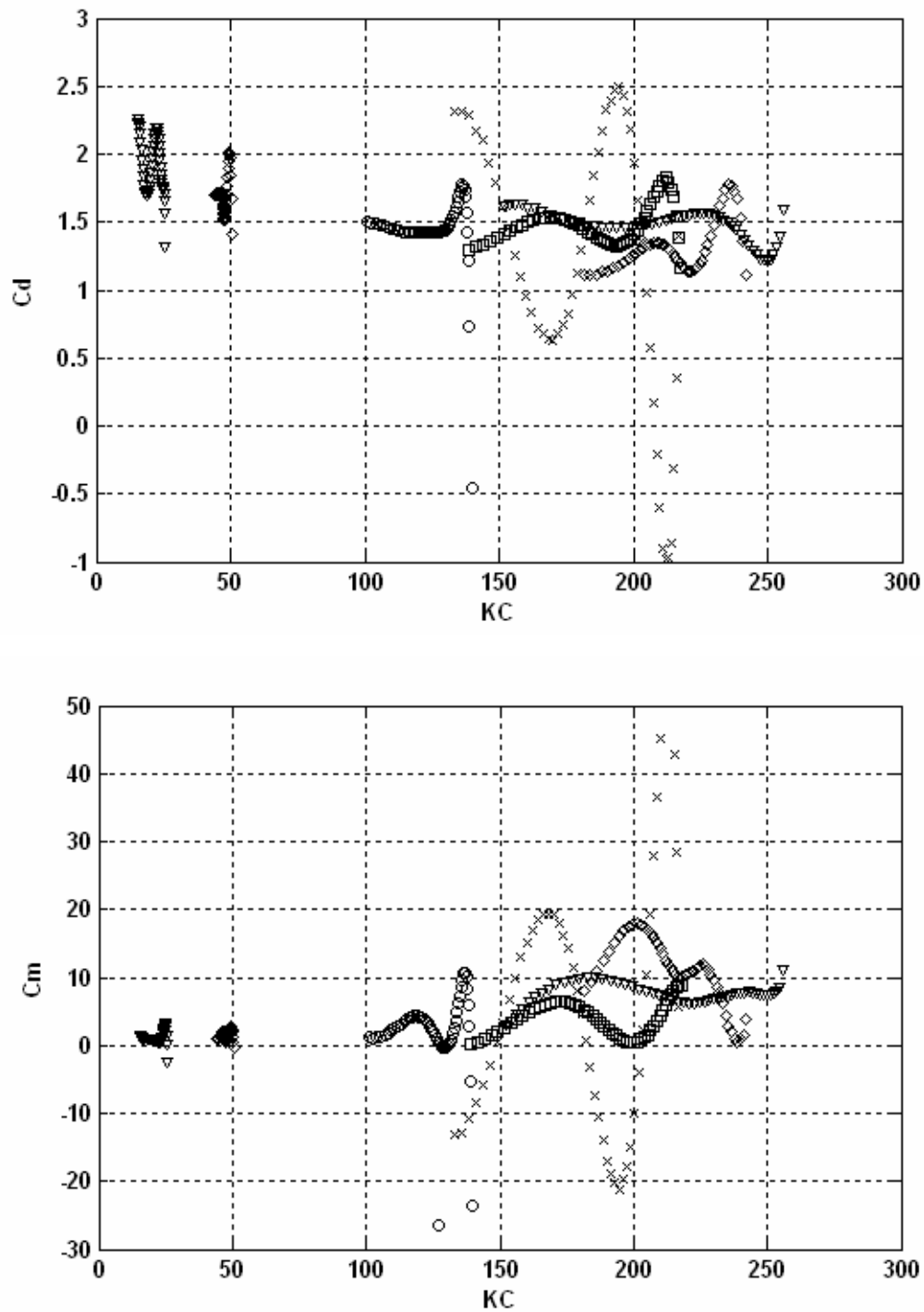

Figure A.1   Time-averaged coefficient of chain (diameter: 0.584 cm) with semi-taut catenary configuration
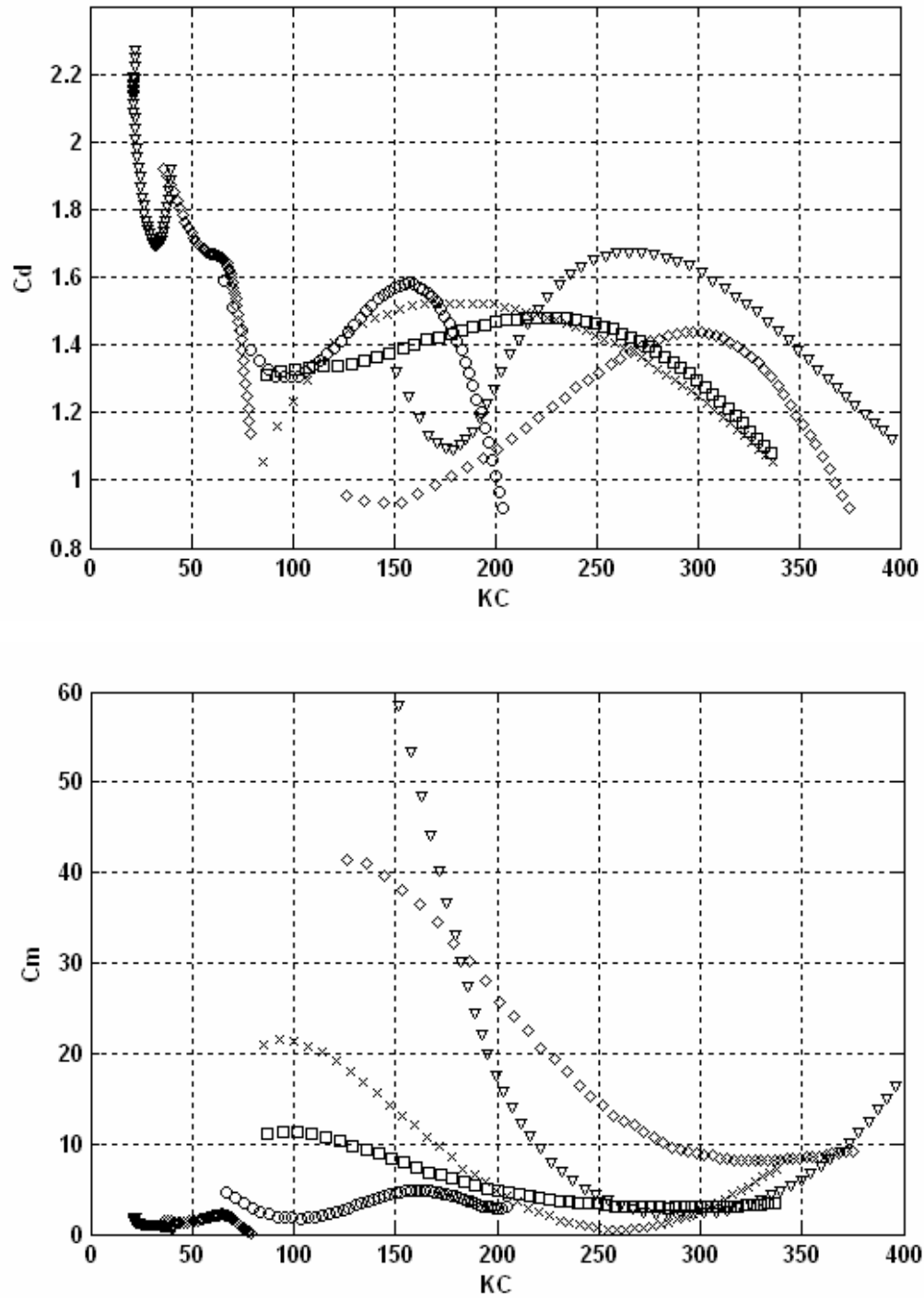
Figure A.2   Fourier-averaged drag and added mass coefficient of chain (diameter:

0.584 cm) with semi-taut catenary configuration
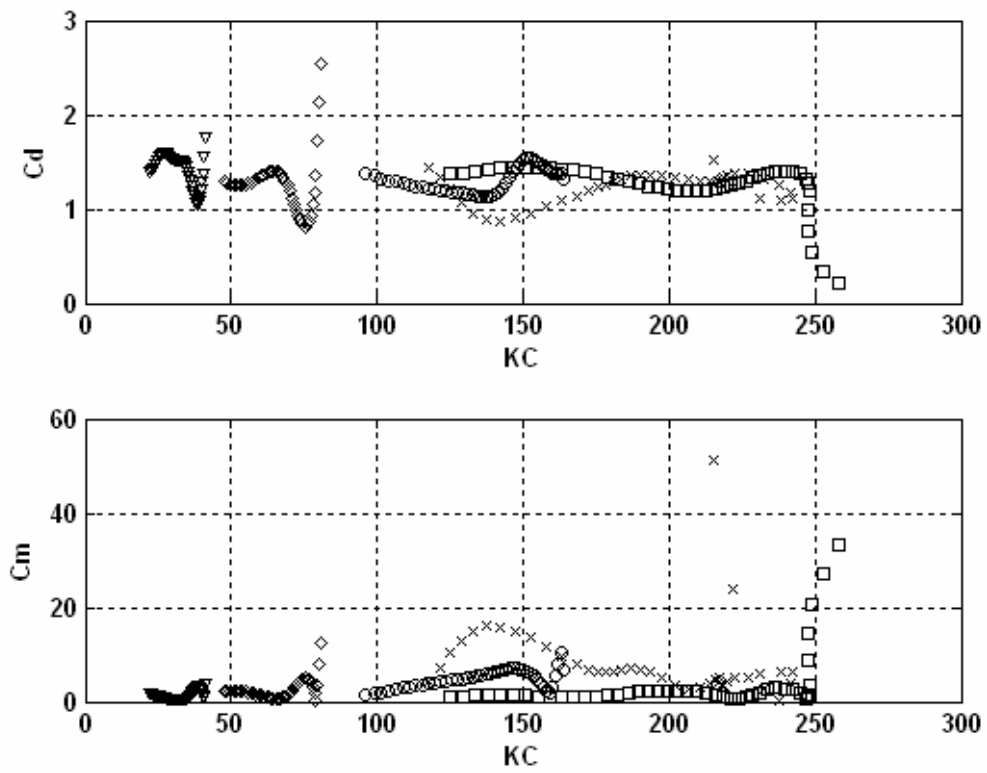
Figure A.3   Time-averaged drag and added mass coefficient of chain (diameter: 0.584 cm) with suspended catenary configuration
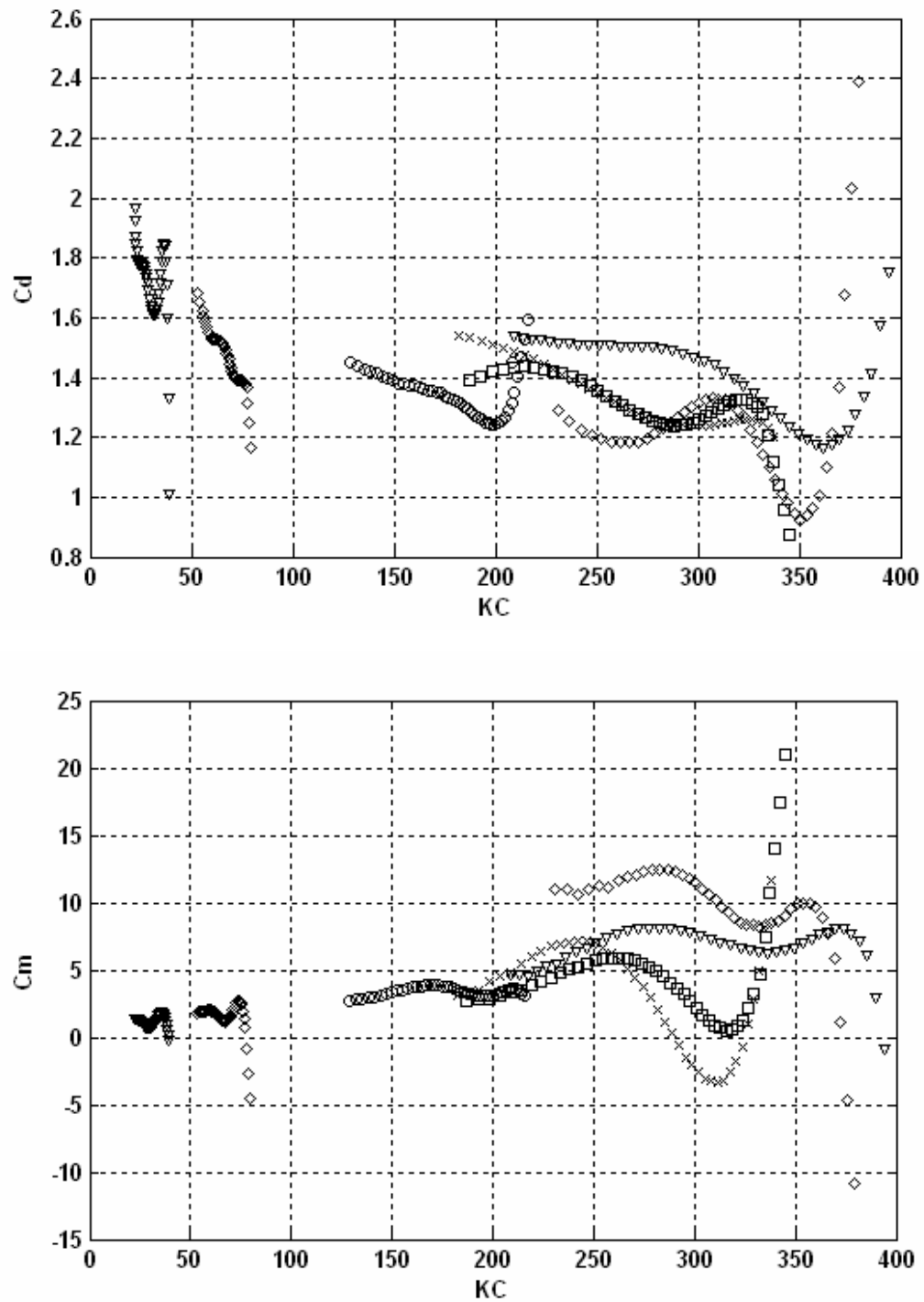
Figure A.4   Fourier-averaged drag and added mass coefficient of chain (diameter:

0.584 cm) with suspended catenary configuration
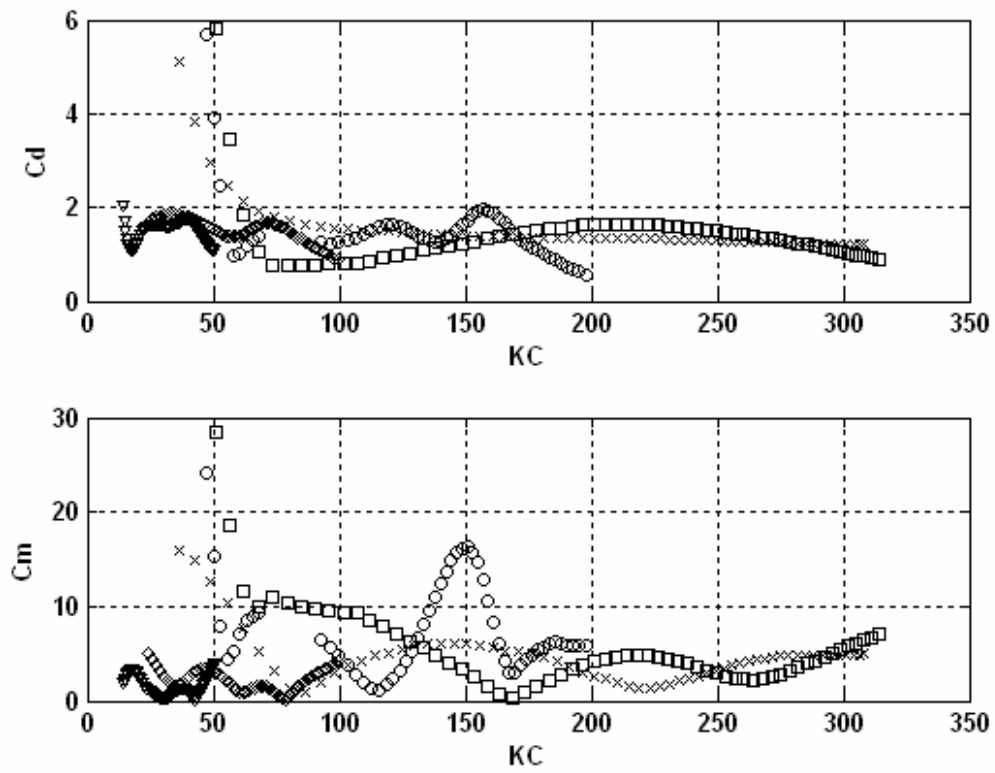
Figure A.5   Time-averaged drag and added mass coefficient of wire (diameter: 0.479 cm) with semi-taut catenary configuration
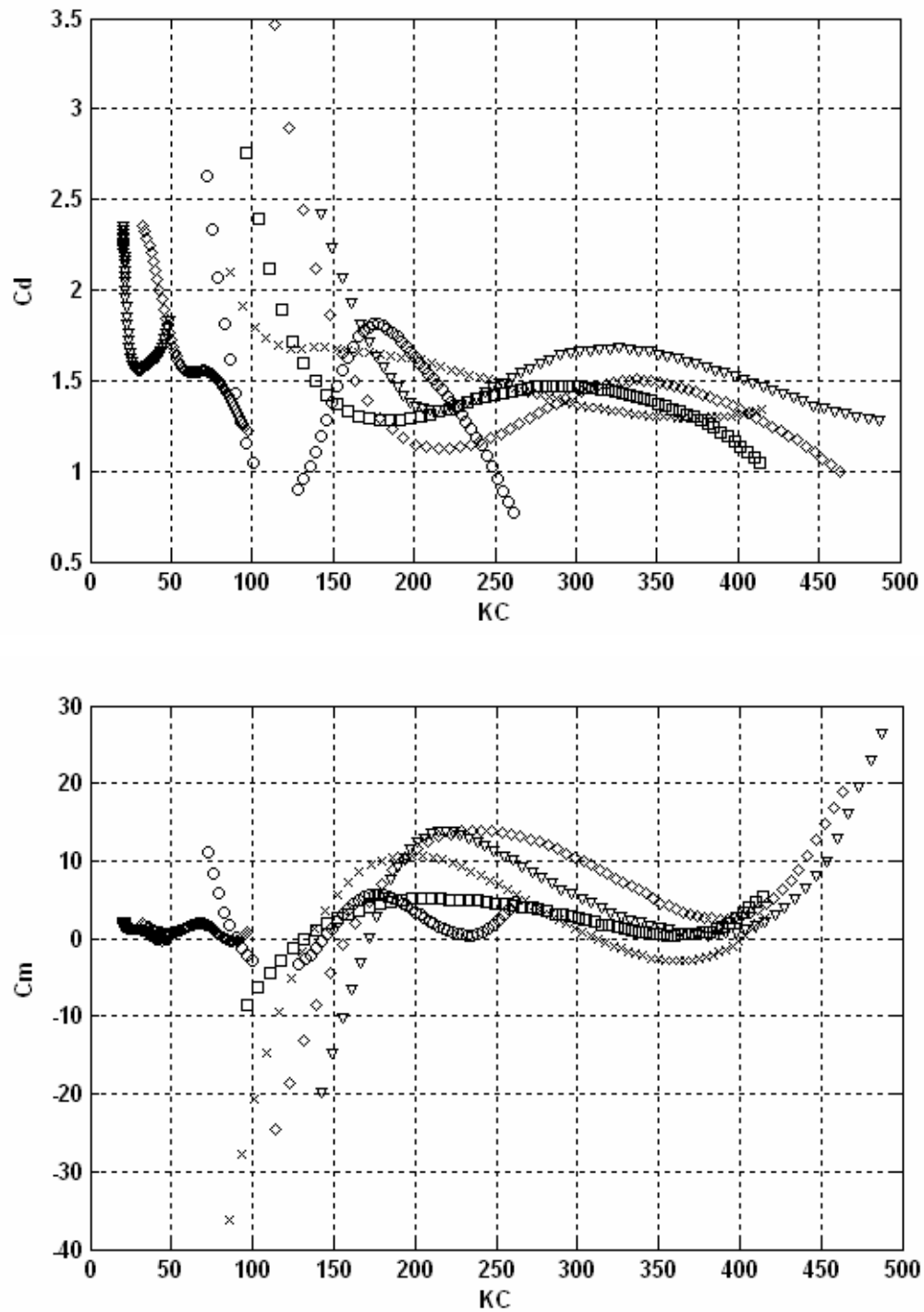
Figure A.6   Fourier-averaged drag and added mass coefficient of wire (diameter: 0.479 cm) with semi-taut catenary configuration
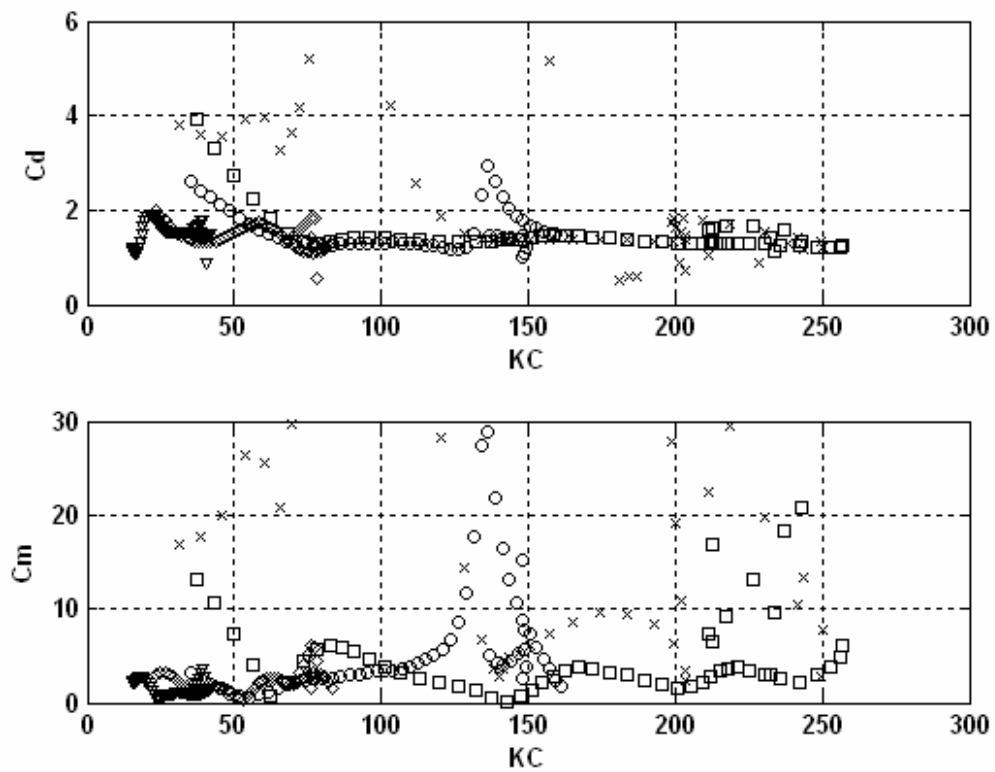
Figure A.7   Time-averaged drag and added mass coefficient of chain – wire

(diameter: 0.584 cm - 0.479 cm) with semi-taut catenary configuration
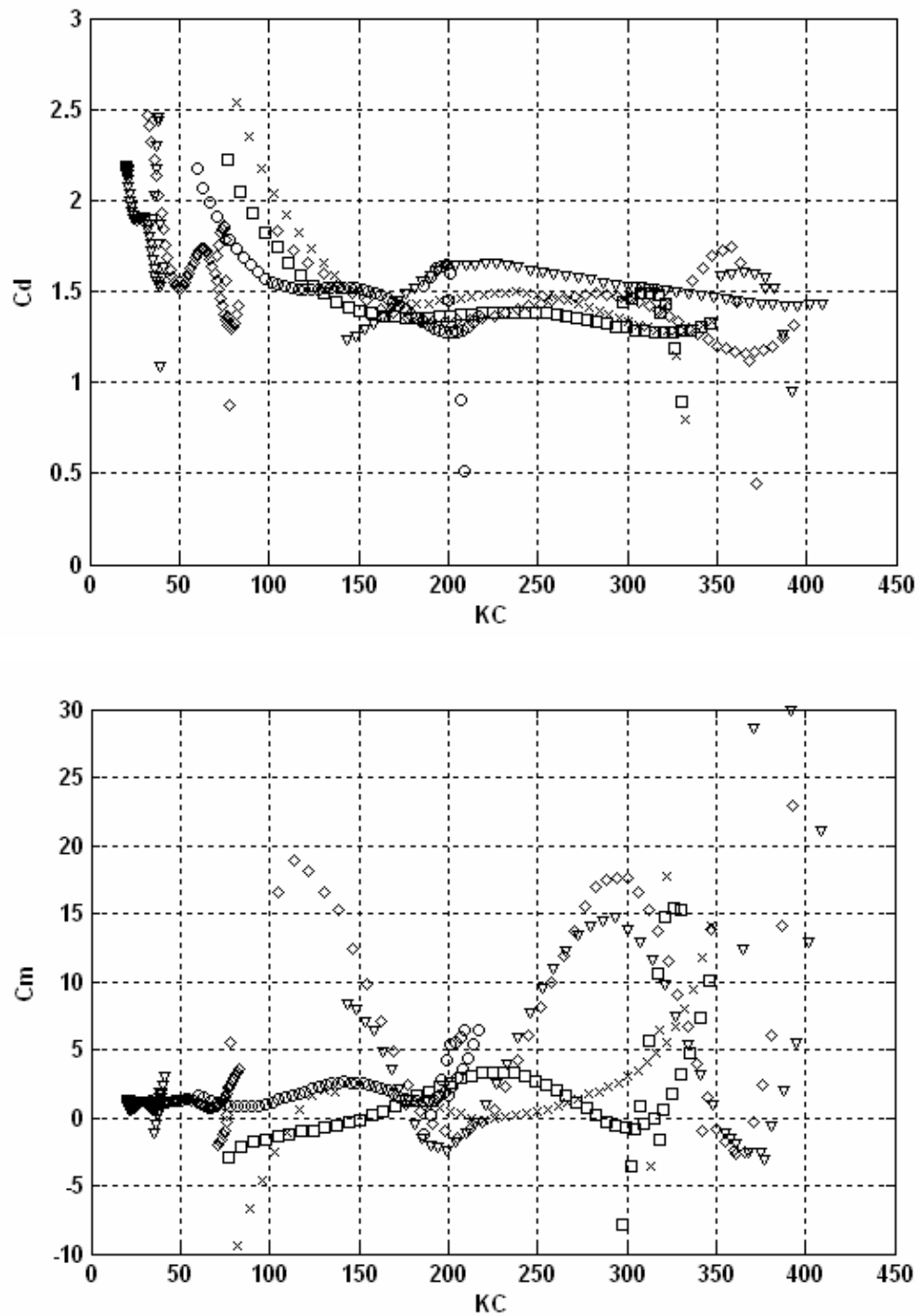
Figure A.8   Fourier-averaged drag and added mass coefficient of chain – wire

(diameter: 0.584 cm - 0.479 cm) with semi-taut catenary configuration

A.2. Medium Size Mooring

Graph legend [○ : Frequency = 1/5 Hz, □ : Frequency = 1/10 Hz, × : Frequency= 1/15 Hz, ▽ : Frequency = 1/1.5 & 1/15 Hz, ◊ : Frequency = 1/3 & 1/15 Hz]

Figure A.9   Time-averaged coefficient of chain (diameter: 0.897 cm) with semi-taut catenary configuration

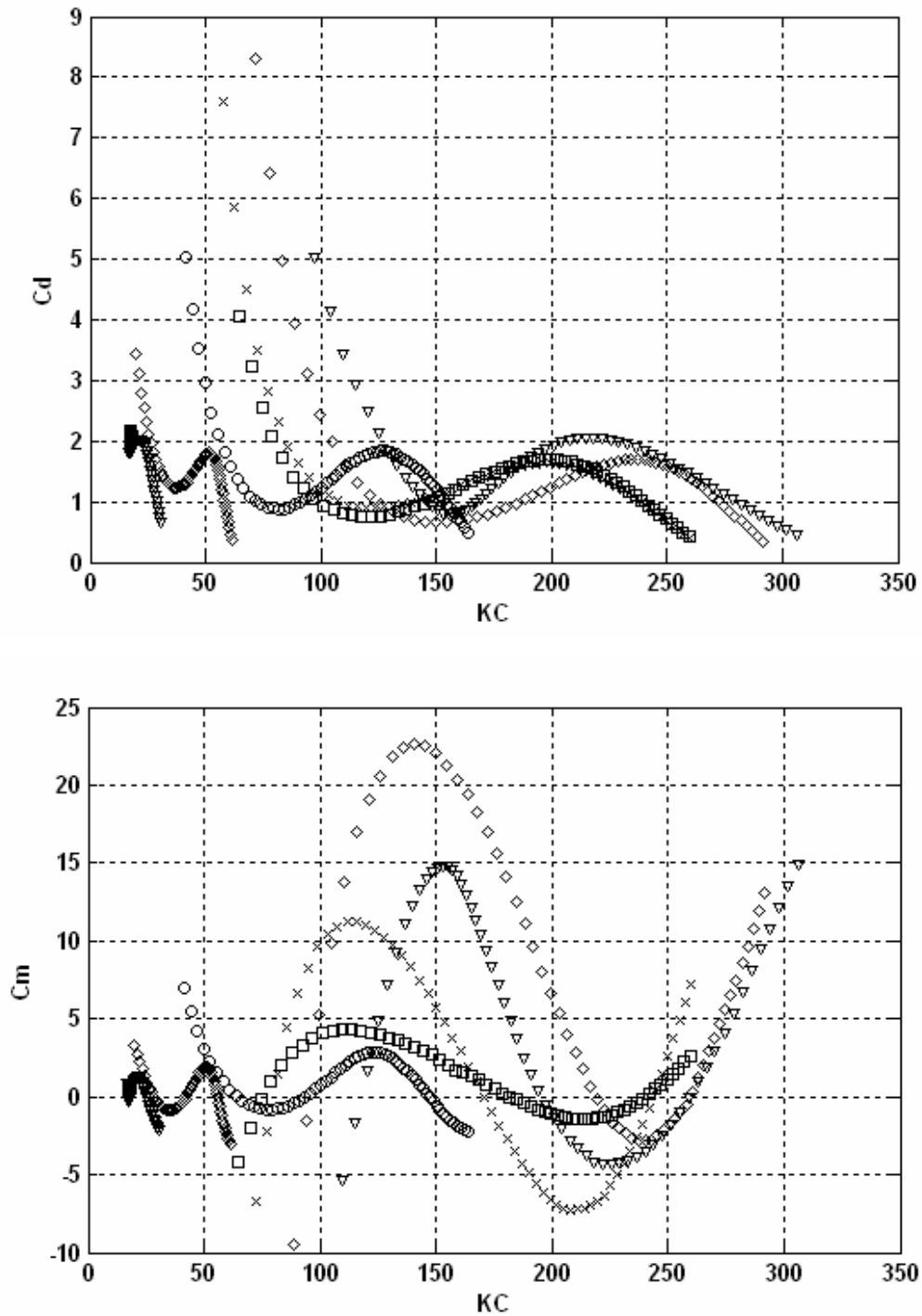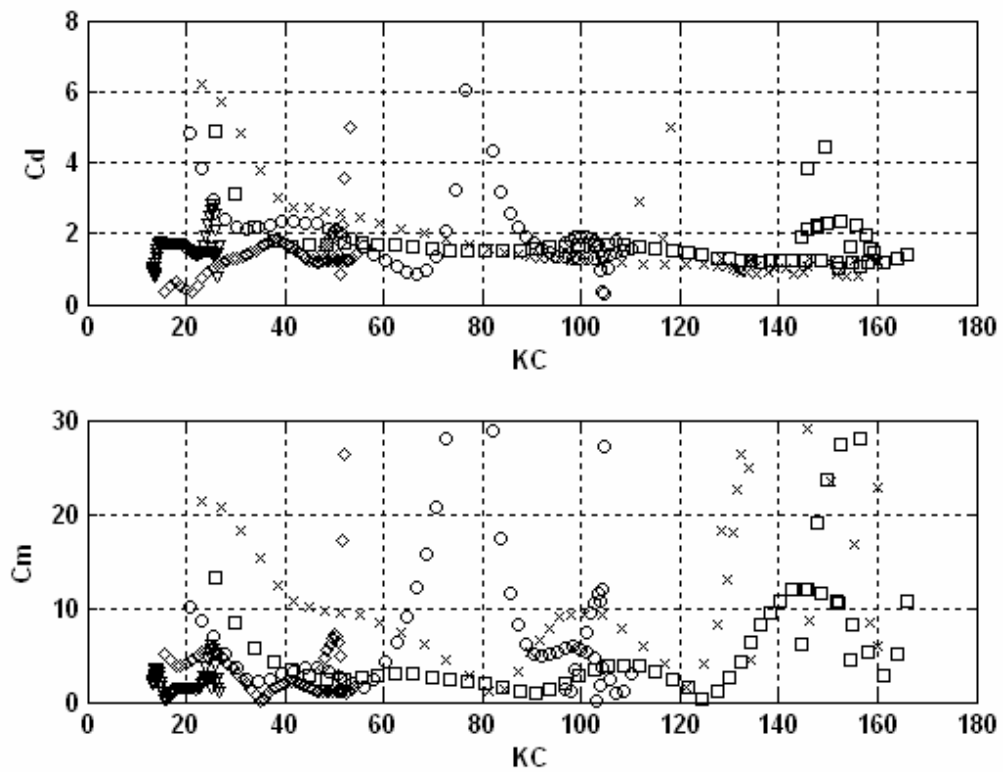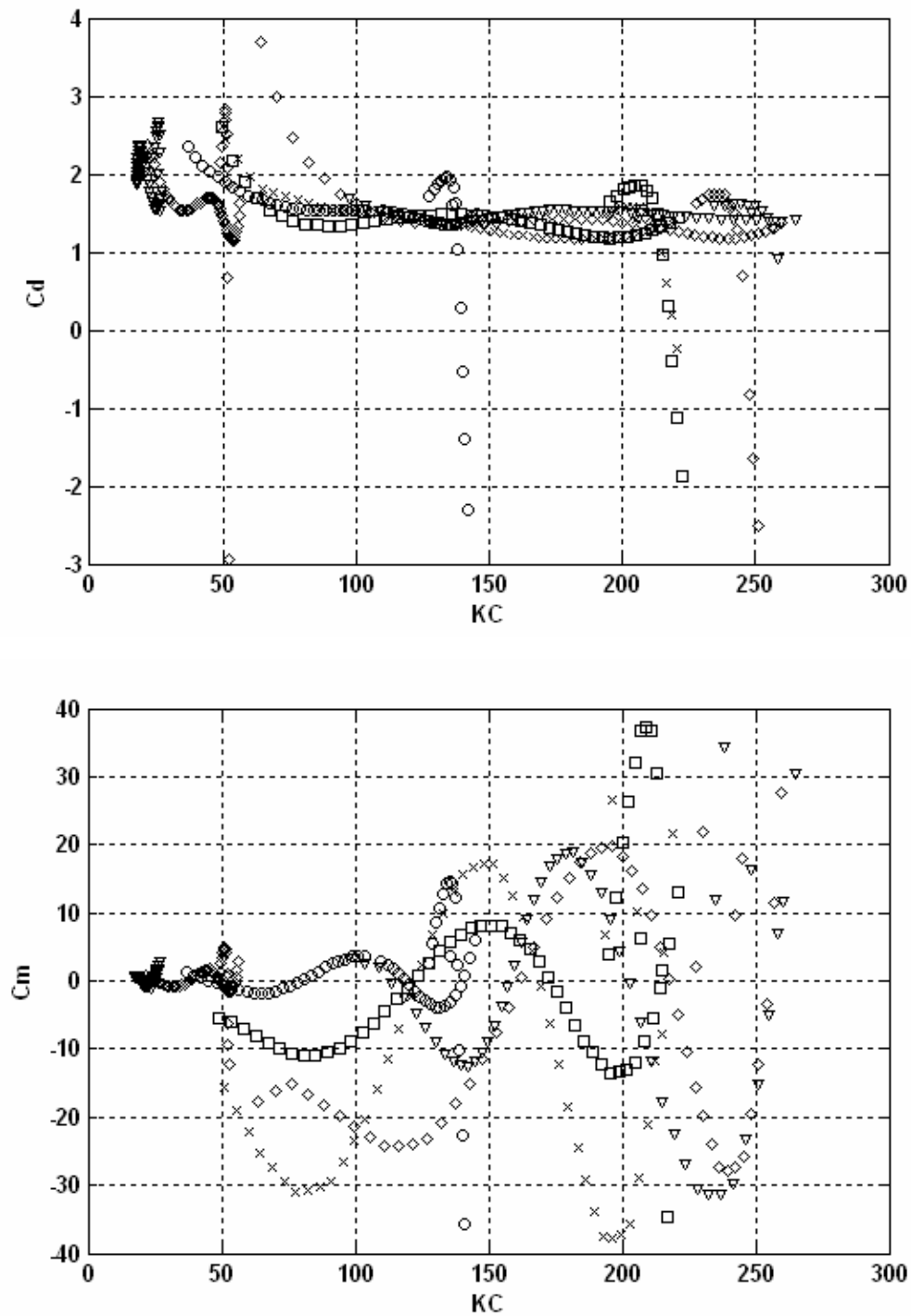**Figure A.10   Fourier-averaged coefficient of chain (diameter: 0.897 cm) with semi-taut catenary configuration**

Figure A.11   Time-averaged coefficient of chain (diameter: 0.897 cm) with

suspended catenary configuration

Figure A.12   Fourier-averaged coefficient of chain (diameter: 0.897 cm) with

suspended catenary configuration
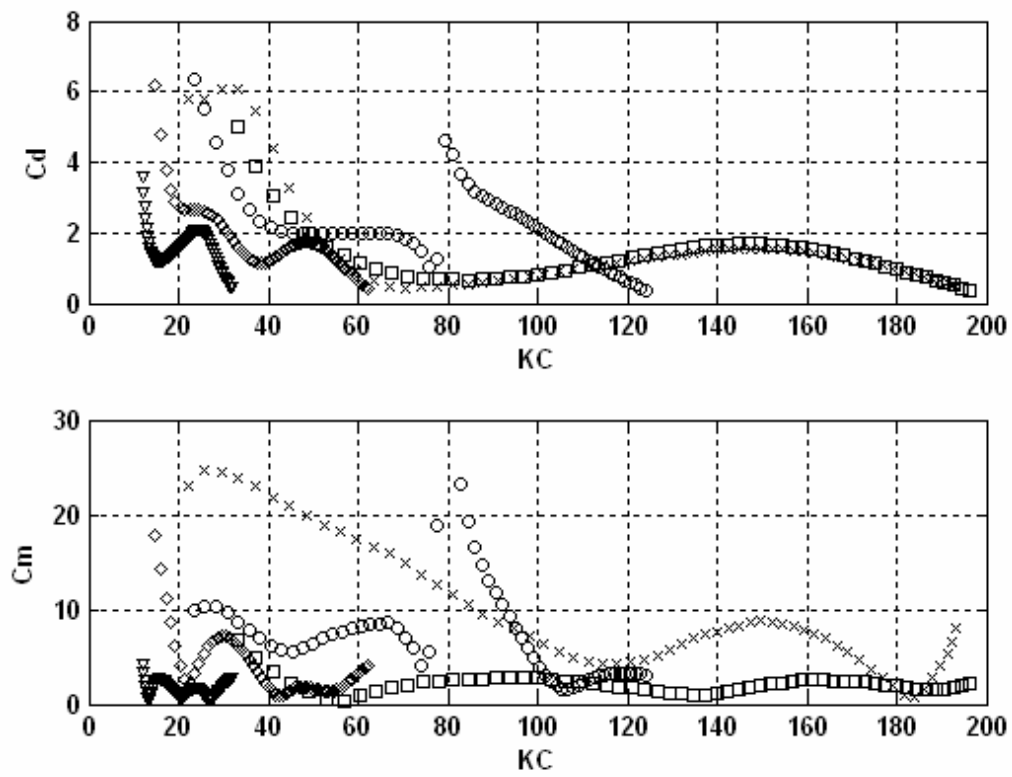
Figure A.13   Time-averaged coefficient of wire (diameter: 0.767 cm) with semi-taut catenary configuration

Figure A.14   Fourier-averaged coefficient of wire (diameter: 0.767 cm) with semi-

taut catenary configuration

Figure A.15   Time-averaged drag and added mass coefficient of chain – wire

(diameter: 0.897 cm - 0.767 cm) with semi-taut catenary configuration

Figure A.16   Fourier-averaged drag and added mass coefficient of chain – wire (diameter: 0.897 cm - 0.767 cm) with semi-taut catenary configuration

A.3. Big Size Mooring

Graph legend [○ : Frequency = 1/5 Hz, □ : Frequency = 1/10 Hz, × : Frequency= 1/15 Hz, ▽ : Frequency = 1/1.5 & 1/15 Hz, ◊ : Frequency = 1/3 & 1/15 Hz]
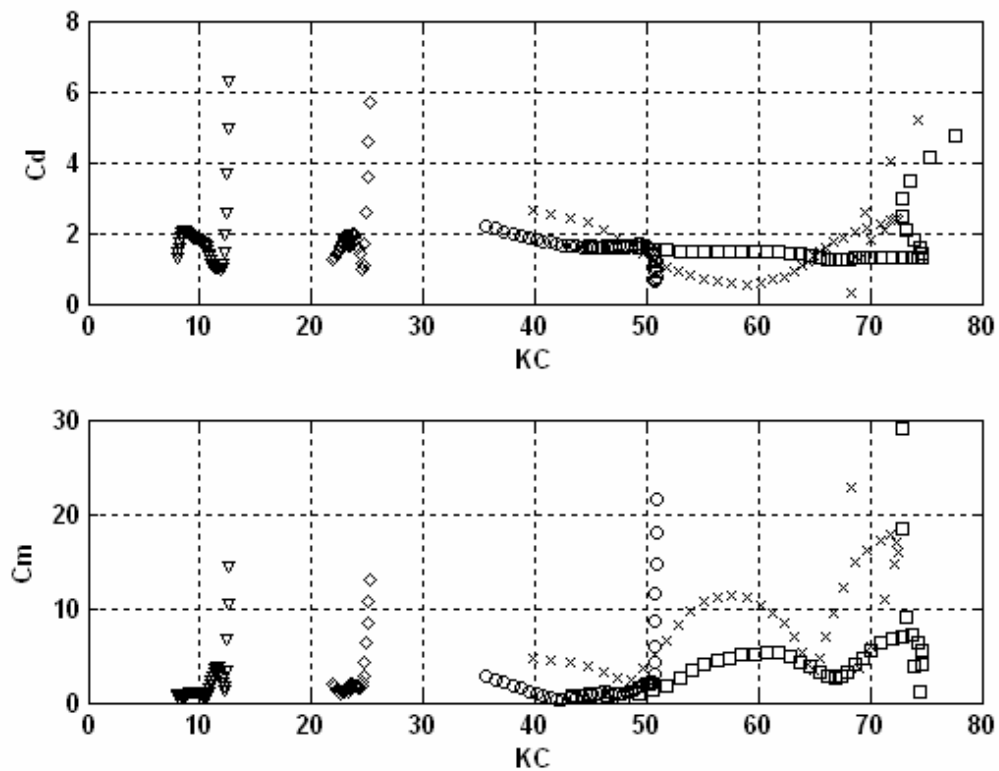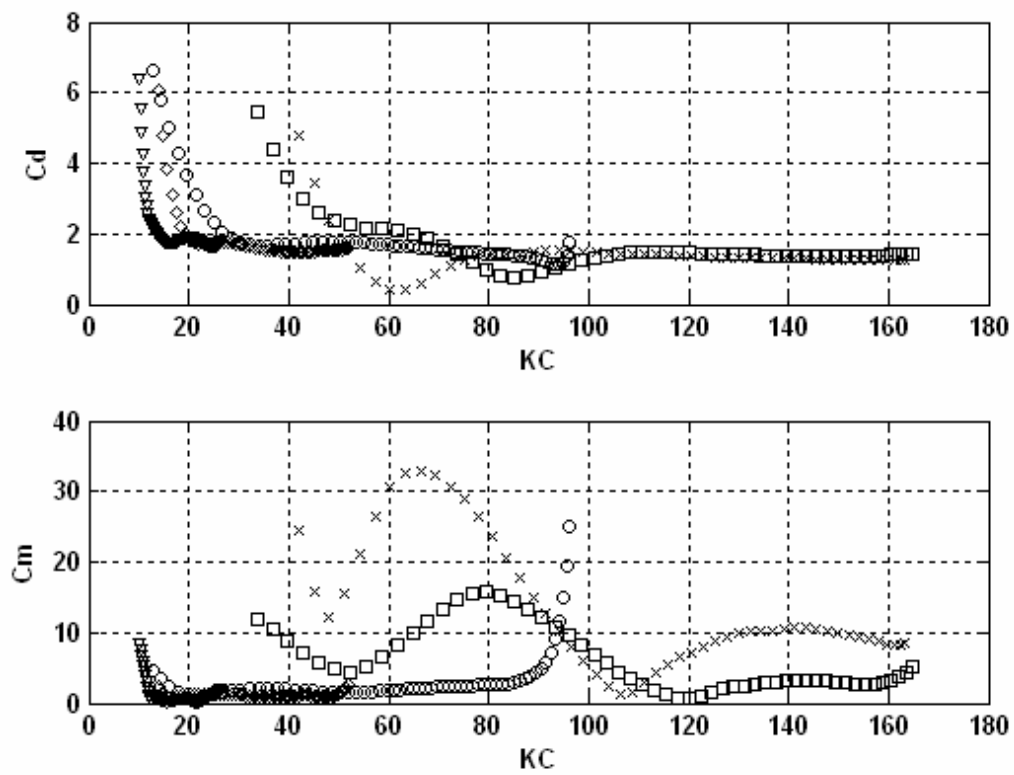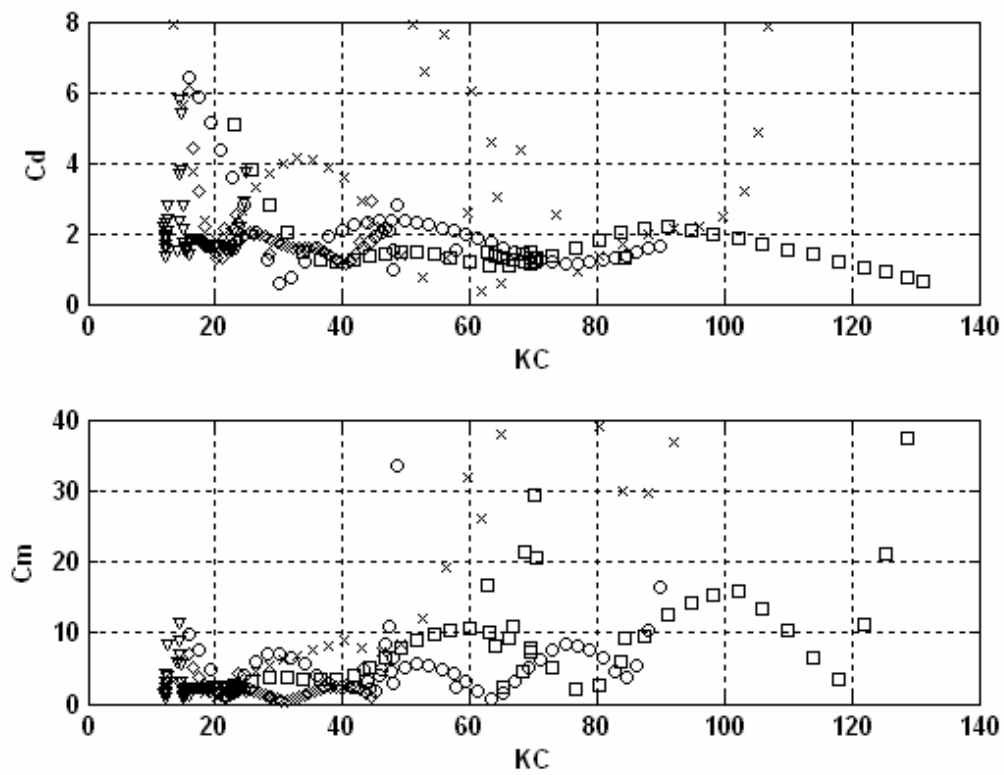

Figure A.17   Time-averaged drag and added mass coefficient of chain (diameter: 1.954 cm) with suspended catenary configuration

Figure A.18   Time-averaged drag and added mass coefficient of wire (diameter:

0.915 cm) with semi-taut catenary configuration

Figure A.19   Time-averaged drag and added mass coefficient of chain – wire

(diameter: 1.954 cm - 0.915 cm) with semi-taut catenary configuration

VITA

Woo Seuk Yang was born in Busan, Korea, 1973. He graduated from Chung-Ang University with a bachelor of science in civil engineering in February, 1999. He entered the graduate school at Chung-Ang University in March, 1999 and received a master of science in civil engineering in February, 2001. After graduation, he entered the graduate program at Texas A&M University in August, 2001 and received a Ph.D. in ocean engineering in December, 2007. He is married to Eun-Hee Cha and has a son, Andrew Yang.

His permanent address is:

Busan-si, Suyeong-gu,

Namcheon-dong, New Beach Apt 501-1001

Busan, Korea 608-010

e-mail address: lubinstein@msn.com